1-15-2020

Fabrication of vascularized scaffolds for the treatment of spinal cord injury

Paul P. Partyka
Rowan University

FABRICATION OF VASCULARIZD SCAFFOLDS FOR THE TREATMENT OF SPINAL CORD INJURY

by

Paul P. Partyka

A Dissertation

Submitted to the
Department of Biomedical Engineering
Henry M. Rowan College of Engineering
In partial fulfillment of the requirement
For the degree of
Doctor of Philosophy
at
Rowan University
June 2018

Dissertation Advisor: Peter A. Galie, Ph.D.

Dedication

To my Loving Family: Wife Bekah; Daughter Katherine; Parents Teresa and Joseph; Siblings Anna and Mark; Aunt Ryszarda.

Acknowledgments

I would like to thank my advisor, mentors, and committee members for believing, supporting, and guiding me throughout my educational career. My advisor Dr. Peter Galie has always pushed me to become the best version of myself and for this I am genuinely thankful and hope to apply this skillset to all my future endeavors. He is my role model for his dedication, perseverance, ability to effectively balance demanding work schedule with a busy family life, and for his attitude to push-forward until the job is done. In addition, if one day I will be half as brilliant as he is, then I will be a successful physician scientist. I would like to thank my long term mentors Dr. Thomas Cavalieri, Dr. John Li, and Dr. Hasan Ayaz for always providing unconditional support. A special thank you to Dr. Thomas Cavalieri for guiding me, beginning from my undergraduate education to my current status as a Ph.D./D.O. student. Your advice, recommendations, and guidance are invaluable and have contributed to where I stand today. Next I would like to sincerely thank my committee members Dr. Byrne, Dr. Lowman, Dr. Merrill, and Dr. Nagele for their commitment, support, and time. Each one of you have contributed to my success and for this I am grateful.

None of my accomplishments would be possible without my fundamental faith in Lord Jesus Christ and without the continuous love and support from my family for which I am eternally thankful. I thank my parents for always believing and supporting my educational endeavors, and equipping me with the skills, morals, faith, and independence needed to be an invaluable asset to the society. My father is my role model whom I hope to mimic one day; if I will be able to be at least half as great as my father is to my family, then I will consider myself accomplished. My mother has always provided tender care and love to her children and to the people that surround her. I am truly blessed to be her son. My older siblings have always looked out and genuinely cared for me. I sincerely appreciate their constant love and protection; this is something that I will never forget.

My beautiful wife Bekah is an angel sent from Heaven who always loves, supports, and believes in me unconditionally, even when my work is incredibly demanding. I truthfully thank you for being there for me. My love for you is eternal, and I am genuinely humbled and incredibly lucky to call you my wife.

Abstract

Paul P. Partyka
FABRICATION OF VASCULARIZED SCAFFOLDS FOR THE TREATMENT OF SPINAL CORD INJURY
2016-2018
Peter A. Galie, Ph.D
Doctor of Philosophy

The overall goal of the research presented here is to evaluate the efficacy of transplanting scaffolds containing central nervous system vasculature to repair spinal cord injury. There are three major phases of this effort: development of a three-dimensional model of central nervous system vasculature, transplantation of a pre-vascularized scaffold, and optimization of the biomaterial used to deliver vasculature to the injured spinal cord. This research has produced the first ever compliant, three-dimensional (3D) blood-brain barrier (BBB) vessel. In order to create vascularized scaffolds appropriate for transplantation into a rat model of spinal cord injury, techniques to fabricate and spatially pattern capillary-scale vasculature that maintain the tight junction morphology characteristic of the BBB are described. Both in vitro experiments using neural precursor cells and in vivo studies using the rat model demonstrate that axons grow along the patterned microvasculature, which demonstrates the potential of harnessing neurovascular interaction as a novel strategy to regenerate the central nervous system. The third phase of the dissertation focuses on improving the biomaterial composition to enhance the infiltration of host axons into the scaffold. Specifically, the permissivity of a RADA-16I nanofiber peptide material is evaluated by measuring axon growth and levels of serotonin receptors within the scaffold. Taken together, this work advances the field of tissue engineering and regenerative medicine by demonstrating the potential of vascularized scaffolds to repair the damaged spinal cord.

Table of Contents

Table of Contents (Continued)

Table of Contents (Continued)

Table of Contents (Continued)

List of Figures

List of Figures (Continued)

Figure Page

List of Tables

Table Page

Chapter I

Introduction

Although major advances have been made in the field of spinal cord regeneration, complete functional recovery following spinal cord injury (SCI) remains elusive. The ultimate goal of SCI treatment is to restore lost motor and sensory function through spinal cord regeneration. To date there is no treatment for SCI beyond medication for pain management (Phillips, Warburton, Ainslie, & Krassioukov, 2014), surgical intervention for spinal decompression (Sekhon & Fehlings, 2001), and physical therapy for rehabilitation (Wernig & Muller, 1992). These management options fail to regenerate the injured spinal cord and thus do not represent a permanent solution to the sustained injury. Cellular and molecular therapies show functional recovery in SCI animal models, but these results have yet to be replicated in clinical trials. Overall, attempts to reinnervate the injured cord demonstrate the complexity of the central nervous system and the need for a novel approach that fully restores function following SCI.

The approach described here involves cellular seeding within protein and peptide-based scaffolds prior to transplantation into a Sprague Dawley rat spinal cord hemisection and contusion injury models. Cells used to perform these studies include hCMEC/D3, hBVP, NHA, and rat derived E14 neural progenitor cells, which are first studied within polydimethylsiloxane microfluidic devices designed to control the biochemical and mechanical environment. Throughout these studies, the cellular response is quantified using methods that include immunofluorescence, immunoblotting, transmission electron microscopy, scanning electron microscopy, rheology, micro-particle image velocimetry, and immunohistochemistry. Additionally, a novel method developed for these analyses

evaluates microvessel barrier integrity using a three-dimensional transendothelial electrical measurement impedance spectroscopy system. The central hypothesis is that delivery of vasculature featuring a blood-spinal cord or blood-brain barrier addresses the secondary aspect of spinal cord injury by restoring oxygen and nutrients to the site of injury without exacerbating the inflammatory response, and the primary aspect by facilitating and guiding the direction of axon growth.

Regarding the terminology between the blood-brain barrier and the blood-spinal cord barrier, there are some specific ultrastructural differences. In rabbit animal studies of the central nervous system vasculature, the blood-spinal cord barrier shows higher permeability values compared to the blood-brain barrier (Prockop, Naidu, Binard, & Ransohoff, 1995). In a different set of experiments, the radiolabeled interferons (INF-α), INF-γ, and tumor necrosis factor (TNF- α) again show higher permeability in the spinal cord than the brain (Pan, Banks, & Kastin, 1997). Additionally, the blood-spinal cord barrier has a decreased expression of the zona occluden-1 and occludin tight junction proteins (Viktor Bartanusz, Daniela Jezova, Betty Alajajian, & Murat Digicaylioglu, 2011). However, the central nervous system makes up the brain and the spinal cord, henceforth both the blood-brain barrier and blood-spinal cord barrier will be referred to as barrier function.

This dissertation is organized into chapters that provide background information on SCI and current treatment strategies, present the in vitro and in vivo results, and place these results in the context of previous work and future clinical applications. Chapter II defines SCI and addresses its epidemiology and current treatment options. The chapter also reviews bioengineered scaffolds for SCI and in vitro vascular models, and introduces

the specific aims of the dissertation. Chapter III details the experimental methodology for both the in vitro and in vivo experimentation. Chapter IV presents the experimental results, and Chapter V discusses the findings related to the research goal of facilitating spinal cord injury. Chapter VI contains detailed experimental protocols along with the statistical analyses performed on the obtained data.

Chapter II

Background

2.1 Spinal Cord Injury

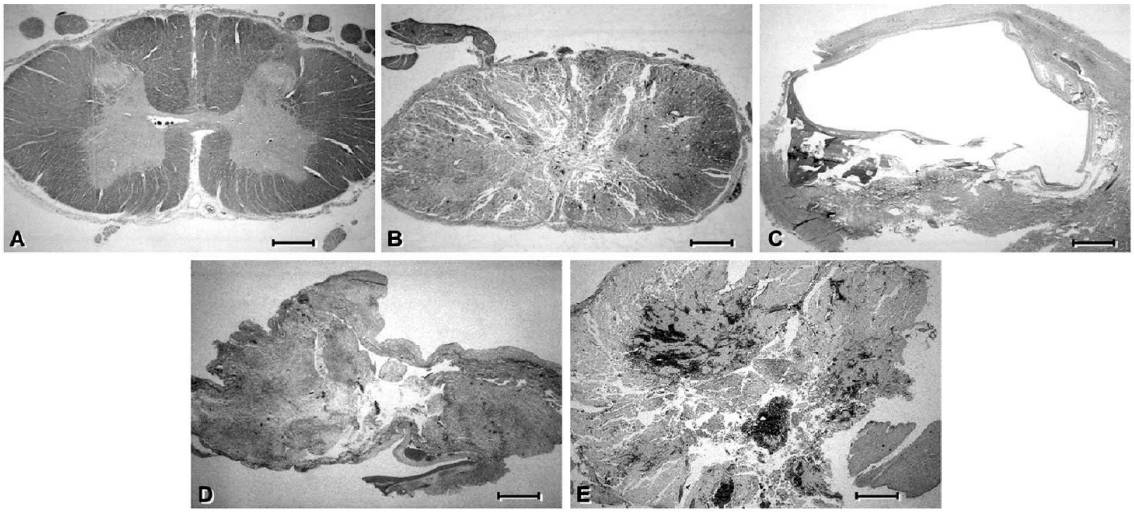

Figure 1. Human spinal cord histological sections of various injury conditions: A) normal, B) solid cord injury, C) contusion injury, D) laceration injury, and E) compression injury. Scale bars are 2 mm. Image taken from Norenberg, 2004.

2.1.1 Introduction to spinal cord injury. Spinal cord injuries (SCI) encompass a wide variety of severities and types of damage to the cells and matrix within the cord. SCI includes contusion, laceration, compression, and solid cord injury (Figure 1), and patients suffering from SCI experience a range of symptoms from burning sensation to complete loss of motor function (Siddall, McClelland, Rutkowski, & Cousins, 2003). The most frequently reported SCI is contusion injury, which is characterized by necrotic and hemorrhaged areas within the cord parenchyma (Norenberg, Smith, & Marcillo, 2004). In laceration SCI, the spinal cord shows visible disruption of the surface anatomy with collagenous connective tissue deposition at the epicenter of the injury. When the

spinal cord suffers a compression injury, the vertebral body fractures the cord, which leads to softening, distortion, and disintegration. The least frequent SCI is solid cord injury which can only be detected with histological examination identifying the prominent disrupted architecture typical of this SCI type (Norenberg et al., 2004). Regardless of the injury type, damage to the spinal cord impairs the motor and sensory signals to and from the brain.

2.1.2 Epidemiology of spinal cord injury. The multitude of people afflicted by SCI motivates the aims of research presented here. Annually, the incidence of new spinal cord injury cases is approximately 54 per one million people in the United States, which translates to 17,500 people per year and a total of approximately 285,000 people (0.09% of the US population) based on the 2017 statistics ("National Spinal Cord Injury Statistical Center, Facts and Figures at a Glance.," 2017). Globally, the incidence of spinal cord injury is 23 cases per million people and the prevalence is between 236 to 4187 cases per million people (Lee, Cripps, Fitzharris, & Wing, 2014). The two main causes for spinal cord injuries are falls and vehicular accidents while injuries due to violence, sports, and medical/surgical events are less common. The financial burden associated with SCI varies based on the severity of injury and the associated neurological impairment, but also on the education and pre-injury employment history (Cao, Chen, & DeVivo, 2011). Not including indirect costs resulting from losses in wages and productivity, the average first year expenses in 2016 after spinal cord injury vary from $352,279 for low severity injury (motor functional at any level-AIS D) to $1,079,412 for high severity injury (high tetraplegia-AIS ABC), respectively. The average yearly expenses for each subsequent year range from $42,789 to $187,443 for low to high

severity injury (Cao et al., 2011). The life expectancy for people with spinal cord injury is between 3.7 to 53 years of life following injury and varies with both the injury severity as well as the age of the person at the time of injury. Regardless of the severity of the injury, people who suffer from spinal cord injury report a significantly lower quality of living compared to people not afflicted by spinal cord injury (Westgren & Levi, 1998). In order to understand the spinal cord injury clinical scale, a short explanation is given in the next paragraph.

Briefly, the American Spinal Injury Association Impairment Scale (AIS) is used to characterize the severity of spinal cord injury with the following ratings (Maynard Jr et al., 1997). Rating "A" is the most severe injury causing complete sensory and motor loss. Individuals with ratings "B" or "C" have loss of motor function or motor function preservation with a muscle grade less than 3, respectively. Rating "D" is for those who have preserved motor function below the neurological level of injury with at least half of the muscles experiencing a grade level of at least a 3. Rating "E" is given to those patients who had prior deficits, but now have normal sensory and motor function.

Due to the complexity of the central nervous system and the inability of axons to spontaneously regrow and facilitate complete functional recovery after SCI, the current treatment options are limited. The standard treatment options of spinal cord injury in the U.S. are medication, surgical intervention, and rehabilitation in the form of physical therapy. Current cellular and molecular therapies in SCI animal models show functional recovery, but the successful translation to the clinic still needs clinical trial approval. The following sections provide a brief review of the pathology of SCI and its lack of neural regeneration, as well as appraise treatment options for patients suffering from SCI.

2.1.3 Introduction to the pathology of spinal cord injury. The human response to SCI includes the initial primary stage that occurs immediately after the insult and the subsequent secondary response that starts days to weeks later. Primary injury involves physical damage to the cord regardless of the type of spinal injury. Physical damage also disrupts blood perfusion, which prevents oxygen and nutrition from being delivered to the injury site. Following primary injury is the secondary injury characterized by tissue hypoxia, ionic imbalance, cytotoxicity, increase in microvasculature permeability, and tissue necrosis. The final result following the primary and secondary responses to SCI is the formation of a glial scar at the injury site, causing a lack of sensory and motor function based on the location and severity of the damage.

The force exerted during primary injury can directly damage the cord structure by tearing or compressing axons. Regardless of the type of SCI sustained, the destructive forces applied to the cord can directly damage the neural tissue structure by tearing or compressing axons. Damage to the axons can result in immediate loss of sensory and motor function at or below the injury level, or in a gradual loss that occurs due to the secondary response mechanisms. The damaging forces from the initial impact to the cord may also disrupt the microvasculature either by rupture, compression, or increased permeability which could limit blood flow and oxygen delivery to the injured cord as well as to the region distal to the injury.

The mechanical damage inflicted to both the cord and microvasculature from this primary injury initiates a cascade of cellular events which together make up the secondary injury. The secondary injury includes increased barrier permeability, inflammation, and cytokine recruitment which can all contribute to the glial scarring that

develops months to years after the insult (V. Bartanusz, D. Jezova, B. Alajajian, & M. Digicaylioglu, 2011). Glial scar development begins with increased BSCB permeability that permits blood leakage into the parenchyma causing reactive gliosis (Preston, Webster, & Small, 2001; Silver & Miller, 2004). Reactive astrocytes can be visualized by staining with the glial fibrillary acidic protein (GFAP) stain which shows the cellular intermediate filament proteins (Eng, 1985). In addition to the reactive astrocytes, inflammatory cells increase the already highly toxic microenvironment for the axons. Inflammatory cells such as T cells and cytokines initially help to eliminate infection by removing dead cells at the injury, but their prolonged activation is detrimental. Inflammation is initiated through macrophage recruitment and upregulation of inhibitory extracellular matrix components such as TNF-α, interferons, TGF-β1 TGF-β2, which all contribute to glial scar formation (Fitch & Silver, 1997). Animal rat SCI experiments verify the presence of these factors and cells at the site of injury (Lagord, Berry, & Logan, 2002). In a separate study of a brain injury model, TGFß1 has been shown to upregulate chondroitin sulfate proteoglycans (Asher et al., 2000), which are produced at the glial scar (McKeon, Hoke, & Silver, 1995). Another cytokine that contributes to glial scarring is interleukin 1, which is an inflammatory protein released by macrophages (Giulian & Lachman, 1985). These cytokines and inflammatory components instigate the eventual formation of a characteristic glial scar.

The mechanical properties of a glial scar are important especially when developing a scaffold for treatment after injury to the spinal cord. The glial scar has considerably softer mechanical properties compared to the healthy uninjured spinal cord (Moeendarbary et al., 2017). Additionally, the glial scar is much softer than scar

formation elsewhere in the body (Stichel & Müller, 1998). Some of the components that contribute to the soft properties of the glial scar include glial intermediate filaments such as GFAP and vimentin, as well as extracellular components such as laminin and collagen IV (Moeendarbary et al., 2017). Substrate stiffness has been shown to play a role in the degree of axon proliferation in the peripheral nervous system such as the dorsal root ganglia, but it does not play a role in central nervous system tissue such as the hippocampus (Koch, Rosoff, Jiang, Geller, & Urbach, 2012). Manipulating substrate stiffness could serve a beneficial role as a means to regenerate the injured cord.

2.1.4 Neural regeneration following spinal cord injury. Due to the effects of primary and secondary injury, the central nervous system lacks the self-regeneration needed for complete neural recovery. Few examples of self-regenerative capabilities in the adult central nervous system have been observed: a rat mediobasal hypothalamus (Chauvet, Prieto, & Alonso, 1998) and an olfactory bulb in a monkey (Monti Graziadei, Karlan, Bernstein, & Graziadei, 1980). In both of these studies the neurons regenerated their axons following complete transection, while axon regeneration in the olfactory bulb was accompanied by active synaptogenesis (Monti Graziadei et al., 1980). This regeneration is not observed in the other segments of the CNS, where axons develop arborizations incapable of regeneration (Li & Raisman, 1995). Lack of neural regeneration has been mainly attributed to the extrinsic environment around the CNS injury such as the reactive astrocytes that form an environment that prevents axons from reinnervation and synaptogenesis.

However, CNS axon terminals can undergo elongation when stimulated with an appropriate microenvironment. The first experiments on rabbits demonstrated that

severed axon terminal endings have sterile nerve fibers incapable of regeneration (Ramon y Cajal, 1928). Since then, scientists have shown that CNS axons have the ability to extend their fibers into transplanted peripheral nerve grafts in the injured CNS (David & Aguayo, 1981). Whether the authors observed damaged axons or spared axons near the injury location remains unclear. To better understand why CNS axons have the potential for regeneration in the absence of gliosis, dystrophic endbulb formation dynamics must be studied further. In the meantime, the next section describes past and current treatment options available to those who suffer from SCI.

2.1.5 Current available treatment options. In the 1980s attempts to manage inflammation associated with SCI immediately after insult included methylprednisolone treatment. Methylprednisolone, a steroid that reduces inflammation, administration in preliminary acute SCI animal models demonstrated significant improvements in both motor function and sensation (Bracken et al., 1990; Bracken et al., 1997). However, one of the main drawbacks of this treatment included the need for rapid injection within eight hours after injury in order to achieve neurological improvement. When translated to clinical trials such as the Rick Hansen Spinal Cord Injury Registry, there was no improvement in motor function even when methylprednisolone was administered within eight hours of injury (Evaniew et al., 2015). Due to lack of functional recovery and the strong adverse side effects such as pneumonia and sepsis, methylprednisolone was stopped as a treatment option for acute SCI (Hugenholtz, 2003).

To this date, acute SCI treatment is nonexistent and is limited to management of associated symptoms such as low blood pressure and muscular dysfunctions. Patients with severe SCI suffer from hypoperfusion of the spinal cord that leads to a systemic low

blood pressure. The current treatment for this condition is the administration of midodrine which brings blood pressure to healthy levels and can even bring moderate cognitive performance improvements (Phillips et al., 2014). In addition to the low blood pressure, SCI patients also experience muscular dysfunction in the form of pain and spasm. These symptoms are managed by medications such as baclofen which act as gamma-aminobutyric acid agonists to inhibit excitatory activity at the spinal reflexes (Sezer, Akkuş, & Uğurlu, 2015). Overall, the use of medications for spinal cord injury is limited to managing the symptoms of the patient rather than instigating regeneration.

Surgical intervention is an additional method to minimize pain after SCI by decompression and stabilization of the spine. Although there are many types of SCIs, compression of the spine is typically caused by a vertebral fracture, ruptured disc, or excess fluids or blood in the spinal cord cavity (Sekhon & Fehlings, 2001). Spinal cord decompression surgeries include laminectomy, laminotomy, foraminotomy, and laminaplasty. Laminectomy is the removal of the bony lamina that forms the posterior walls of each vertebra, while laminotomy is the partial removal of the bony lamina typically only on one side of the vertebrae (Thome et al., 2005). Foraminotomy is bone removal around the surrounding neural foramen which is the location between two vertebrae where the nerve root leaves the spinal canal(Moussa, 2012). Laminaplasty consists of expansion of the spinal canal by cutting the laminae on one side, but this procedure is applicable only to the cervical area of the cord (Lehman, Taylor, Rhee, & Riew, 2008). In addition to surgical decompression of the spine, the spine might also need to be stabilized, which is performed by fusing two or more vertebrae together with bone grafts, rods, or screws. Timing for surgical intervention is critical as the Surgical

Timing in Acute Spinal Cord Injury Study showed that patients who underwent early surgery (14.2 +- 5.4 hours after injury) compared to late surgery (48.3 +- 29.3 hours after injury) had 2.8 times higher odds of at least a 2 grade improvement on the ASIA impairment scale(Fehlings et al., 2012). Surgical intervention after SCI relieves external forces on the spinal cord and ensures that the spinal column is stable so that any pain is minimized. After surgical intervention, patients undergo a period of recovery and many choose to enroll in physical therapy to regain function.

Physical therapy rehabilitation can improve functional recovery in patients with incomplete SCIs. Exercise training in the form of walking improves the paralyzed limb locomotion in patients who have unilateral limb paralysis (Wernig & Muller, 1992). This improvement is the result of the flexion reflex that coordinates neuronal circuits to initiate gait movement in the paralyzed (Wernig & Muller, 1992). Since voluntary muscle activity in the paralyzed limb didn't show significant improvement after the physical therapy, the functional improvement could be due to strengthening the remaining muscle and motor automation of the healthy (Wernig, Nanassy, & Muller, 1998). Unfortunately, patients with complete SCIs are unable to benefit from treadmill walking therapy even in the presence of body weight support (Dietz, Colombo, & Jensen, 1994; Harkema, 2008). Since treadmill exercise training is unable to elicit the flexion reflex, an alternative solution to achieve functional recovery in patients suffering from complete SCIs is needed. The following section will describe the current research themes that focus on regenerating the injured cord as well as some of the clinical trials currently underway to treat SCI.

2.1.6 Cell-based therapies. Cell-based therapies exhibit potential for promoting repair and functional improvements after SCI in animal models. Numerous cell types have been transplanted to SCI animal models including Schwann cells, neural stem/progenitor cells, oligodendrocyte progenitor cells, and mesenchymal stem cells (Mothe & Tator, 2013; Sahni & Kessler, 2010). Schwann cells are a type of glial cell that not only support axon myelination in the peripheral nervous system, but also show improved axonal regeneration after transplantation in the spinal cord (Takami et al., 2002; Xu, Guenard, Kleitman, Aebischer, & Bunge, 1995). Neural stem/progenitor cells transplanted into a compressed rat spinal show function recovery through a neuroprotective mechanism that supports both oligodendrocyte and axon viability (Parr et al., 2008). After SCI numerous myelin-forming oligodendrocytes lose their viability, but transplantation of oligodendrocyte progenitor cells shows potential for axonal remyelination and improvement in motor function (Keirstead et al., 2005). Transplantation of mesenchymal stem cells derived from bone marrow shows the immunomodulatory effects of shifting macrophage phenotype from M1 to M2 phase, which improves axonal viability and leads functional locomotion recovery (Nakajima et al., 2012). All of these transplanted cell types lead to functional improvements, but through different mechanisms including axonal regeneration, neuroprotection, and immunomodulation. Although these cell therapies have shown promise in animal models, the same results have not been observed when translated to humans.

Cell-based therapies for SCI have yet to result in functional recovery in human clinical trials. For example, olfactory ensheathing cells (OEC) and skin-activated macrophages are effective in animal models, yet transplantation of OECs scaffolds to a

complete SCI model resulted in the ability of the rat to regain coordinated walking as evaluated with the climbing test (Ramon-Cueto, Cordero, Santos-Benito, & Avila, 2000). In a similar fashion, transplants of skin-activated macrophages resulted in motor function improvement and cyst reduction (Bomstein et al., 2003). Unfortunately, the same beneficial response of these cellular transplantations is not observed in humans. Transplantation of autologous ensheathing cells in a phase I clinical trial resulted in no significant functional changes in a three year follow up (Feron et al., 2005; Mackay-Sim et al., 2008). Similarly, a phase II clinical trial that used autologous macrophages injections failed to show an improvement between the treated and control groups (Lammertse et al., 2012). For this study, participants had complete neurological injuries between C4 and T11 vertebra segments as classified according to the International Standards for Neurological Classification of Spinal Cord Injury. Due to lack of neurological improvements, these two clinical trials were regressed to conclude that the autologous cells were safe to transplant into humans without evoking any serious side effects. These results underscore the need for improved approaches to cell-based therapies.

2.1.7 Bioengineered scaffolds for spinal cord repair. One method to bridge the injured spinal cord is using engineered scaffolds that provide a permissive environment for axons or progenitor cells that could potentially form relays. Scaffolds transplanted with aligned poly-l-lactic acid microfibers (Hurtado et al., 2011), channels within polylacticcoglycolic acid (Moore et al., 2006), or channels within agarose scaffolds all direct the growth direction of regenerating axons from the host tissue (Stokols & Tuszynski, 2006). However, these studies present obstacles that limit functional recovery

by the low number of axon infiltration, lack of axon outgrowth, and lack of synaptic relay with the host tissue. These results demonstrate the need for permissive matrices that are capable of the higher axon infiltrations with significant outgrowth required to bridge the injured spinal cord and restore functionality.

Transplantation of scaffolds containing Schwann cells to the injured spinal cord results in host axon infiltration and myelination within the grafts, but axon outgrowth remains insignificant (Guest, Rao, Olson, Bunge, & Bunge, 1997). Schwann cells have the potential to elicit central nerve regeneration due to their peripheral regenerating capabilities, peripheral axon myelination, and extracellular matrix deposition (Bunge, 1993). Transplantation of human Schwann cells supplemented with methylprednisolone resulted in host neuronal infiltration within the polyacrylonitrile/polyvinylchloride-based graft (Guest et al., 1997). Specifically, neuronal populations of the following types were present within the graft: propriospinal, sensory, motorneuronal, and brainstem neurons. Despite the success with axon infiltration into these scaffolds, a central limitation to Schwann cell treatment for spinal cord injury is that only a mere 1% of the axons that enter the grafts reenter the host spinal cord tissue(Guest et al., 1997). Lack of axon outgrowth from the scaffold eliminates the potential for successful functional restoration.

Olfactory ensheathing cells (OEC) overcome this limitation due to their intrinsic ability for continuous neurogenesis into adulthood (Fairless & Barnett, 2005). OEC transplantations improve host axon infiltration into the scaffolds and axon outgrowth into the host spinal cord tissue, which is a major improvement compared to transplants with other cell types. Specifically, one study showed propriospinal axon infiltration into and out of the OEC-seeded polyacrylonitrile/polyvinylchloride transplant (Ramon-Cueto,

Plant, Avila, & Bunge, 1998). In order to demonstrate functional recovery, axon continuity across the injury site is needed for synapse transmission. The functional recovery of rat forepaw reaching ability was assessed after OEC injection into the corticospinal tract. The rat showed functional improvement in as little as six days after transplantations (Li, Field, & Raisman, 1997). Although functional recovery was possible after OEC transplantations in these 1990s controlled animal experiments, recent data shows lack of functional improvements between studies due to the absence of a purification procedure in OEC transplantation therapies (Yao et al., 2018). The current OEC identification marker is p75NTR that is nonspecific and stains positive for other cell types such as astrocytes, Schwann cells, and lamina propria mesenchymal stem cells (Yao et al., 2018). Even though studies with OEC cell grafts transplants reported functional improvements, this therapy shows inconsistent results between studies due to the lack of a unique OEC marker (Yao et al., 2018).

Multifactorial SCI treatment approaches include combining cell-seeded scaffold therapies with neurotrophic factors or complementary cell types. A common example is to supplement transplanted Schwann cells (SC) or bone marrow stromal cells (MSC) with either olfactory ensheathing cells (OEC) or neurotrophic growth factor (NT-3). One of the caveats of transplantation of SC cells only is the limited outgrowth from the grafts, but this has been shown to improve by the addition of OECs at the polyacrylonitrile/ polyvinylchloride-based scaffold exit (Fouad et al., 2005). In addition, upregulating factors that control axon growth cone orientation (Song, Ming, & Poo, 1997) and distance (Cai et al., 2001), such as cyclic adenosine monophosphate (cAMP), resulted in axon sparing, myelination, and serotonergic axon infiltration into and out of transplanted

scaffolds (Pearse et al., 2004). In addition to SC, bone marrow stromal cells (MSC) have been tested to regenerate the spinal cord. Specifically, autologous MSCs were supplemented with cAMP and an axon growth factor NT-3 and transplanted into a rat SCI that resulted in sensory axon infiltration and outgrowth from the scaffolds (Lu, Yang, Jones, Filbin, & Tuszynski, 2004). Combining cAMP and growth factors together have contributed to axonal regeneration beyond the injured cord that has not been observed with treatment of either variable alone. In addition, the usage of progenitor cells is an attractive option with promising results due to the vast differential potential of these cells. Additionally, transplantations using progenitor cells holds great promise in reinnervating the injured cord due to the differentiating potential of these cells.

Transplantation of progenitor cell-seeded grafts into the injured CNS show that these cells form synapses with host neurons and provide significant functional improvements. Neural and glial restrictor progenitor cells differentiate into neuronal and oligodendrocyte cells, which are two of the cell types that are damaged during SCI. Transplantation of host derived neural progenitor cells from a rat animal model results in functional synapse restoration between host axons and graft-derived axons (Bonner et al., 2011; Kadoya et al., 2016). The same result is seen using human neural stem cell grafts transplanted into both rat and mouse animal models (Cummings et al., 2005; Lu et al., 2012). As a way to mimic the larger human spinal cord, a large nonhuman primate animal study on rhesus monkeys was performed to evaluate the potential of human neural progenitor cells to restore functional relay. Similar to the smaller model rodent studies, host axons exhibited infiltration and outgrowth from the scaffolds with functional synapses in the distal gray matter that led to improved forelimb function (Rosenzweig et

al., 2018). Despite these results, the main shortcoming of this primate study included incomplete spinal cord transection at the level of C7 which is known to exhibit endogenous extensive functional recovery (Friedli et al., 2015). Though studies have employed scaffolds seeded with endothelial progenitor cells to develop a vascular network following transplantation (Saglam et al., 2013), there have been no attempts to pre-vascularize scaffolds prior to transplantation. Table 1 below shows a summary of previous studies that attempt to repair the injured spinal cord.

Table 1

Summary of previous scaffolds for spinal cord repair

Study	**Cells Used**	**Scaffold Type**	**Summary of results**	**Limitations**
Guest, 1997	Schwann cells	polyacrylonitrile/ polyvinylchloride	Axon infiltration and myelination	Low axon outgrowth
Raisman, 1997; Yao 2018; Fouad 2005	Olfactory ensheathing cells	polyacrylonitrile/ polyvinylchloride	Increased axon outgrowth	High variability in result replication due to lack of a standardized OEC purification technique
Lu 2004	Bone marrow stromal cells + cAMP + NT3	Injection method	Sensory axon infiltration and outgrowth	Low axon outgrowth
Bonner 2011; Kadoya 2016	Rat neural progenitor cells/ Human derived neural stem cells	Injection method	Functional synapse restoration	Lack of axon guidance across scaffold
Cummings 2005; Lu 2012; Rosenzweig; 2018	Human neural stem cells	Injection method	Functional synapse restoration	Incomplete spinal cord transection

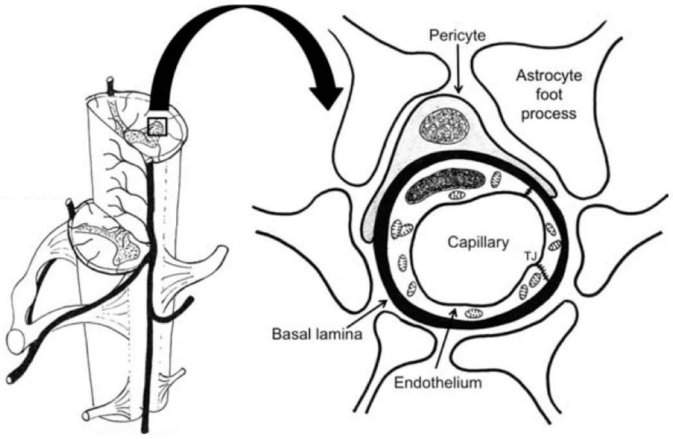

Figure 2. Cross section of a blood-spinal cord barrier demonstrating astrocyte foot processes, pericytes, basal lamina, and tight junctions in the endothelium. Image taken from Bartanusz, 2011.

2.1.8 Central nervous system vascularization. The vasculature in the spinal cord has a different structure and function than vasculature found elsewhere in the human body. The spinal cord and the brain make up the central nervous system, where the endothelial cells lining the vascular bed exhibit tight junctions that give rise to the blood-spinal cord barrier (Figure 2) and the blood-brain barrier, respectively. This highly selective barrier that prevents the leakage of blood constituents into the parenchyma. Compared to endothelial cells in other parts of the body, these central nervous system endothelial cells have junctional complex proteins such as zona occluden-1 and claudin-5 that limit paracellular transport (Hirase et al., 1997; Kanda, Numata, & Mizusawa, 2004; Wen, Watry, Marcondes, & Fox, 2004). This reduced permeability is needed to prevent damage to the brain and spinal cord by reducing the influx of plasma components into the surrounding tissue. In addition to paracellular transport, transcellular movement through

the blood-brain barrier transports lipid-soluble gases such as oxygen and carbon dioxide, substances such as glucose and amino acids, as well as ions such as sodium and potassium (Daneman & Prat, 2015). One of the main pathological characteristic of spinal cord injury is the disruption of the blood-spinal cord barrier where leakage of blood into the parenchyma contributes to a hostile environment preventing regeneration.

In addition, damage to the cord can result in vascular ischemic conditions that cause CNS vasculature breakdown by disruption of endothelial tight junctions, causing increased permeability. This ischemic episode can occur at the injured location of the cord or distal to the site of injury. Regardless of the location, the interrupted blood flow leads to decreased oxygen and nutrient delivery that causes the endothelial tight junctions to increase their permeability (del Zoppo & Hallenbeck, 2000). An in vitro study suggests that the mechanism for increased vascular permeability during hypoxic conditions could be due to autocrine vascular endothelial growth factor upregulation and nitric oxide synthesis (Fischer et al., 1999). In addition, the presence of astrocytes or pericytes has been shown to reduce endothelial sensitivity to hypoxic conditions, which translates to the ability to maintain low barrier permeability despite being exposed to hypoxic conditions (Fischer, Wobben, Kleinstuck, Renz, & Schaper, 2000; Hayashi et al., 2004). However, SCI injury usually causes both hypoxia and glial death that contributes to increased vascular permeability and widespread damage (Witt, Mark, Hom, & Davis, 2003).

In addition to the vascular permeability, there is also substantial vascular remodeling at the injured cord. One week after injury to the cord, angiogenesis is at its maximum activity especially at the epicenter of the injury, with decreasing vascular

sprouting farther from the injury (Cyril Dray, Geneviève Rougon, & Franck Debarbieux, 2009). The increased vascular response provides the required nutrients for endogenous treatment and secondary response. Interestingly, two weeks after injury there is substantial vascular pruning that results in very few stable vessels that supply the injured cord. This reduced vascular activity is maintained even at seventy-seven days after injury in a mouse animal model (Cyril Dray et al., 2009). These results show that the majority of the vascular remodeling at the injured spinal cord is complete by two weeks.

Due to the complexity of the vascular remodeling in vivo, studying the vascular response has been isolated and simplified using in vitro vascularized models (Audus & Borchardt, 1986; Dehouck, Meresse, Delorme, Fruchart, & Cecchelli, 1990; Pardridge, Triguero, Yang, & Cancilla, 1990; Rubin et al., 1991). The use of human cells, the potential for high-throughput testing, and the level of control over mechanical and biochemical stimuli yield a substantial advantage compared to in vivo experiments in animals. The main drawback of these models, as with any in vitro platform, is their inability to recapitulate the complete in vivo microenvironment. This caveat is exacerbated in CNS models by the complexity of the neurovascular unit, a three-dimensional arrangement of endothelium surrounded by basal lamina, pericytes, and astrocytic endfeet processes (Abbott, Ronnback, & Hansson, 2006; Hawkins & Davis, 2005; Persidsky, Ramirez, Haorah, & Kanmogne, 2006; Winkler, Bell, & Zlokovic, 2011).

The shear stress exerted by blood flow is one mechanical stimulus in particular that has been thoroughly investigated in previous in vitro models of the CNS (Booth & Kim, 2012; Cucullo, Hossain, Puvenna, Marchi, & Janigro, 2011; Deosarkar et al., 2015;

Griep et al., 2013; Prabhakarpandian et al., 2013; van der Helm, van der Meer, Eijkel, van den Berg, & Segerink, 2016). Previous models have found that application of shear stress bolsters the CNS function of endothelial monolayers. However, shear stress is not the only mechanical stimulus caused by blood flow: the vascular wall also experiences cyclic strain due to pressure-induced dilation. Studying the effects of wall strain requires a 3D model of the CNS due to the cylindrical geometry of neurovasculature. But current 3D models are incapable of interrogating the effects of stretch due to lack of perfusion (Cho et al., 2015; Herland et al., 2016; van der Meer, Orlova, ten Dijke, van den Berg, & Mummery, 2013) or dependence on synthetic membranes to support the endothelium (Cucullo, Marchi, Hossain, & Janigro, 2011; Cucullo et al., 2002).

Current 3D CNS models lack physiologically relevant diameter sizes or fail to demonstrate barrier integrity of the vasculature. 3D in vitro CNS models have vasculature diameter ranges up to 800 μm (Cho et al., 2015; Herland et al., 2016), which is not comparable to the human CNS vasculature diameters that range from 7 μm- diameter capillaries to 90 μm- diameter arterioles and venules (Bell & Zlokovic, 2009). Although smaller 5 μm- diameter in vitro microvessel models exist (Chrobak, Potter, & Tien, 2006; Riemenschneider et al., 2016), these platforms fail to demonstrate barrier-integrity and thus cannot mimic CNS vasculature. Creating a vascularized model that exhibits similar diameter and integrity as the CNS-vasculature in vivo is important when used as a scaffold for the injured spinal cord.

The primary benefit of a pre-vascularized scaffold is the ability to pattern the vessels prior to transplantation. Previous studies have demonstrated that multiple mechanical and biochemical cues can be used to align vasculature in vitro. Specifically,

both interstitial fluid flow and mechanical strain have been used to direct the orientation of microvessels (Butcher, Penrod, Garcia, & Nerem, 2004; Krishnan et al., 2008; Morin, Dries-Devlin, & Tranquillo, 2014; Polacheck, Charest, & Kamm, 2011; Riemenschneider et al., 2016). Due to the interdependence between vascular and neural systems, aligned vasculature may act as a guidance cue for infiltrating axons. Although this strategy has not been applied to the CNS, human umbilical vein endothelial cells (HUVECs) have been shown to secrete BDNF to stimulate and guide axon growth from a dorsal root ganglia body (Grasman & Kaplan, 2017).

In addition to pre-vascularizing a scaffold for CNS regeneration, the material of the scaffold needs to be appropriate for axon infiltration and vascular growth. Potential biomaterials include nanofiber peptides, which self-assemble in response to pH changes (Ye et al., 2008). One such peptide is the RADA-16I hydrogel which has been shown to demonstrate high axon infiltration (Ellis-Behnke et al., 2006; J. Guo et al., 2007) and cellular viability (Genove, Shen, Zhang, & Semino, 2005) within this synthetic material. Additionally, previous studies have shown that this nanofiber peptide supports neurite outgrowth (Holmes et al., 2000) and capillary morphogenesis (Sieminski, Was, Kim, Gong, & Kamm, 2007) within this nanofiber peptide. Another benefit of using RADA-16I is that this material is biocompatible and produces minimal inflammation with the host tissue (Ellis-Behnke et al., 2006; J. Guo et al., 2007).

2.2 Hypothesis and Specific Aims

The purpose of this research is to investigate whether incorporating BSCB-integrity vasculature into transplantable scaffolds holds promise for SCI treatment. The central hypothesis of the study is that delivery of vasculature featuring a barrier function

addresses the secondary aspect of spinal cord injury by restoring oxygen and nutrients to the site of injury without exacerbating the inflammatory response and the primary aspect by facilitating and guiding the direction of axon growth. It has been clearly established that the vascular and neural networks are intimately linked in the CNS; but capitalizing on this interaction to facilitate a regenerative approach is novel.

Specific Aim 1: Create a pre-patterned vessel within a microfluidic device with barrier-integrity vasculature. The goal of the first aim is to assess the barrier function of microvessels fabricated within collagen/HA scaffolds using immunohistochemistry. A central requirement of a vascularized scaffold for SCI repair is that the vasculature exhibits characteristics that are unique to the central nervous system. The presence of tight junctions that prevent passage of plasma components from blood into the surrounding tissue is crucial for blood vessels in the spinal cord. The expected results for this aim include the presence of punctate tight junction staining localized to the endothelial cell membrane.

Specific Aim 2: Exploit intrinsic neurovascular properties between axons and microvessels to guide axon growth. The goal of the second aim is to evaluate the ability of an aligned pre-vascularized scaffold to guide axon growth across the site of an acute hemisection cervical SCI. Due to the interdependence between vascular and neural systems, aligned vasculature may act as a guidance cue for infiltrating axons. The expected result is that the aligned microvessels will guide the axons in the rostral-caudal direction of the spinal cord.

Specific Aim 3: Increase host axon permissivity within transplants using a nanofiber self-assembling RADA-16I peptide matrix. The goal of the last aim is to assess the

permissivity of the peptide scaffold using immunohistochemistry after scaffold transplantations into a cervical SCI. Peptide-based scaffolds, specifically the RADA 16-I-based matrix, provide a more permissive matrix for axon infiltration. The expected results include an increase in the number of axons infiltrating into the scaffold.

The overall goal of this research is to evaluate the efficacy of using BSCB-integrity microvasculature patterned in a permissive scaffold to stimulate and direct the growth of axons across the site of an SCI so that functional improvements can be achieved.

Chapter III

Methods and Materials

3.1 Experimental Methods

3.1.1 Pre-patterned microvasculature.

3.1.1.1 Microfluidic device fabrication. Fabrication of the microfluidic device was completed by soft lithography using a previously described method (Galie et al., 2014). Briefly, a 3-inch silicon wafer was placed on a hot plate for 5 minutes at 60ºC. Using a 10-mL plastic syringe (BD Bioscience), 7 mL of SU-8 2025 photoresist (MicroChem) was poured on top of the 3-inch silicon wafer. Air bubbles were moved to the center of the wafer using the tip of the 10 mL plastic syringe. An aluminum cover was placed over the wafer to protect it from light. The temperature of the hot plate was increased to 95ºC for overnight incubation. The next day, the hot plate temperature was lowered to 60ºC and air bubbles were removed by puncturing with a 180 μm diameter acupuncture needle. The temperature of the hotplate was increased back to 95ºC and left for 10 minutes until the surface appeared homogenous. The hot plate was then turned off and the wafer was left to cool for 15 minutes. A photomask was placed over the wafer before exposure with a 200W UV lamp for 2 hours. Propylene glycol methyl ether acetate (PGMEA) (MicroChem) was used to dissolve the unpolymerized photoresist, and poly-dimethylsiloxane (PDMS) (Corning) was used to create negative molds from the silicon master. Following silanization, positive PDMS stamps were cast to create the microfluidic channels on 22 mm by 22 mm cover slips. Prior to gel fabrication, the hydrogel reservoir was filled with 10 N sulfuric acid for 90 min, washed thoroughly with distilled water, and then filled with 20 μg/mL of collagen type I (MP Biomedical)

dissolved in phosphate buffered saline (PBS). This method was shown to promote hydrogel attachment to PDMS as described in a previous study (Galie & Stegemann, 2011).

3.1.1.2 Collagen/hyaluronan hydrogel formation. At the time of gel fabrication, passage 5-7 normal human astrocytes NHA (Lonza) cultured in astrocyte growth medium (Lonza) were trypsinized and centrifuged to a final concentration of 1 million cells per mL of hydrogel. Each device was filled with 50 µL hydrogel consisting of the following: 5 µL 10x PBS, 5 µL NaOH, 2.5 µL distilled water, 5 µL Matrigel (Corning), 2.5 µL Extralink (from HyStem kit, Glycosan), 5 µL thiol-modified hyaluronan (from Hystem kit, Glycosan), and 25 µL 10 mg/mL collagen type I (MP Biomedical). This formulation yielded a gel consisting of 5 µg/mL collagen, 1 µg/mL Matrigel, and 1 µg/mL HA, mimicking a previous study investigating the effect of hydrogel formulation on astrocyte spreading (Placone et al., 2015). After mixing, the hydrogel was added to the astrocyte cell pellet and then injected into the hydrogel reservoir of the device. Two 180-µm-diameter acupuncture needles (DBC) were inserted into the needle guides of the device, and the assembly was placed at 37ºC for ten minutes to facilitate polymerization. Astrocyte growth medium was then pipetted on the ports of the hydrogel reservoir to prevent drying of the hydrogel and provide nutrients for the seeded astrocytes. After 1-2 h of incubation, the needles were pulled from the hydrogel to create cylindrical voids (Chrobak et al., 2006). Human cerebral microvascular endothelial cells hCMEC/D3 (Weksler et al., 2005), cultured on gelatin-coated plates using Endothelial Cell Basal Medium (EBM-2, PromoCell) supplemented with 5 µg/mL ascorbic acid (Sigma), 1 ng/mL human basic fibroblast growth factor (Sigma), 1/100 chemically defined lipid

concentrate (Thermo Fisher), 5% fetal bovine serum (VWR Life Science), 10 mM HEPES (Quality Biological), 1.4 μM hydrocortisone (Sigma), and 1% penicillin-streptomycin (Corning); we hereafter refer to this medium as modified endothelial growth medium (mEGM). The cells were injected into one of the channels at a density of 3-5 million cells per mL. The channel was then incubated for ten minutes prior to a second injection of hCMEC/D3 cells, and an additional ten-minute incubation in an inverted position to facilitate full coverage of the cylindrical void.

3.1.1.3 Mechanical stimulation.

3.1.1.3.1 Lumen shear stress and pressure-driven radial strain. Cell-seeded channels were cultured in 10 mL of mEGM and placed in the incubator for four days of either static or perfused conditions. For static controls, the channels remained within the same volume of culture medium during the four-day time period. For channels exposed to shear stress, the input port for the cell-seeded channel was attached to a 10 mL plastic syringe (BD) secured to a GenieTouch linear syringe pump (Kent Scientific). The syringe pump delivered a 2.4 μL/min volumetric flow rate, which exerted approximately 0.7 dynes/cm^2 of shear stress on the endothelium within the channel assuming fully developed Poiseuille flow governed by Equation 1:

$$\frac{v(r)}{v_{max}} = 1 - \left(\frac{r}{R}\right)^2 \tag{2}$$

where r is the radial coordinate and v_{max} is the velocity at the centerline, and R is the 180-μm diameter of the channel. For channels exposed to cyclic stretch, the channels were first incubated in static conditions for three days. On the third day, both the input and output ports of one channel were attached to 10 mL syringes filled with mEGM, and silicone grease (Bayer) was applied to the opening of the needle guide to prevent leakage.

The syringes were fixed together and secured to the platform of a rocking platform (VWR- 82007-202). A video of the rocker motion was captured and analyzed in ImageJ to determine the height as a function of time to determine the hydrostatic pressure exerted on the lumen of the channel. Cyclic pressure was applied to the lumen for approximately 18 hours prior to permeability testing.

3.1.1.4 Barrier integrity verification.

3.1.1.4.1 Dextran transport assay. Channels were removed from their respective testing conditions (static, shear, or stretch) and placed on the stage of an inverted epifluorescence microscope (Zeiss Axiostar 10). The devices were perfused with 4-kDa FITC-dextran (Sigma-Aldrich) at a flow rate of 5 μL/min. Images were taken at 10-s intervals and then imported into ImageJ for analysis. Quantification of permeability coefficient was determined using a method described in a previous study (Adamson, Lenz, & Curry, 1994). The coefficient, P, was determined by correlating dextran concentration to fluorescent intensity and using the measurements with the following equation 2:

$$P = \frac{dI}{dt}\frac{r}{2I_o} \tag{2}$$

where $\frac{dI}{dt}$ is the change in fluorescent intensity in a region of interest outside the lumen, r is the channel radius (approximately 90 μm), and I_0 is the maximum intensity in lumen during the duration of the test (approximately 5 minutes).

3.1.1.4.2 Immunocytochemistry

Devices were fixed in 3.7% paraformaldehyde for 20 minutes at room temperature. After fixation, the hydrogels were removed from the device reservoir and placed in a 100-μL centrifuge tube. Permeabilization was completed by addition of 0.2%

Triton X-100 for 30 minutes at room temperature. After permeabilization the hydrogels were blocked in either 5% donkey serum or 3% bovine serum albumin (BSA) for 30 minutes at 37ºC. Hydrogels were then incubated overnight at 4ºC with one or more of the following: 1:100 anti-laminin sc-59980 (Santa Cruz), 1:100 anti-GFAP sc-33673 (Santa Cruz), or 1:250 anti-ZO-1 D7D12 (Cell Signaling). After washing with PBS, the hydrogels were incubated with 1:500-1:1000 of the secondary antibody, 1 mg/mL of DAPI, and 1:30 of Texas Red-conjugated phalloidin for one hour at 37ºC. Images were acquired on an Eclipse Ti-E inverted microscope with an integrated C2 laser scanning confocal system or an AI confocal microscope (Nikon).

3.1.1.4.3 Transmission electron microscopy (TEM). Devices were fixed in a solution containing 4% formaldehyde and 2.5% glutaraldehyde for 30 minutes at room temperature. Samples were transported to the Electron Microscopy Core at the University of Pennsylvania, where samples were postfixed in osmium tetroxide and embedded in amber. Thin sections were then mounted onto grids for examination in the TEM at the core.

3.1.1.5 Impedance spectroscopy and transendothelial electrical resistance (TEER) measurement.

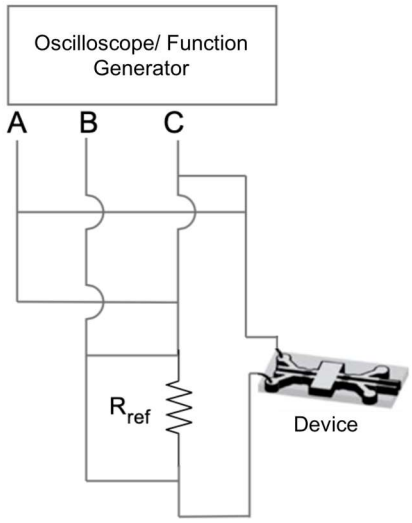

Figure 3. Circuit diagram for TEER measurements. Lead A measures the output of the oscilloscope. Lead B measures the voltage across the reference resistor. Lead C is the output voltage. R_{ref}= 460Ω.

Impedance measurements were performed using a Stringray DS1M12 USB oscilloscope adapter (USB Instruments). The circuit diagram is shown in Figure 3. Using the DS1M12 EasyScope II software, the output voltage (lead C) was set to a sine wave with 220-mV amplitude and varying frequency, with electrodes inserted into the input ports of the device so that the measured current passed across the endothelium. The leads of input A measured the voltage in lead C to monitor the output of the oscilloscope. The leads of input B measured the voltage across the reference resistor to determine the current passing through the device. The frequency of the output voltage was swept from 15 Hz to 15.6 kHz, with intermediate values of 50 Hz, 105 Hz, 558 Hz, and 3,906 Hz, to assure that the impedance followed a characteristic frequency dependence for cell monolayer measurements (Benson, Cramer, & Galla, 2013). The impedance was characterized by calculating the ratio of amplitudes between the applied voltage and measured current. Impedance was defined as Z = V/I where V is the voltage magnitude

and I is the current magnitude. TEER values were determined by taking the difference in impedance at 15 Hz, where the capacitance of the electrodes dominates the overall impedance, and 15,600 Hz, where the resistance of the culture medium is the primary component of the impedance. These TEER values were then subtracted by the impedance difference measured between the inlet and outlet of the blank acellular device containing only a hydrogel with cylindrical voids.

3.1.1.6 Micro-particle image velocimetry. For flow visualization studies, 1-μm beads tagged to fluoresce at several wavelengths were injected into the channels. A triggered LED light source was used to illuminate the beads within the channel at predefined pulses. The experiments were conducted on the stage of an inverted Eclipse Ti-E microscope (Nikon). Images were taken at 2000 fps, and ImageJ was used to quantify bead velocity as well as wall strain. Videos of the bead tracking can be found in the Videos attached to this thesis.

3.1.1.7. copGFP transfection. HCMEC/D3 were incubated overnight with lentiviral particles containing copGFP and a puromycin-resistance coding constructs using an MOI of 1 overnight. The following day, the cells were washed with PBS and incubated for a day in EGM. 10 mg/mL puromycin was then added to the cells for an additional three days. At day 4 of puromycin treatment, greater than approximately 90% of the cells expressed GFP.

3.1.2 Self-assembled microvasculature.

3.1.2.1 Microfluidic device fabrication. Microfluidic devices were fabricated using soft lithography in the same manner as for the pre-patterned vasculature described in section 3.1.1.1. Here, two differences were in the design of the device to accommodate

interstitial fluid flow perfusion and the fabrication of the central chamber to a height of 2 mm. This device schematic is shown in section 4.2.1.

3.1.2.2 Collagen/hyaluronan hydrogel formation. Microvessels were formed in collagen and hyaluronan (HA) composite hydrogels polymerized inside PDMS-based microfluidic devices. Passage 20-23 hCMEC/D3 and passage 7-15 GFP-labeled hBVP (Neuromics) were seeded in the hydrogels at densities of 2 M/mL and 0.4 M/mL, respectively. These ratios were obtained from a previous study that used co-cultures of human blood outgrowth endothelial cells and human pericytes to form microvasculature networks (Riemenschneider et al., 2016). hCMEC/D3 were cultured in mEGM and hBVP were cultured in DMEM (Corning) supplemented with 10% FBS, 1% penicillin-steptomycin, and 1X MEM Amino Acid Solution (Thermo Fisher). Hydrogels were bathed in mEGM and the final hydrogel formulation concentrations consisted of 3 mg/mL HA (Sigma), 5 mg/mL collagen type I (MP Biomedical), and 0.85-1 mg/mL Matrigel (Corning). These reagents were combined with 0.1 M sodium hydroxide (NaOH) and 10x phosphate buffer solution (PBS) to facilitate polymerization and maintain physiological pH.

3.1.2.3 Mechanical stimulation

3.1.2.3.1 Interstitial fluid flow. For control experiments, the cell-seeded collagen/HA gels were bathed in 8 mL of mEGM and placed in the incubator for five days in static conditions. For gels exposed to interstitial fluid flow, the input flow port of the microfluidic device was attached to a 5 mL plastic syringe (BD) secured to a GenieTouch linear syringe pump (Kent Scientific). The syringe pump was set to deliver 0.72 µL/min volumetric flow rate, equivalent to a bulk 3-µm/s interstitial fluid flow

velocity, for a total of five days, to match previous alignment studies (Polacheck et al., 2011).

3.1.2.4 Barrier integrity verification.

3.1.2.4.1 Dextran exclusion permeability assay. Microfluidic devices of day 5 samples were secured to a 22 mm x 40 mm cover slip with super glue and transferred to the stage of the confocal microscope. Microvascular structures within the hydrogel were located using the brightfield prior to perfusion with 4-kDa FITC-dextran (1:250) at a flow rate of 2 μL/min. Individual confocal slices were captured every minute at approximately 8-10 different regions within the hydrogel. Images were processed using ImageJ software where the permeability was calculated using Equation 2 with a few modifications. To accommodate for interstitial dextran perfusion instead of intraluminal, the change in fluorescent intensity $\frac{dI}{dt}$ was measured inside the lumen and the maximum intensity I_0 was measured outside the lumen. To perform a negative control, 10 U/mL thrombin (Calbiochem) was added to the 4-kDa dextran solution perfusing the samples for 30 minutes.

3.1.2.4.2 Immunocytochemistry. To visualize the presence of tight junctions, samples were blocked in 3% BSA for 30 minutes at room temperature. Then the samples were incubated at 4 °C overnight with 1:250 primary antibody ZO-1 (Cell Signaling). The next day hydrogels were incubated at 37°C with 1:500 secondary antibody Cy-3 for 1 hour and visualized with the confocal microscope.

3.1.2.5 Quantification of alignment, length, and diameter. For hydrogels containing self-assembled vasculature, samples were fixed at room temperature for 20 minutes with 4% paraformaldehyde, permeabilized with 0.2% Triton X- 100 for 20

minutes, and then stained with 1:100 Texas Red-phalloidin (Biotium) and 1:500 DAPI. Samples were imaged with a laser scanning confocal microscope (Nikon C2), which was used to generate z-stacks that were then analyzed with Nikon Elements Analysis software. Microvessels were identified by the presence of a distinct, three-dimensional lumen. Microvessel length was measured by comparing the maximum projection and 3D volume views to determine the beginning and end microvessel positions. Microvessel alignment was measured using the reference angle tool (in the Nikon Elements Analysis software) with the reference angle dictated by the direction of the applied interstitial flow.

3.1.2.6 cd44 knockdown and quantification. HCAM siRNA (Santa Cruz Biotechnology) was used to knock down cd44 in the hCMEC/D3 cell line. hCMEC/D3 cells were seeded at a density of 2 $x10^5$ cells per well in a six well plate and then grown until confluent. Two solutions were prepared, solution A with 8 µL siRNA duplex diluted in 100 µL siRNA transfection medium and solution B with 8 µL of siRNA transfection reagent diluted in 100 µL siRNA transfection medium. The siRNA duplex solution was then mixed with the dilute transfection reagent and incubated at 15 minutes at room temperature. 0.8 mL of siRNA transfection medium was added to the siRNA transfection reagent mixture and then this solution was added to cells that were washed once with 2 mL of siRNA transfection medium. The cells were incubated for 5 hours at 37ºC in a 5% CO_2 incubator after which 1 mL of EGM containing 2% penicillin/streptomycin and 10% fetal bovine serum was added without removing the transfection mixture. The cells were incubated for an additional 18 hours after which they were used for experiments. To verify knockdown, cellular protein was isolated using digestion in sample buffer with reducing agent, and separated using SDS-PAGE. Following transfer, 0.45 µm PVDF

blots were incubated with an anti-cd44 primary (1:50) and horseradish peroxidase-conjugated secondary (1:4000) within an iBind Flex Western Device (Thermo Scientific). Blots were imaged in a chemiluminescent imager. To provide a loading control, gels were incubated in Coomassie Blue for 30 minutes following the transfer and representative bands were used to normalize blot signals.

3.1.2.7 Seeding hydrogels with neural progenitor cells.

Rat-derived E14 neural progenitor cells (NPC) were seeded within the co-culture of the GFP-labeled hBVP and hCMEC/D3 at a ratio of 1:2 with hCMEC/D3. NPC isolation and culture was performed at Drexel University. NPCs were derived from E14 transgenic Fischer 344 rats that express human placental AP marker. Embryonic cords were dissected and dissociated in 0.05% trypsin for 20 minutes at 37ºC. Cells were cultured for 3-10 days, prior to using for experiments, in DMEM supplemented with 1 mg/ml BSA (Sigma A9418), 20 µL/mL B27 (Life Tech. 12587-010), 10 ng/mL bGFG (Pepro Tech. 100-18B), 10 µL/mL N-2 (Life Tech. 17502-048) , and 10 ng/mL NT-3 (Pepro Tech. 450-03) on poly-l-lysine and laminin coated dishes (Medalha, Jin, Yamagami, Haas, & Fischer, 2014). Hydrogels were perfused with mEGM supplemented with 20 µg/mL NT-3 growth factor (PeproTech) to maintain the viability of NPCs and facilitate their differentiation to neuronal restricted precursors (NRP), distinguished by positive staining for Tuj-1.

Hydrogels seeded with rat-derived neural progenitor cells (NPC) were stained to visualize both the endothelial tight junctions and axons. All the following steps were done at room temperature. Hydrogels were blocked in 10% normal donkey serum (NDS) for 10 minutes followed by incubation with 1:500 Tuj-1 801201 (Biolegend), 1:250 ZO-

1, and 2% NDS for 2 hours. Hydrogels were then incubated with 1:500 DyLight 650 conjugate, 1:500 Cy-3, and 2% NDS for 1 hour. Positive branches extending from each Tuj-positive axon were identified by subtracting the 640 nm Cy5 signal (Tuj-1) from both the 561 nm TRITC (ZO-1) and the 488 nm GFP signals. These branches were then totaled using the counter option in the Nikon Elements software and compared between flow and static samples.

3.1.2.8 Scaffold transplantation in vivo.

3.1.2.8.1 Hemisection spinal cord injury model. For the in vivo transplantation, the collagen concentration was reduced to 2.5 mg/mL to increase axon permissivity. Day 2 scaffolds (either exposed to flow or static conditions) were transplanted into acute animal hemisection spinal cord injury model by aspiration at the level of the fourth cervical vertebrae of the spinal cord 1-mm lateral of the midline from the posterior side. In total, 4 female adult Sprague-Dawley rats (225-250 g) were used. Surgeries were conducted at the Drexel University Queen Lane Medical Campus in accordance with the IACUC agreement, which was approved by the Drexel College of Medicine Institutional Review Board. Animals were administered cyclosporine three days prior to surgery and during the 3-week experiment as a means to minimize host inflammatory response. Following transplantation, animals were caged in their normal environments with normal food and water intake. Animals were sacrificed three weeks after transplantation and immunohistochemistry was performed to process the data using serial 8-μm sagittal sections. These sections were stained using 1:250 anti-ZO-1 D7D12 (Cell Signaling), 1:1000 anti-GFAP (Chemicon), 1:500 anti-RECA (AbD Serotec), and 1:20000 anti-5-HT (Immunostar). These sections were then visualized in a confocal microscope, and stacks

were concatenated to form a three-dimensional rendering of the transplant. These 3D renderings were used to measure both microvessel and axon length to account for extensions out-of-plane from single sagittal sections and to assure that the measurements were representative of their full lengths.

3.1.3 Vascularized self-assembling peptide hydrogels.

3.1.3.1 Microfluidic device fabrication. The fabrication of the microfluidic device involved using a rectangular PDMS stamp that had rectangular 4 mm x 6 mm dimensions and a thickness of 0.5 mm. The positive-featured stamp was covered with 1 mL of uncured PDMS. Air bubbles were removed using a desiccator under vacuum for 5 minutes. The uncured PDMS-covered stamp was then inverted onto a 4 cm by 6 cm glass slide with a thin layer of PDMS created by spinning at 1,000 rpm for 15 seconds and baked at 150ºC for 3 minutes. The inverted PDMS covered stamp on the glass slide was baked at 150ºC for 7 minutes. After gently peeling the stamp from the glass slide, the negative mold for the peptide hydrogel was plasma oxidized at 25% power for 20 seconds. This oxidized negative mold was then placed on an approximately 100-µm thick PDMS covered 4 cm by 6 cm glass slide that had been prepared in the following way. The PDMS layer was spun at 1,000 rpm for 15 seconds and baked at 150ºC for 3 minutes. Additional PDMS was added on top of the cured PDMS layer and spun at 1,000 rpm for 15 seconds. The non-cured second PDMS layer made direct contact with the oxidized negative mold which was baked at 150ºC for 7 minutes. At this stage the PDMS device had a closed central chamber that was inverted onto a 22 mm by 22 mm cover slip and baked at 150ºC for 30 minutes. After complete polymerization of the PDMS device, nine ports were punctured in the thin PDMS layer above the central chamber to facilitate

hydrogel gelation. The same protocol described in section 3.1.1 was used to facilitate gel attachment: 10-N sulfuric acid was injected into the central chamber for 90 minutes and then washed 5 times with distilled water prior to the addition of diluted collagen.

3.1.3.2 RADA 16-I peptide hydrogel formation. Microvessels were fabricated in RADA 16-I self-assembling synthetic peptide hydrogels within PDMS-based microfluidic devices. Passage 20-23 hCMEC/d3 and passage 7-15 GFP-labeled hBVP were seeded at the same densities of 2 M/mL and 0.4 M/mL, respectively (same densities as within the collagen/HA-based hydrogels). In addition, for some experiments only passage 20-23 GFP-labeled hCMEC/d3 were seeded within the peptide hydrogels. The desired cell seeding density was suspended in 20% cell sucrose solution which was mixed with an equal volume of 2 mg/mL peptide (1:1 ratio). The final hydrogel formulation consisted of 10 % sucrose and 1 mg/mL peptide. This solution was injected into the microfluidic central chamber followed by the careful addition of 8 mL mEGM containing 10 % FBS and transferred to a 37ºC incubator. After 1 hour the EGM was replaced with 8 mL mEGM containing 100 ng/mL VEGF and 50 ng/mL PMA. The cell seeded peptide hydrogels were stored at 37ºC for 5 days.

3.1.3.3 Barrier integrity verification.

3.1.3.3.1 Dextran exclusion permeability assay. To assess barrier function within the vascular structures, 500 µL of 2-MDa dextran was pipetted on the surface of the microfluidic device containing the cellular peptide gel to test the integrity of tight junctions of endothelial cells. Images were taken on a Nikon A1 confocal microscope at intervals of 10 seconds for 15 minutes at different z depths. The images were then imported to ImageJ for analysis. The permeability coefficients were quantified using a

modified version of Equation 2. Briefly, assuming the dextran concentration remains constant in the surroundings and the cylindrical geometry of the vessels, permeability coefficients can be calculated from the flux of solute across an area of the capillary using Fick's First Law of Diffusion. Here, assuming a fixed concentration outside the vessels, the dextran concentration was directly correlated with fluorescent intensity yielding the following equation for permeability coefficient: $P = \frac{r}{2I_o}\frac{dI}{dt}$, where dI/dt is the change of fluorescent intensity inside the lumen, r is the radius of the vessel, and I_o is the maximum intensity through the duration of the experiment.

3.1.3.3.2 Immunocytochemistry. Devices were fixed in 4% paraformaldehyde at room temperature for 20 minutes. Afterwards, cellular peptide hydrogels were permeabilized with of 0.2% Triton X-100 (Sigma) for 30 minutes at room temperature. Peptide hydrogels were then removed from the central chamber of the devices and blocked by either goat or donkey secondary antibodies in 5% donkey serum or 3% bovine serum albumin (BSA) for 30 minutes at 37℃. These permeabilized hydrogels were incubated with 1:250 anti-ZO-1 (Cell Signaling) overnight at 4℃. These gels were then washed thoroughly in PBS and incubated with 1:500 DAPI and 1:10 Alexa Fluor phalloidin at 37℃ for one hour. Images were acquired on a Nikon A1 laser scanning confocal microscope

3.1.3.4 Scaffold transplantation in vivo.

3.1.3.4.1 Compression spinal cord injury model. First, isoflurane was used to anesthetize eight 250-250g female Sprague Dawley rats after which a laminectomy was performed at the C4-C5 cervical segments. Then, a force of 150,000 Dynes was applied using the IH Infinity Horizontal Impactor (Lexington) after which a single black suture

was added next to the contusion epicenter to easily locate the lesion site during the peptide injection one week later. The muscle and skin layers were closed in layers followed by 8-10 staples to the dermis. One week later the animals were placed in a stereotaxic frame and the compressed spinal cord was exposed. Using the Micro Syringe Pump (Micro4), 10 uL of hCMEC/d3 and hBVP cells at a ratio of 5:1 were injected into the lesioned spinal cord in a final matrix composition of 1 mg/mL RADA-16-I peptide and 10% sucrose. The surgical syringe had a 30G needle and the flow rate of the injection was 100 nL/s. The needle tip was left inside the spinal cord for 1 minute after the contents were completely injected. In addition, 20 µL Matrigel was injected on the dura over the injection location to assure that the peptide hydrogel remained in the spinal cord parenchyma. Animals were sacrificed two weeks after injections and immunohistochemistry was performed on the spinal cords using serial 8-µm sagittal sections. Detailed protocol can be found in section 6.1.18.

3.1.4 Statistics.

The open source statistics package, R, was used to perform all statistical calculations. Statistical significance was calculated using Welch Two Sample t-test, unless otherwise specified. Two sample t-tests were used to compare measurements of permeability coefficients, and one-way ANOVAs with post-hoc Tukey tests were used to determine statistical significance for the TEER measurements. Statistical significance of the microvessel alignment data was calculated using one-way ANOVA and post-hoc Tukey's HSD tests. Statistical significance was denoted with p-values less than 0.05. Each in vivo condition (four animals total) is averaged from at least 5 histological

sections per condition. Figure captions contain the sample number for the in vitro measurements.

Chapter IV

Results

4.1 Fabrication and Initial Transplantation Attempts of Compliant 3D Models of the Blood-Brain Barrier

4.1.1 Fabrication of a compliant 3D in vitro model of CNS vasculature.

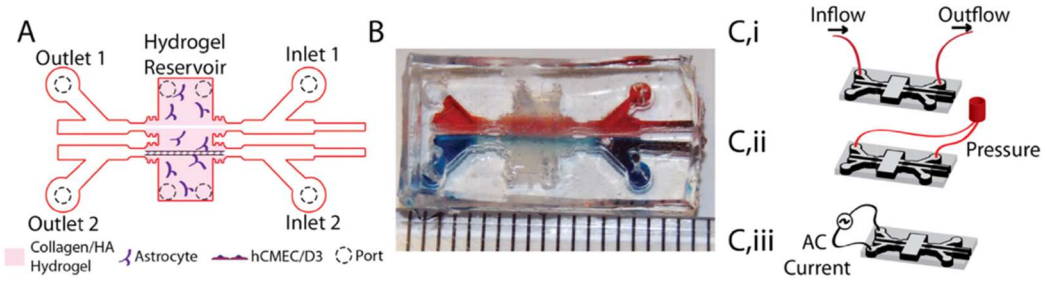

Figure 4. CNS vessel model. A) Schematic of microfluidic device detailing the location of inlet/outlet ports as well as ports to fill the hydrogel reservoir. B) Picture of the device with food dye injected into the two channels. C) Testing configurations i) application of fluid flow, ii) cyclic strain stimulation and iii) TEER measurements.

A microfluidic device was constructed to fabricate a 3D vascular structure exhibiting barrier integrity appropriate for the CNS. Fig. 4A shows a schematic of the device and the location of the endothelial channel (herein referred to as a vessel) within the hydrogel. The device featured two isolated compartments, indicated by perfusion with dye (Fig. 4B). The microfluidic device allowed for application of mechanical stimulation. Fluid flow and hydrostatic pressure-driven cyclic strain were applied by modulating the pressure at the inlet and outlet of the device (Fig. 4C,i and ii). Additionally, impedance spectroscopy non- invasively measured transendothelial electrical resistance (TEER) values through the inlet ports (Fig. 4C,iii).

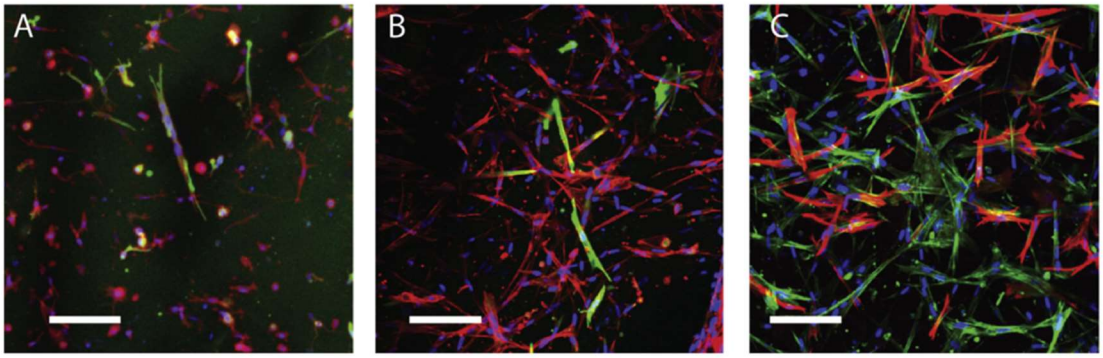

Figure 5. Astrocyte spreading in different hydrogel formulations and culturing conditions. A) Astrocytes embedded in 5 mg/mL collagen and cultured in AGM medium. B) Astrocytes embedded in 5 mg/mL collagen, 1 mg/mL HA, and 1 mg/mL Matrigel and cultured in AGM medium. C) Astroctyes embedded in the same hydrogel formulation used in (B) but cultured in mEGM medium. Green: anti-GFAP, red: phalloidin. Scale = 50 μm for all images.

A hydrogel formulation containing collagen type I, hyaluronan, and Matrigel shown to facilitate astrocyte migration and spreading (Placone et al., 2015) was used to increase the frequency of interactions between the astrocytes and endothelium. Fig. 3 indicates that presence of hyaluronan in the matrix substantially augments astrocyte spreading in the base collagen matrix (Fig. 5A and B). Incubation with mEGM substantially increased the activation of astrocytes, as evidenced by staining for glial fibrillary acidic protein (GFAP) in Fig. 5C, compared to astrocyte growth medium.

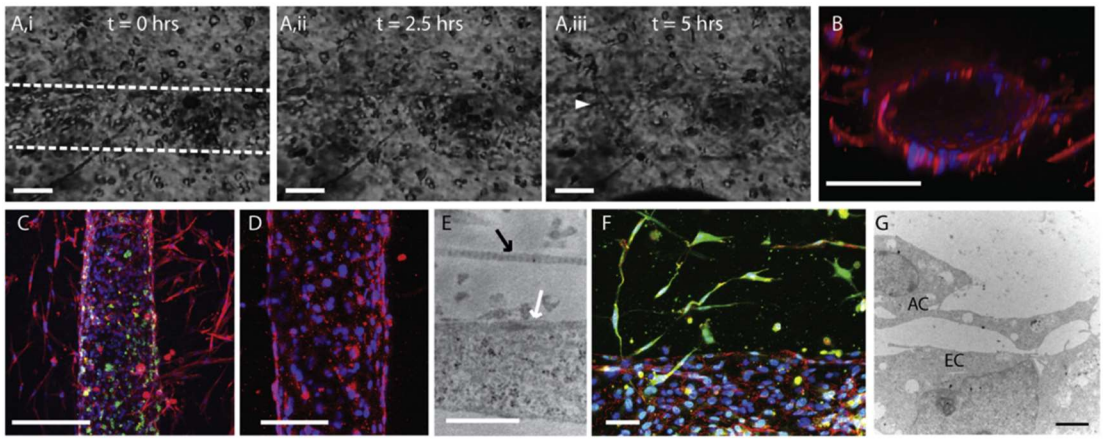

Figure 6. 3D model of the neurovascular model. A,i-iii) Brightfield time lapse of endothelial vessel formation, scale: 100 µm. B) Confocal stack of phalloidin and DAPI stain showing clear lumen within the endothelial monolayer with surrounding astrocytes, scale: 100 µm. C) Confocal stack with GFP-positive HCMEC/D3, scale: 100 µm. D) Confocal stack demonstrating positive laminin staining around the endothelial channel after four days in culture, scale: 100 µm. E) TEM micrograph demonstrating the presence of a basement membrane on the basal side of the endothelium (white arrow) surrounded by striated collagen fibrils (black arrow), scale: 500 nm. F) Confocal stack showing presence of astrocytes (stained green with anti-GFAP) surrounding the endothelial monolayer displaying tight junctions (red is anti-ZO-1), scale: 50 µm. G) TEM showing microstructure of interaction between astrocyte and the endothelial monolayer, scale: 2 µm.

Formation of the endothelial monolayer and its initial interaction with surrounding astrocytes occurred within several hours of co-culture, as indicated by time lapse images in Fig. 6A. Confocal microscopy demonstrated a discrete lumen surrounded by astrocyte processes, which is evident in the confocal stack shown in Fig. 6B. Transfecting the HCMEC/D3 cells to express copGFP confirmed that the endothelial cells lined the surface of the lumen (Fig. 6C). After four days in culture, the presence of a secreted basal lamina was apparent in confocal images of laminin immunostaining (Fig. 6D) as well as in transmission electron microscopy (TEM) micrographs (Fig. 6E).

Vessels also exhibited substantial astrocyte contact and BBB function as evidenced by staining for GFAP and zonula occludens-1 (ZO-1) (Fig. 6F). TEM also demonstrated the microstructure of the astrocyte/endothelial interaction. Astrocyte endfeet approached within ~100 nm of the basal side of the endothelial monolayer (Fig. 6G). These results demonstrate the ability of the model to mimic functional components of the blood- brain barrier including a tight junction-displaying endothelium, robust basement membrane, and interaction with surrounding astrocytes. Due to the diameter of these in vitro vessels, ranging from 180 to 220 μm, and lack of smooth muscle cells in their walls, the model represents a merger between a small arteriole and large capillary in the central nervous system.

4.1.2 Flow distribution characterization using microparticle image velocimetry.

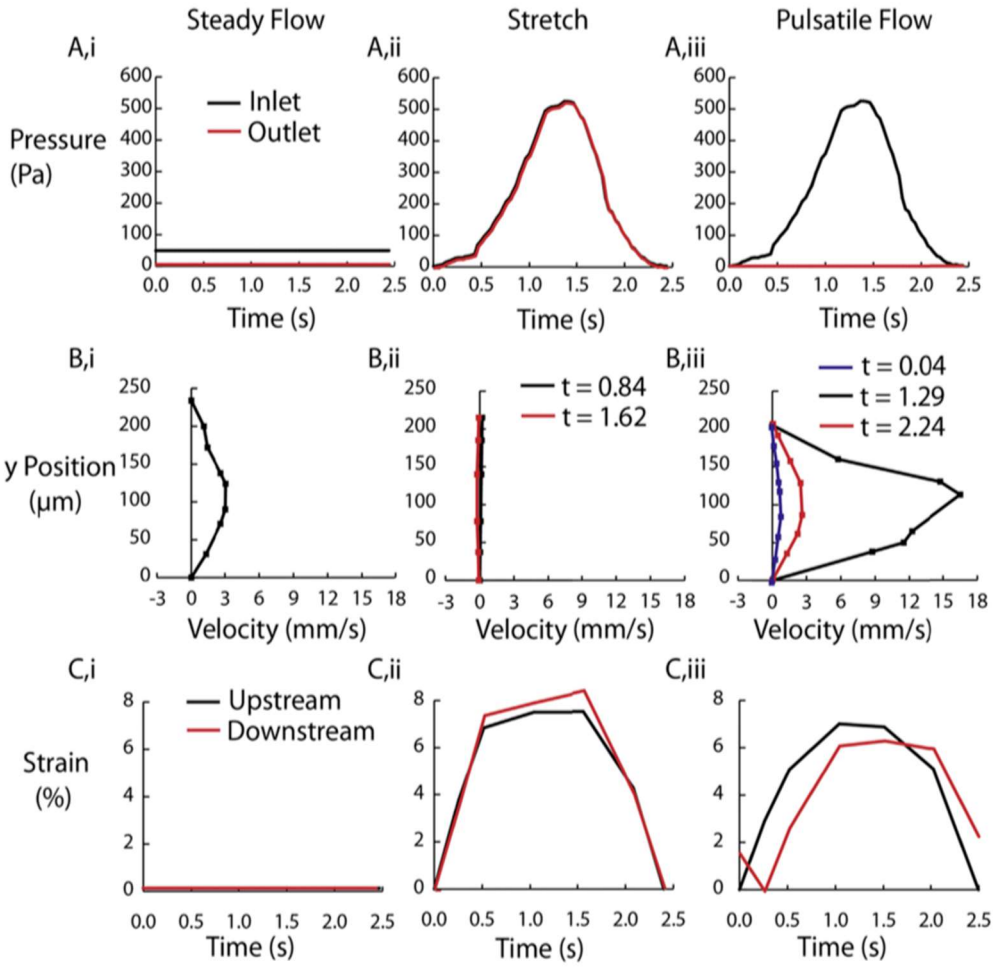

Figure 7. Shear and stretch application. A) Pressure profile at the inlet port for i) steady shear, ii) cyclic stretch, and iii) pulsatile flow conditions. B) Velocity profile within the lumen of the vessel measured by microparticle image velocimetry (mPIV) for i) steady shear, ii) cyclic stretch, and iii) pulsatile flow. C) Radial strain at two axial locations of the wall for i) steady shear, ii) cyclic stretch, and iii) pulsatile flow.

The configuration of the device allowed for application of several flow regimes to the in vitro BBB. To facilitate steady flow, a constant pressure was applied solely to the inlet (Fig. 7A,i). This condition generated laminar flow within the vessel; microparticle image velocimetry (μPIV) verified the presence of a parabolic velocity profile (Fig. 7B,i) and a shear rate corresponding to 0.5 dyn/ cm^2 of shear stress, consistent with the

magnitude predicted by Poiseuille's Law. As expected, the steady application of fluid flow did not result in any measurable radial strain in the vessel wall (Fig. 7C,i). A video of the flow generated by constant pressure can be found in Video 1.

In order to distinguish the effect of cyclic stretch from shear stress, the inlet and outlet pressures were balanced so that no pressure gradient was applied along the length of the vessel. Fig. 7A,ii indicates the pressure at the inlet and outlet during cyclic strain application. Due to a negligible pressure gradient along the length of the vessel, μPIV measured minimal fluid flow (Fig. 7B,ii). The radial strain varied between 0 and 7.8 ± 0.4% at the same frequency of the applied pressure (Fig. 7C,ii). The lack of fluid flow during strain application can be seen in Video 2. The data also indicated no phase change in the strain waveform of two axial positions along the vessel, suggesting homogeneous cyclic strain with zero pulse wave propagation.

Application of pulsatile pressure to the inlet facilitated fluid flow combined with strain (Fig. 7A,iii). This condition generated the quasi-steady laminar flow profile depicted in Fig. 7B,iii. Measuring the strain waveforms at two different axial locations revealed out- of-phase strain profiles, indicative of a pulse wave traveling axially along the vessel (Fig. 7C,iii). Video 3 provides visual evidence of the pulsatile flow field. The average speed of the pulse wave was calculated to be 0.95 ± 0.51 mm/s. Additionally, the calculated Womersley number was 0.004, comparable to capillary levels in vivo (Kassab, Le, & Fung, 1999).

4.1.3 Vessel permeability characterization in response to mechanical stimulation.

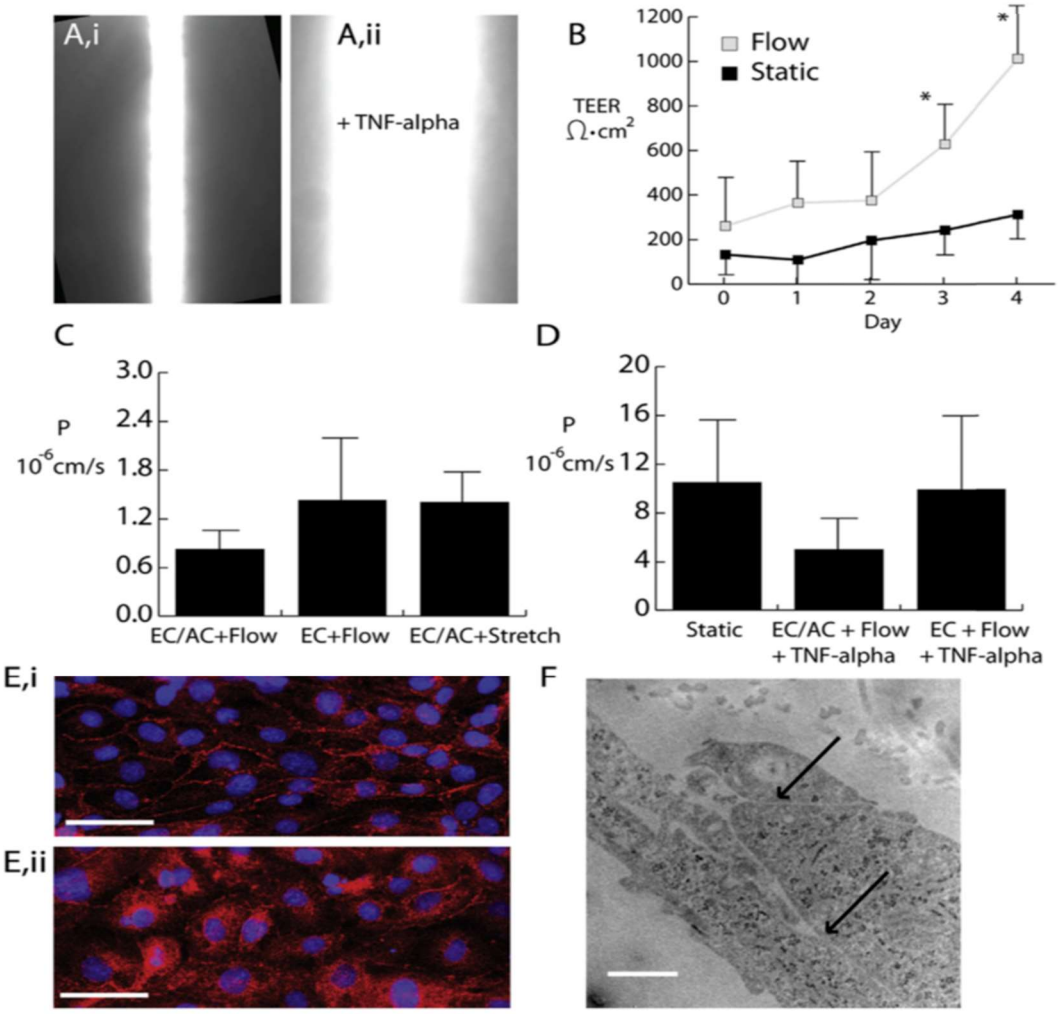

Figure 8. Effect of mechanical stimulation on blood-brain barrier formation. A) Images demonstrating the measurement of vessel permeability using 4 kDa FITC-dextran and the effect of the inflammatory cytokine, TNF- α. B) TEER measurements for channels exposed to static and shear testing conditions for four days, * $p < 0.05$C) Permeability coefficient measured from dextran experiments for endothelial channels exposed to shear with and without astrocytes, and endothelial cell/astrocyte cultures exposed to cyclic stretch. D) Permeability coefficient for static channels containing endothelial cells and astrocytes, as well as channels exposed to flow and TNF- α. E) ZO-1 staining of the endothelial wall (i) with shear and (ii) in static conditions, scale: 10 mm. F) TEM demonstrating the tightness of endothelial cell-cell junctions exposed to shear for 4 days (black arrows indicate adjacent cell membranes in contact), scale: 50 nm.

Having demonstrated the ability to apply controlled levels of shear stress and cyclic stretch, experiments were conducted to assess how these mechanical stimuli affected BBB formation and its structural and functional integrity. Initial barrier functional assessment utilized perfusion of 4 kDa FITC-dextran using a previously described technique for quantifying vessel permeability in 3D (Bagley et al., 2015; Smith et al., 2016). Fig. 8A demonstrates the ability of this method to capture the barrier-disrupting effect of 20 ng/mL tissue necrosis factor a (TNF- α), a potent inflammatory cytokine, in channels exposed to shear stress for four days prior to TNF-α treatment. In order to determine the minimal incubation time required to test permeability, TEER values were measured in vessels either incubated under static conditions or exposed to 0.5 dyn/cm2 shear stress. In vessels exposed to shear stress, the TEER values began to significantly increase compared to static levels by day 3 (Fig. 8B). These TEER values exceeded previous measurements of in vitro monolayers by nearly one order of magnitude, possibly due to the additional impedance generated by the hydrogel. Fig. 8C provides the results of the dextran permeability testing for the various testing conditions at day 4. Both shear stress and cyclic stretch significantly decreased the barrier permeability compared to static controls to values consistent with other 3D models (Herland et al., 2016), and on the order of magnitude of measurements made in animal models (Yuan et al., 2006). Furthermore, shear stress decreased the permeability of the endothelium in the absence of astrocytes in the hydrogel, suggesting that astrocytic endfeet are not required for BBB function. Treatment with TNF- α increased barrier permeability to level comparable to the static condition, with or without the presence of astrocytes (Fig. 8D).

Fig. 8E exhibits confocal image stacks of the vessel wall exposed to shear and static conditions. In vessels exposed to shear stress, ZO-1 co-localized primarily to the lateral cell membranes indicating an intact endothelial barrier. In contrast, the ZO-1 staining was more diffuse in the static sample and revealed fenestration-like gaps along these endothelial membranes. Fig. 8F provides further confirmation of an intact membrane barrier by demonstrating tight junctions along the lateral cell membranes using TEM. The gap between adjacent endothelial cells was on the scale of 10 nm along the length of these junctions, which is substantially smaller than gaps measured in previous models using non-cerebral endothelial cells (Galie et al., 2014).

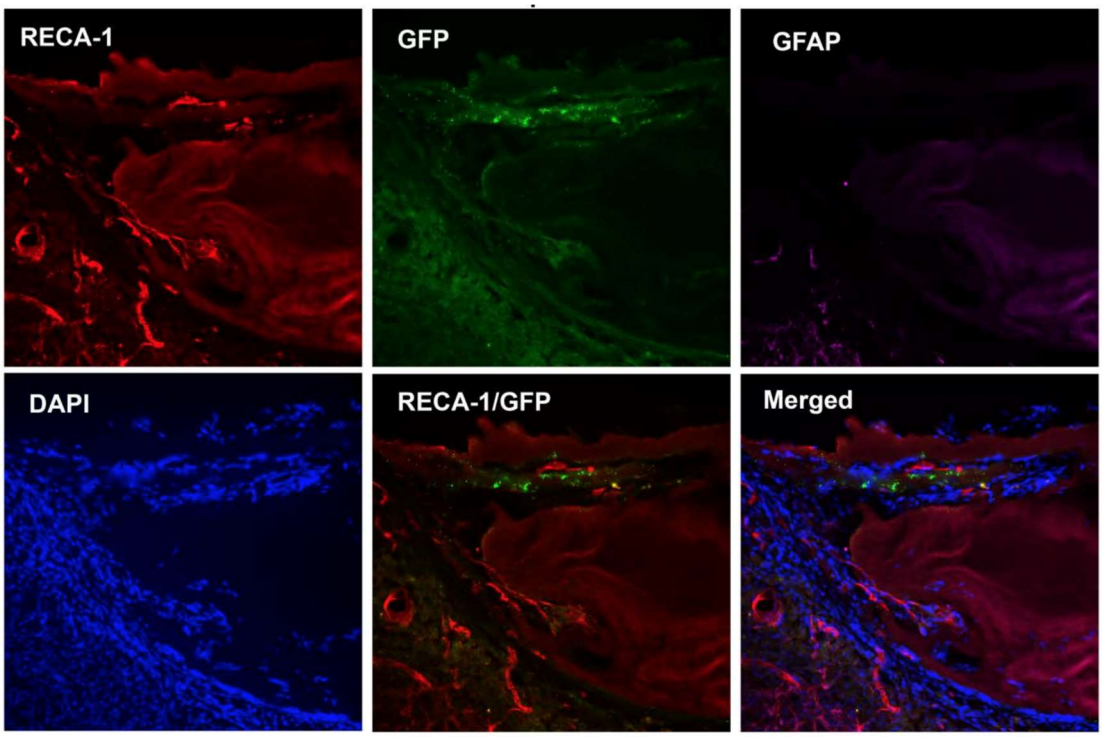

Figure 9. Blood vessel infiltration within transplants of pre-vascularized scaffolds. RECA-1: host blood vessel. GFP: transplanted hCMEC/d3 cells. GFAP: glial scarring. DAPI: cell nuclei.

4.1.4 Transplantation of pre-patterned vasculature. A pilot study was conducted to determine the effectiveness of guiding host axons using pre-patterned vascular scaffolds in a SCI injury model. 180-µm diameter vessels were fabricated within collagen/HA based scaffolds and transplanted at day 5 in vitro until BBB-integrity vasculature was established. Three weeks after transplantations the rats were sacrificed and IHC staining was obtained with the results shown in Figures 9 and 10. Instead of serving as an axon guidance channel and a vasculature model capable of anastomosing with the host vessels, the results indicated that both axons (SCG-10 and GAP-43 positive) and blood vessels (RECA-1) infiltrated the 180-µm diameter vessels. These results suggested that the 180-µm diameter vessels had a diameter that was too large to be compatible with the approximately 25-µm host vessels.

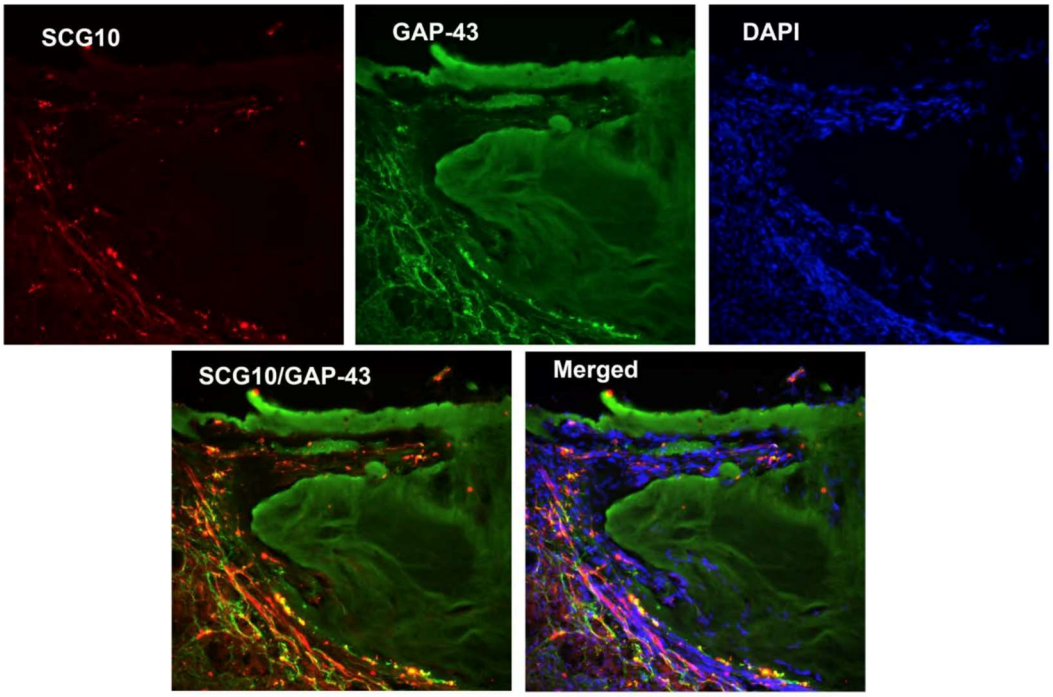

Figure 10. Axon infiltration within transplants of pre-vascularized scaffolds. SCG-10: regenerating sensory axons. GAP-43: axonal regeneration protein. DAPI: cell nuclei.

4.2 Control of Neurovascular Interaction to Guide Axon Growth.

4.2.1 3D in vitro microvessel formation and alignment.

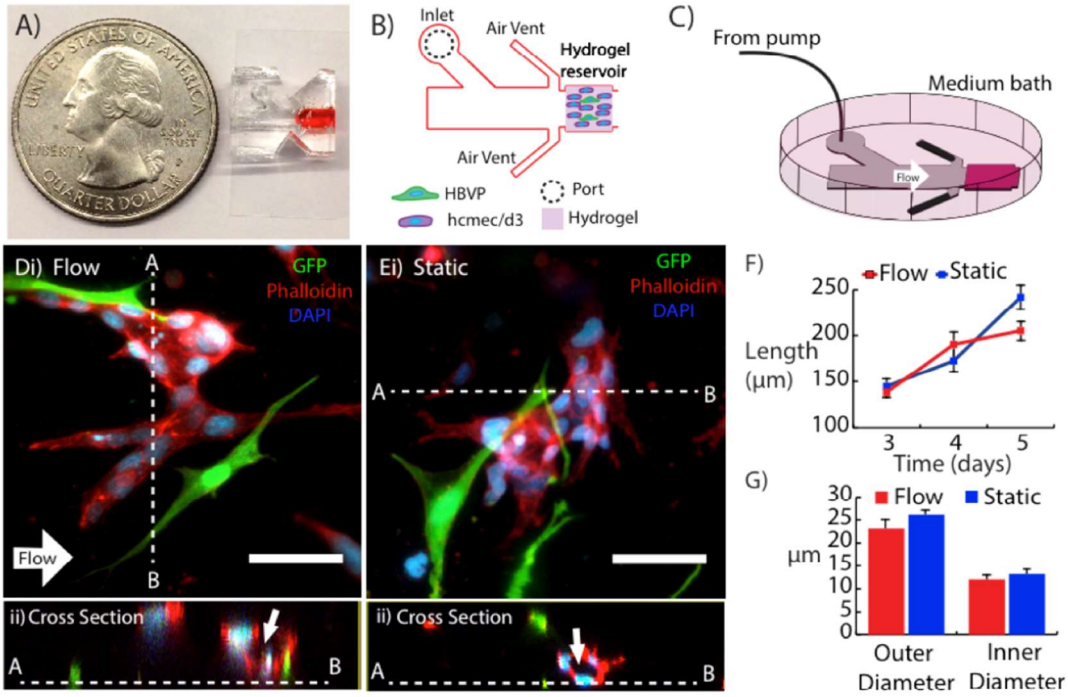

Figure 11. 3D in vitro microvessel formation. Microfluidic device A) photograph, B) schematic, and C) setup for flow. D) Microvessel exposed to interstitial fluid flow (direction denoted by white arrow) with cross section (white dashed line) showing lumen (ii). Ei) Microvessel from static control with cross section showing lumen (arrow) (ii). F-G) Microvessel length and diameter as a function of time. GFP hBVP (green), Phalloidin-Texas Red (red), and DAPI (blue). Scale bars, 50 μm. Data are presented as mean ± s.e.m. Length values (n = 15) and diameter values (n = 5) are from single hydrogel samples per condition.

Having observed that the pre-patterned vessels did not remain viable in vivo, experiments were conducted to form microvascular structures within collagen-based hydrogels. Composite hydrogels consisting of 5-mg/mL type 1 collagen and 3-mg/mL hyaluronan were polymerized within a perfusable microfluidic device (Fig. 11A-B). The devices were connected to a syringe pump and submersed in a well plate filled with culture medium (Fig. 11C). After 2-3 days in culture, the co-culture of pericytes and

cerebral-derived endothelial cells formed multi- cellular structures within the hydrogel in both perfused (3 μm/s interstitial flow velocity) and static conditions (Fig. 11Di-Ei). Between days 3 and 5, these multi-cellular structures displayed continuous lumens visible during confocal imaging (Fig. 11Dii-Eii), and are hereafter referred to as microvessels. Measurements indicated that application of interstitial fluid flow did not have a significant effect on either the length (Fig. 11F) or diameter (Fig. 11G) of the microvessels. After five days, the microvessel length extended to approximately 200-250 μm. The lumen diameter ranged from 12-13 μm, which is within the range of physiological values for microvasculature (Maslov, Zhang, Hu, & Wang, 2008).

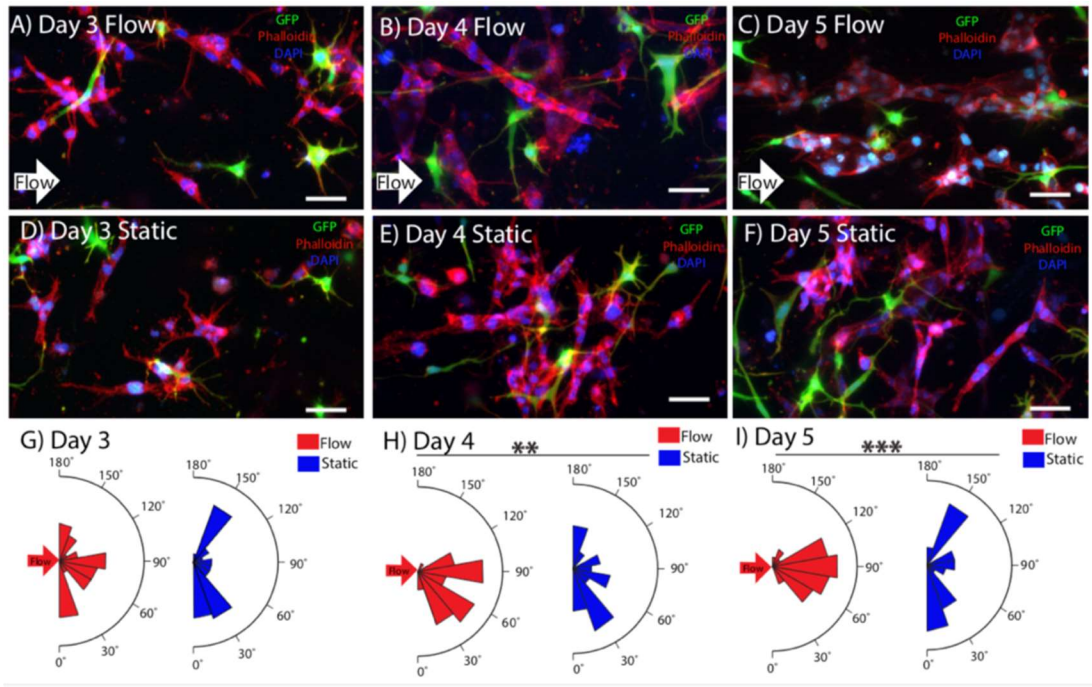

Figure 12. 3D Microvessel alignment with interstitial fluid flow. Microvessel alignment with flow (direction denoted by white arrow) at day 3 (A), day 4 (B), and day 5 (C). Microvessel orientation in static conditions for day 3 (D), day 4 (E), and day 5 (F). Microvessel alignment plots over time for day 3 (G), day 4 (H), and day 5 (I). GFP hBVP (green), Phalloidin-Texas Red (red), and DAPI (blue). Scale bars, 50 μm. Data are presented as mean ± s.e.m. **P<0.01, ***P<0.001; statistical significance was calculated using ANOVA and post-hoc Tukey's HSD test. Alignment values (n = 30) are from single hydrogel samples per condition.

Having demonstrated the ability to create capillary-scale microvessels within the scaffold, experiments were conducted to determine the effect of interstitial flow on alignment. We observed that application of interstitial fluid flow had a significant effect on vascular alignment. Figure 12Ai-iii shows microvessel orientation within hydrogels exposed to flow between days 3 and day 5, and Figure 12Bi-iii shows vessels exposed to static conditions over that timespan. Microvessels exposed to flow had significantly higher levels of alignment in the flow direction. Quantification of the angle between the long axis of the microvessel and the flow direction (Fig. 12C-E) indicated that alignment of vessels exposed to flow was significantly higher at day 5 compared to day 3. A significant difference between flow and static conditions was also observed at day 4 and day 5.

4.2.2 Disruption of flow-mediated alignment by disrupting cd44.

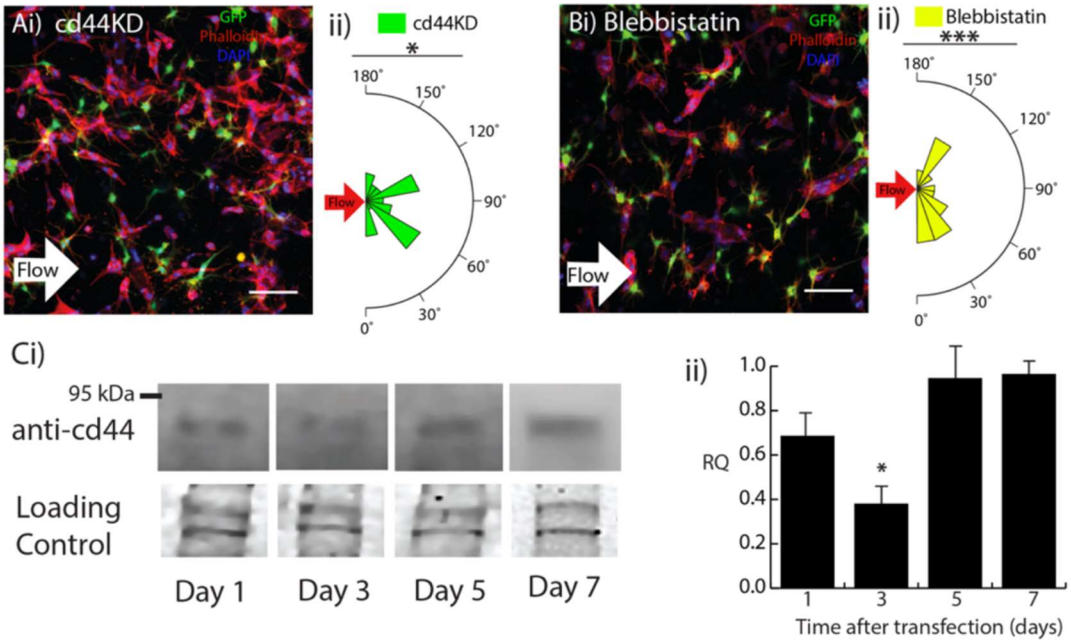

Figure 13. Disruption of 3D microvessel alignment. Ai) Day 5 scaffold exposed to interstitial fluid flow (direction denoted by white arrow) with hCMEC/D3 cd44KD cells and microvessel alignment plot (ii). Bi) Day 5 hydrogel exposed to interstitial fluid flow with 0.5 μM blebbistatin and microvessel alignment plot (ii). GFP hBVP (green), Phalloidin-Texas Red (red), and DAPI (blue). Scale bars, 100 μm. C) Western blot of cd44 protein expression levels from day 1 after transfection to day 7 (normalized to day 7 values). Coomassie blue was used to control for gel loading. Data are presented as mean ± s.e.m. *P<0.05, ***P<0.001; statistical significance was calculated using Welch Two Sample t-test. Alignment values (n = 30) are from single

In order to provide additional control over vascular alignment, experiments were conducted to identify the mechanisms underlying flow-induced alignment. Perfusion with interstitial fluid flow exerts a shear stress on the endothelial cells, so we investigated potential mechanosensors that could mediate the morphological response. Given that hyaluronan is a primary component of the scaffold and that previous studies have identified its primary receptor, cd44, as a contributor to shear stress mechanotransduction (Galie, van Oosten, Chen, & Janmey, 2015), siRNA was used to

knockdown cd44 expression levels in the endothelial cells. Knockdown of cd44 (cd44KD) resulted in disruption of the alignment of microvessels exposed to interstitial fluid flow for five days (Fig. 13A,i). Figure 13A,ii provides quantification of the alignment. To further implicate cd44, which is known to act through Rho/ROCK signaling (Kovacs, Toth, Hetenyi, Malnasi-Csizmadia, & Sellers, 2004; Liu et al., 2010), the effect of low concentrations of blebbistatin (0.5 μM) on alignment was evaluated. Confocal imaging showed disruption of alignment after attenuating myosin II-mediated contractility (Fig. 13B,i). Figure 13B,ii indicates that blebbistatin treatment also resulted in significant decreases in microvessel alignment in response to interstitial fluid flow. Neither the cd44KD or the blebbistatin conditions affected the microvessel length (Fig. 14Ai) compared to normal conditions perfused with flow. However, the microvessel outer diameter for the blebbistatin condition and the inner diameter for both the cd44KD and blebbistatin conditions were significantly lower (Fig. 14ii). The dynamics and validation of the cd44 knockdown were evaluated using Western blotting (Fig. 13Ci), which indicated that the highest knockdown (~40% of Day 7 value) occurred at day 3 (Fig. 13Cii), which is consistent with the finding that alignment occurs between days 3 and 5.

4.2.3 Blood-spinal cord barrier-integrity evaluation.

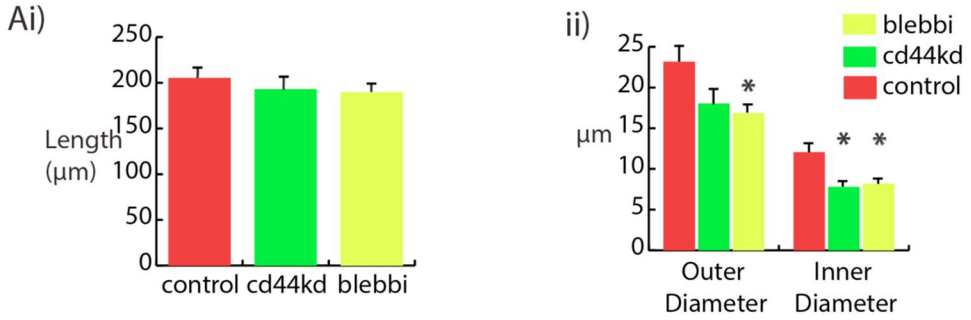

Figure 14. Microvascular morphology in the cd44KD and blebbistatin conditions compared to controls. Ai) Comparison of microvessel length and Aii) microvessel diameter of cd44KD and blebbistatin conditions to normal day 5 perfused hydrogels. Data are presented as mean ± s.e.m. *P<0.05; statistical significance was calculated using Welch Two Sample t-test. Length values (n=15) and diameter values (n = 5) are from single hydrogel samples per condition.

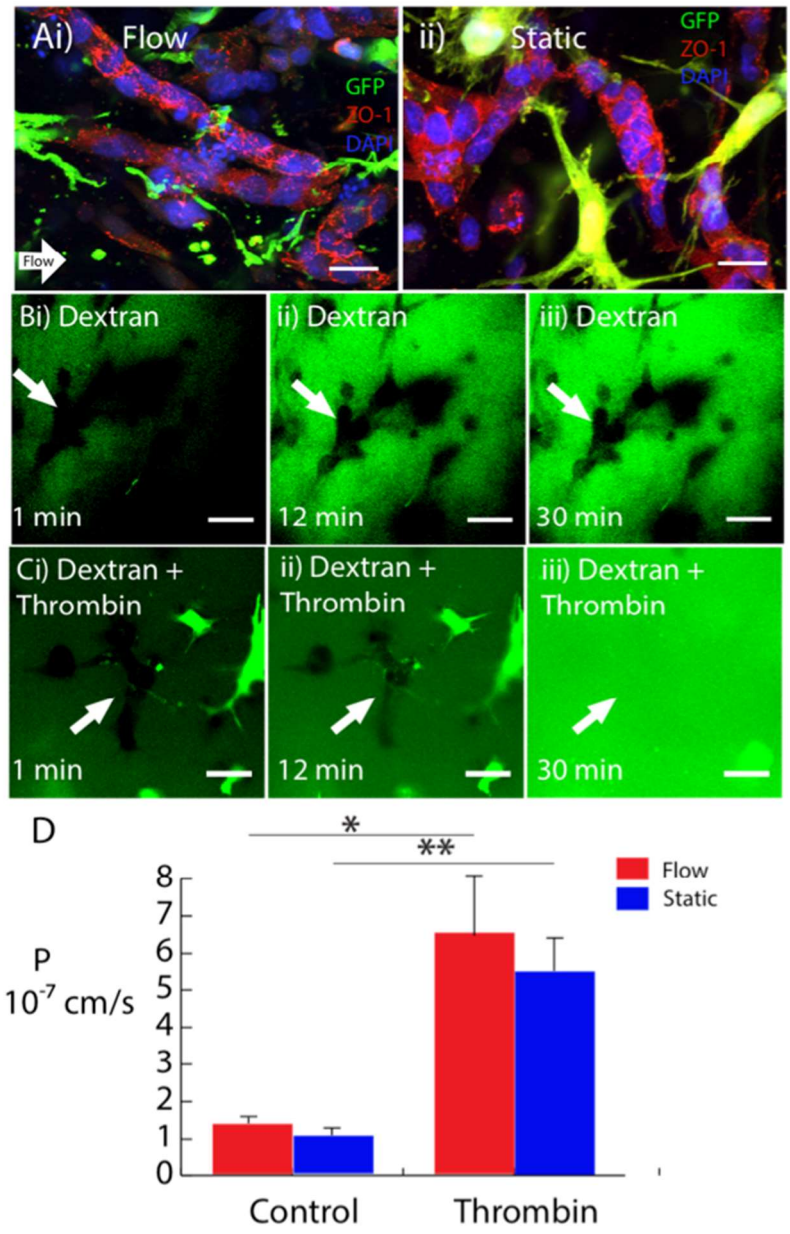

Figure 15. Blood-spinal cord barrier evaluation. A) Day 5 scaffold exhibiting ZO-1 (red) localization to the cell- cell junctions, pericytes (GFP), and nuclei (DAPI) for flow (i) and static (ii) conditions. B) 4-kDa FITC- dextran permeability test for static condition at i) 1 min, ii) 12 min, and iii) 30 min. C) 4-kDa FITC-dextran perfused with thrombin for static condition at i) 1 min, ii) 12 min, and iii) 30 min. D) Permeability values. Scale bars, 20 μm (A) and 50 μm (B-C). Data are presented as mean ± s.e.m. *P<0.05, **P<0.01; statistical significance was calculated using Welch Two Sample t-test.

The microvessel barrier integrity was evaluated using both immunostaining of tight junction proteins and a dextran diffusion assay developed for this study. Figure 15A demonstrates that the tight junction scaffolding protein, zonula-occludin-1 (ZO-1), localized to the cell-cell junctions of endothelial cells within the microvessels. The ZO-1 staining localized to the cell-cell junctions regardless of whether the microvessels were cultured under perfused or static conditions. To provide a more quantitative measure of the barrier integrity of the vessels, 4-kDa FITC-dextran was perfused through the bulk of the hydrogels and high scan-rate confocal microscopy was used to measure dextran exclusion from the vessel lumens (Fig. 15B). During the course of the 30-minute perfusion, dextran was mostly excluded from the microvessel lumen (Fig. 15Bi-iii). To provide a negative control, FITC-dextran was perfused with 10 U/mL thrombin (Fig. 15C) to disrupt barrier integrity. The thrombin eventually resulted in complete saturation of the vessel lumen with FITC-dextran during the same 30- minute span (Fig. 15Ci-iii). Figure 15D shows the permeability values calculated from these measurements, using the dextran fluorescence intensity as an indication of concentration. The measured values had magnitudes consistent with in vivo measurements (Yuan et al., 2006). As expected from the results of the immunofluorescence studies, no significant difference was observed between the permeability of microvessels exposed to perfused and static conditions.

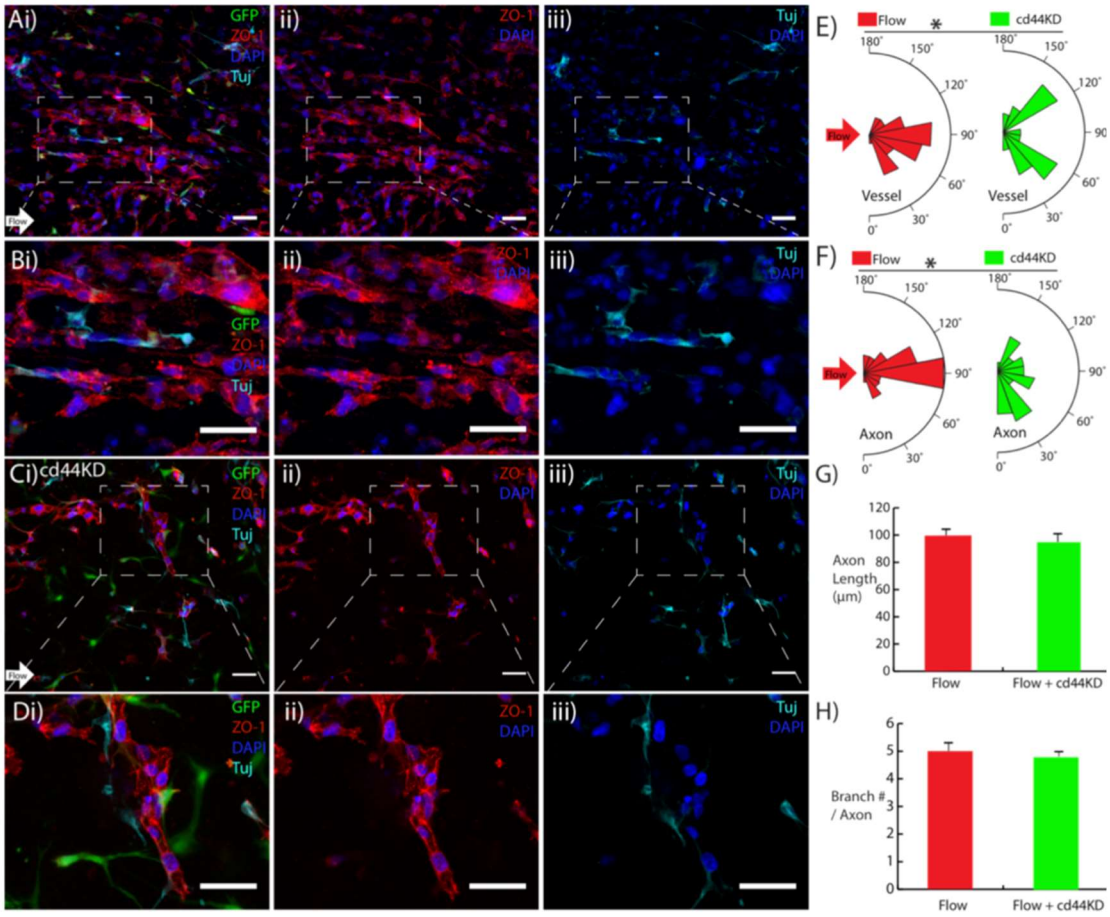

Figure 16. Patterned microvessels guide axons from NPCs in vitro Ai) Day 4 axon alignment with microvessels (direction denoted by white arrow), ii) ZO-1 tight junction stain (red), and iii) axons labeled with Tuj (cyan) for flow condition. B) Higher magnification images from A. Ci) Day 4 cd44KD with flow condition, ii) ZO-1 tight junction stain (red), and iii) Tuj-positive axons (cyan), GFP hBVP (green), DAPI (blue). D) Higher magnification images from C. E-F) Axon and vessel alignment quantification for flow and cd44KD conditions. G-H) Axon length and branch number for both flow and cd44KD conditions. Scale bars, 50 μm. Data are presented as mean ± s.e.m. *P<0.05 compared to untreated flow condition. Alignment values (n = 30), axon length values (n = 15), and branch number/ axon values (n = 5) are from single hydrogel samples per condition.

4.2.4 Patterned microvessels guide axons from neural progenitor cells (NPCs). To evaluate the ability of patterned microvessels to align axon growth along a prescribed direction, an initial in vitro experiment was conducted by seeding NPCs within the scaffold containing pericytes and cerebral-derived endothelial cells. Interstitial fluid flow containing neurotrophin-3 (NT-3) was applied to align the microvessels in the intended direction of axon growth and stimulate NPC differentiation to a neuronal phenotype. After four days of perfusion, Tuj-positive axons from the NPCs extended along the flow direction, parallel to the long axis of aligned microvessels. Figure 16A provides a low-magnification image of the aligned vessels labeled with ZO-1 adjacent to Tuj- positive axons extending from differentiated NPCs. Figure 16B focuses on one segment indicating that the axons aligned with the microvessels in the direction of perfusion. In Figure 16C, hydrogels seeded with cd44 knockdown endothelial cells were also exposed to interstitial fluid flow. Due to the disruption of cd44-mediated signaling, the flow-induced alignment was negated and the Tuj-positive axons no longer oriented in the direction of perfusion. Figure 16D provides a higher magnification image of this condition, indicating that the axons still exhibited close proximity to the microvessels, further suggesting that microvessels dictate axon orientation regardless of alignment. Quantification of both vessel and axon orientation (Fig. 16E- F) indicated significantly higher alignment in the direction of flow in cells without cd44 knockdown. Additionally, the length of Tuj-positive axons and the number of branches per axon were not significantly affected by cd44 knockdown (Fig. 16G-H).

4.2.5 Patterned microvessels guide host axons in an acute spinal cord injury (SCI) model.

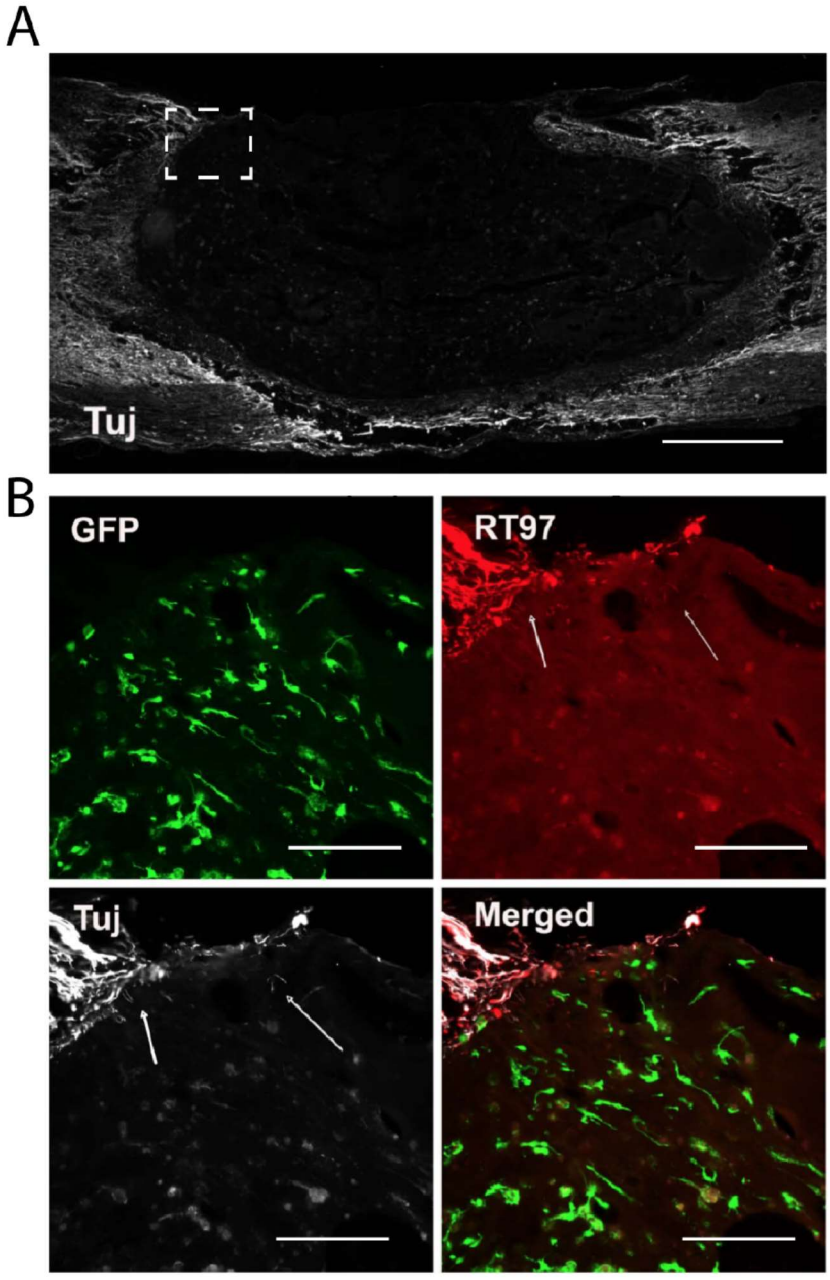

Figure 17. Transplantation of a scaffold containing 5 mg/mL collagen density. A) Low magnitude image showing a lack of axon infiltration in the location of the transplant following hemisection injury. Scale = 500 μm. B) A magnified image of the location denoted with dotted lines in panel A. White arrows show attenuated neurite infiltration labelled by both Tuj and RT97 staining. Scale = 100 μm.

Having demonstrated that aligned microvessels guide the direction of axons in vitro, an in vivo study was conducted to evaluate the efficacy of vascular-guided axon growth in a rat model of SCI. Cerebral-derived endothelial cells and pericytes were labeled with GFP to facilitate tracking after transplantation. An initial attempt with a scaffold containing 5 mg/mL collagen yielded little to no axon infiltration (Figure 17). Therefore, the scaffold composition used for this study consisted of 2 mg/mL collagen, 3 mg/mL hyaluronan, and 1 mg/mL Matrigel. These scaffolds were exposed to either flow or static conditions and delivered into an acute cervical hemisection injury, with the flow direction aligned with the rostral-caudal axis of the cord (Fig. 18Ai-iii). Three weeks after transplantation, immunohistochemistry was used to evaluate the viability and alignment of the transplanted microvessels as well as the presence and direction of host axons infiltrating the scaffold. Video 4 shows a confocal stack of several histological sections, indicating the incorporation of the transplanted scaffold. The microvessels aligned with flow remained aligned in the rostral-caudal axis after 3 weeks (Fig. 18Bi-ii). Additionally, Figure 18B,iii shows that Tuj-positive host axons infiltrated the scaffold along microvessels in the rostral-caudal direction. In order to determine if the host axon infiltration within the scaffold was regenerating or spared axons, the spinal cord sections were stained with CGRP. Positive CGRP axons were identified within the transplants three weeks after administration of the scaffolds (Figure 19), which suggests that the axons within the scaffold were regenerating and not spared axons.

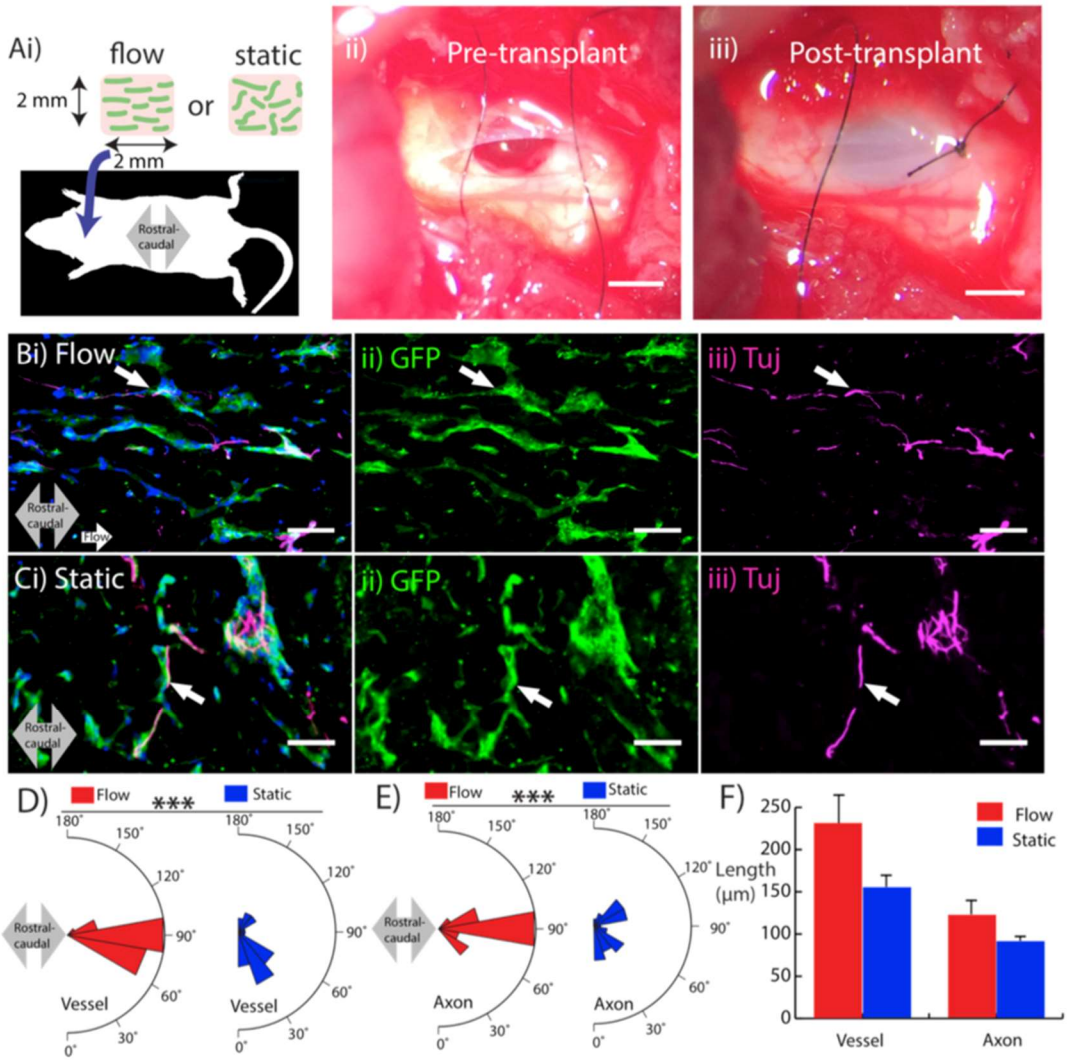

Figure 18. Axon guidance at the site of a cervical spinal cord injury in a rat model. Ai) Schematic illustrating transplantation of scaffold into a C-4 hemisection. The injury cavity is shown prior to (ii) and immediately following (iii) transplantation. Bi) Scaffold conditioned with flow exhibits viable GFP-labeled microvessels (green) (ii) and alignment of host axons (magenta) infiltrating the scaffold in the rostral-caudal direction (grey arrow). C) Scaffold conditioned in static conditions showing disrupted alignment of both microvessels (ii) and host axons (iii). D-F) Microvessel and axon plots showing alignment (D,E) and length (F). Scale bars, 1 mm (Aii,Aiii) and 50 μm (B-C). Data are presented as mean ± s.e.m. ***P<0.001; statistical significance was calculated using Welch Two Sample t-test. White arrows denote proximity of axons with microvessels. Microvessel alignment values (n = 30), axon alignment values (n = 30), microvessel length values (n=15), and axon length values (n = 15) are from single hydrogel samples per condition.

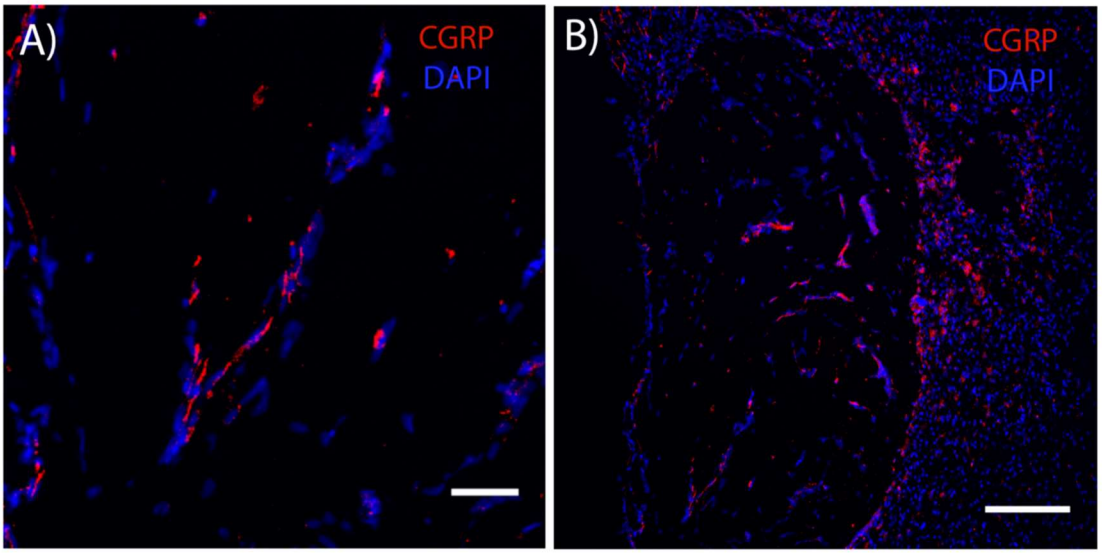

Figure 19. A) Regenerating axon (CGRP-positive) infiltration into the transplant three weeks after transplantation. B) Low magnitude image showing the orientation of the transplant relative to host tissue. Scale bars, 50 μm (A) and 200 μm (B).

In contrast, microvessels in the scaffold exposed to static conditions exhibited random alignment (Fig. 18Ci-ii) after transplantation. Though the scaffold instigated axon ingrowth, there was no significant alignment of the infiltrating axons with the rostral-caudal direction (Fig. 18C,iii). In both cases, the axons closely interacted with the microvessels with a high degree of spatial proximity, similar to the in vitro NPC experiments. Quantification indicated a significant increase in alignment with the rostral-caudal direction in the perfused scaffolds compared to static controls (Fig. 18D-E), though there was no difference in length of the microvessels and axons between the flow and static conditions (Fig. 18F). These results underscore the close interaction between vasculature and neural cells, and demonstrate that patterning microvessels with interstitial flow can be used to dictate the orientation of axon growth in vivo.

4.3 Self-Assembled Peptide Hydrogels Containing CNS Vasculature

The primary limitation of the collagen-based scaffold is its lack of incorporation into the host tissue and its level of permissivity to host axons. In order to address these caveats, the scaffold material was changed to a nanofiber self-assembling peptide. The RADA-16I self-assembling peptide was chosen due to previous studies demonstrating its permissivity to infiltrating axons in CNS injury models (Ellis-Behnke et al., 2006). The following section describes both in vitro and in vivo studies involving the RADA-16I self-assembling peptide.

4.3.1 Hydrogel microstructural analysis and storage modulus values.

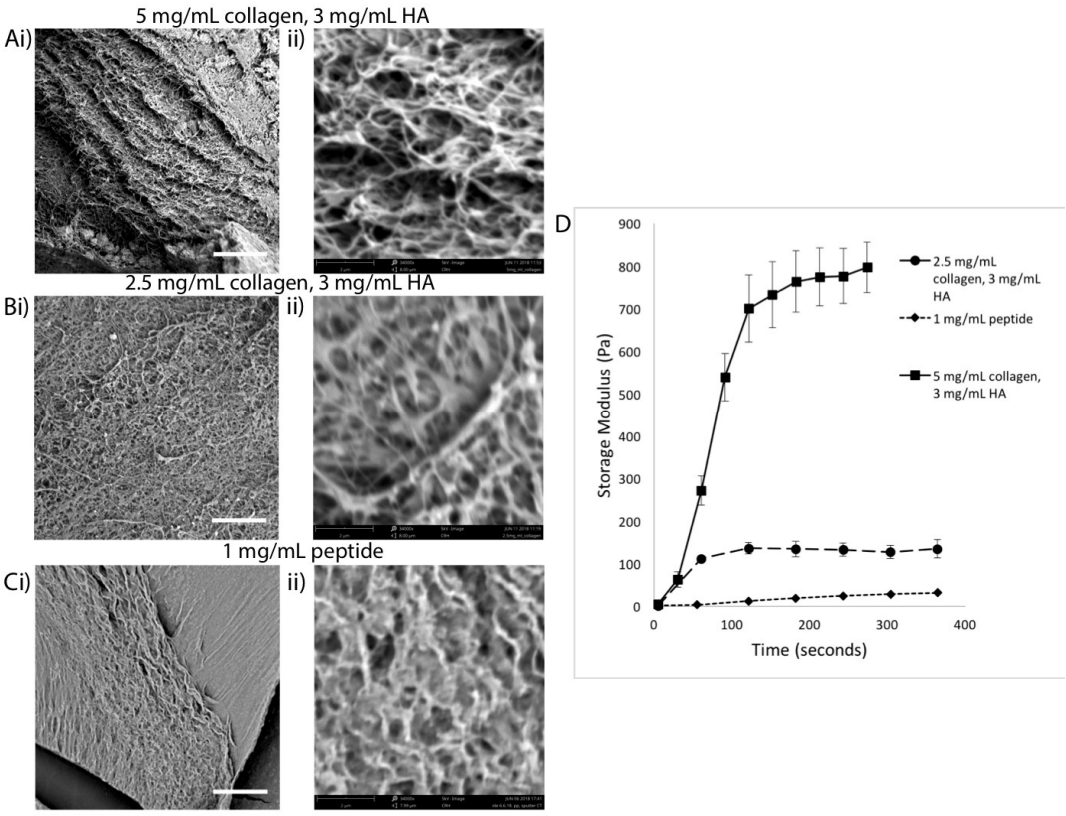

Figure 20. Hydrogel microstructural and rheological analysis. Ai) Low magnification of 5-mg/mL collagen / 3-mg/mL HA hydrogel microstructure. Aii) High magnification image showing hydrogel porosity. Bi) Low magnification of 2.5-mg/mL collagen / 3-mg/mL HA hydrogel microstructure. Bii) High magnification image showing hydrogel porosity. Ci) Low magnification of 1-mg/mL peptide hydrogel microstructure. Cii) High magnification image showing hydrogel porosity. D) Storage moduli for each hydrogel formulation. Scale bars, 10 µm for Ai, Bi, Ci, and 2 µm for Aii, Bii, Cii. Error bars denote standard error of mean. Rheology data sample size is n=3 for 5-mg/mL collagen / 3-mg/mL HA hydrogel, n=3 for 2.5-mg/mL collagen / 3-mg/mL HA hydrogel, and n =1 for the 1 mg/mL peptide.

Three hydrogel formulations used in experiments have been analyzed microstructurally and their stiffness values were determined using a rheometer. The hydrogel microstructure used for in vitro experiments can be seen in Figure 20Ai, with a higher magnification image showing structure detail in Figure 20Aii. This hydrogel exhibited the stiffest storage modulus values of approximately 800 Pascal's compared with the other two conditions. These hydrogel properties were established to prevent

hydrogel collapse during in vitro experiments. The second hydrogel formulation that was used for the hemisection SCI animal model transplantations is shown in Figure 20Bi, Bii. This hydrogel formulation had a final 2.5 mg/mL collagen concentration compared with the final 5 mg/mL collagen formulation used for in vitro experiments. The lower collagen concentration resulted in a less stiff hydrogel with storage modulus values of 135 Pascal's. The softer hydrogel was selected to provide a more permissive environment for host axon infiltration in vivo. The last hydrogel was made of a RADA-16I peptide with a final concentration of 1 mg/mL peptide (Figure 20Ci,Cii). This hydrogel was used for the compression SCI studies and this hydrogel had the lowest storage modulus values of 32 Pascal's compared to the other two conditions that had collagen/HA-based formulations.

4.3.2 In vitro RADA-16I peptide experiments.

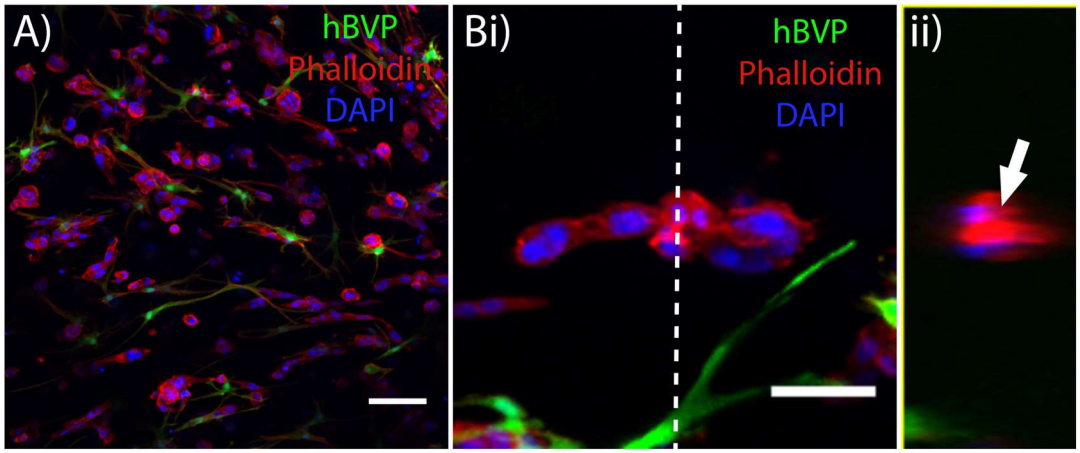

Figure 21. Lack of microvessel formation in 5 mg/mL peptide. A) Day 4 perfused peptide with a 5:1 ratio of hCMEC/d3 and GFP-hBVP coculture. Bi,ii) High magnification of a multicellular structure with a cross section that shows lack of lumen (white arrow). Green: hBVP. Red: Texas-Red Phalloidin. Blue: DAPI. Scale bars, A) 100 um, B) 50 um.

4.3.2.1 Endothelial-only self-assembled vessels. Seeding a 5:1 coculture of hCMEC/D3 and hBVP within a 5 mg/mL peptide failed to yield microvessel formation. Cell-seeded 5 mg/mL peptide gels were injected into the hydrogel reservoir of the same microfluidic device design as for the microvessel formation within the collagen/HA scaffolds (Figure 21). This final peptide concentration was selected to provide scaffold structural integrity for transplantations into a spinal cord injury animal model after a few days culture in vitro. After peptide injection, the microfluidic devices were incubated with 8 mL of EGM supplemented with growth factors at 37ºC for four days prior to fixation. Immunofluorescence with Texas-Red Phalloidin and DAPI showed numerous multicellular structures within the peptide scaffold denoted by the cell actin and cell nuclei staining (Figure 21A). A high magnification of a cross section of this multicellular structure showed a lack of lumen (Figure 21Bii). The lack of lumen formation could be attributable to seeding the cells in a 5 mg/mL peptide concentration.

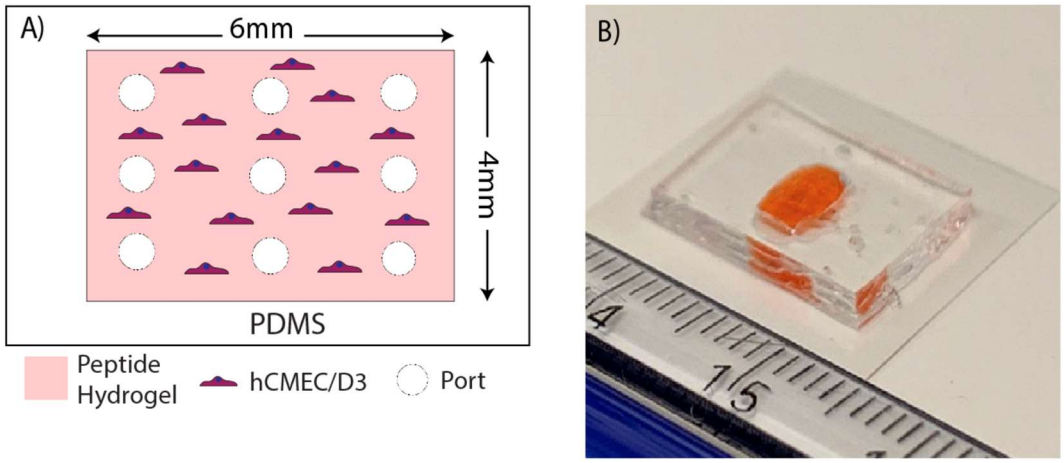

Figure 22. Microfluidic device for 1 mg/mL peptide scaffold. A) Schematic showing the central chamber, cell seeding location, peptide hydrogel, and open ports. B) Photograph of the device with food dye showing central chamber.

Reducing the peptide concentration to 1-mg/mL and supplementing with the growth medium 50 µg/mL and 50 µg/mL PMA was still insufficient to form microvessels. The addition of these factors mirrored a previous study (Sieminski et al., 2007) that demonstrated the formation of microvessels within 1 mg/mL peptide scaffolds using human umbilical vascular endothelial cells (hUVEC). Due to the lower mechanical integrity of the 1-mg/mL peptide scaffold, a microfluidic device was designed with a thin PDMS membrane to separate the hydrogel from the culture medium during gelation (Figure 22A-B).

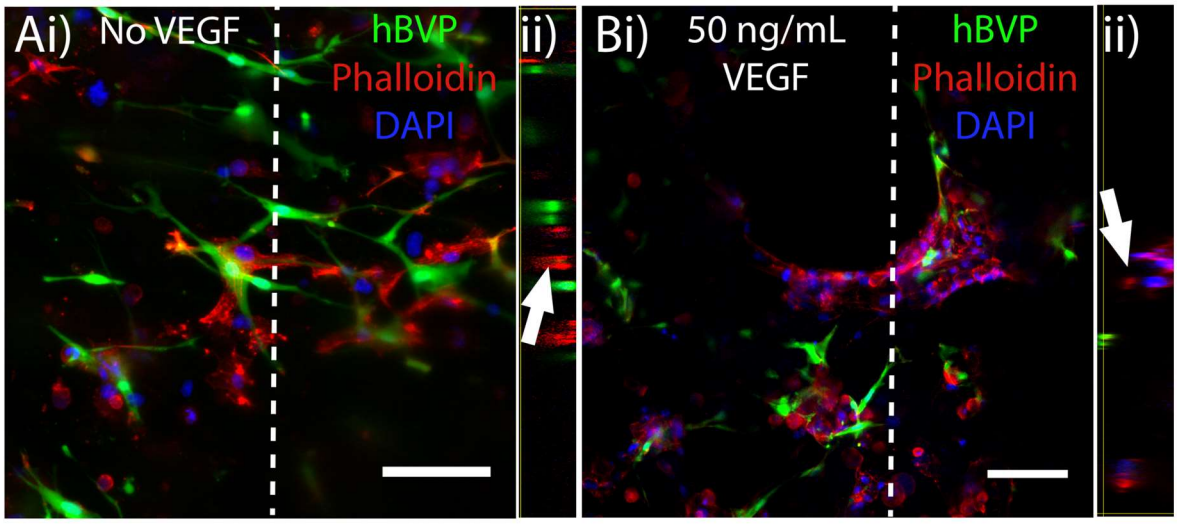

Figure 23. Lack of microvessel formation in 1 mg/mL peptide at day 5 without or with 50 ng/mL VEGF. Ai) 1 mg/mL peptide without VEGF or PMA supplementation. Aii) Cross section of multicellular structure shows lack of lumen (white arrow). Bi) 1 mg/mL peptide with 50 ng/mL VEGF and 50 ng/mL PMA supplementation. Bii) Cross section of multicelular structure shows partial lumen (white arrow). Green: hBVP. Red: Phalloidin. Blue: DAPI. Scale bars are 100 µm.

After five days of culture in 8 mL mEGM, the structure formation resembled the cells in the 5 mg/mL scaffold (Figure 23Ai, Aii). The addition of 50 ng/mL VEGF and 50 ng/mL PMA to the cultured EGM resulted in a multicellular structures with numerous cell nuclei strung together after 5 days (Figure 23Bi). However, despite the strong multicellular appearance, a cross section of this structure revealed a lack of lumen, similar to those formed in the 5 mg/mL peptide-scaffolds (Figure 23Bii). This suggested that the addition of 50 ng/mL VEGF and 50 ng/mL PMA had a strong effect on the formation of multicellular structures within the 1 mg/mL peptide.

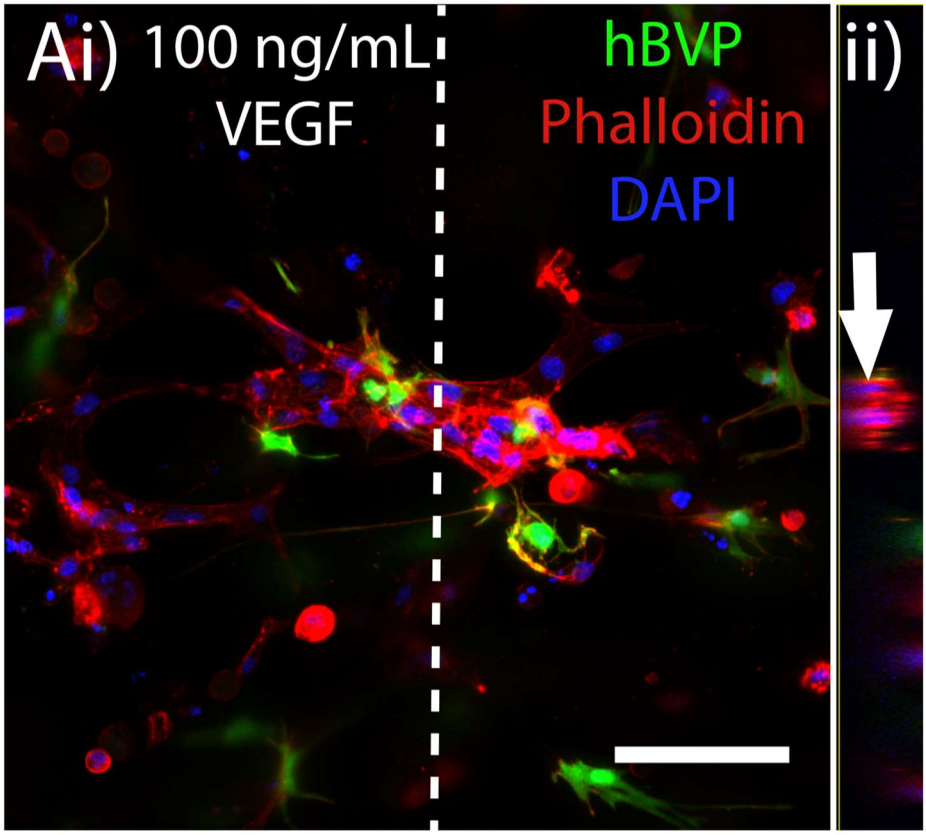

Figure 24. Lack of microvessel formation with 100 ng/mL VEGF for endothelial/pericyte coculture at day 3. Ai) Multicellular structure within 1 mg/mL peptide. Aii) Cross section of the multicellular structure shows complete lack of lumen formation (white arrow). Green: hBVP. Red: Phalloidin. Blue: DAPI. Scale bar is 100 µm.

Since VEGF is responsible for the formation of tube-like structures and PMA simply increases the quantity of tube-like structures, VEGF concentration was to achieve mature microvessel formation. hCMEC/d3 and hBVP were cocultured at a ratio of 5:1 and seeded at a final density of 5 million cells per mL. The cultured 8 mL of mEGM per peptide gel was supplemented with 100 ng/mL VEGF and 50 ng/mL PMA. At day three, the peptide gel was fixed and stained after identification of a multicellular-like structure under the brightfield microscope. Immunofluorescence with Texas-Red Phalloidin and

DAPI showed multicellular structure with cell nuclei strung together surrounded by GFP-labeled hBVP (Figure 24Ai). However, a cross section of this multicellular structure failed to show any potential formation of a microvessel with a lumen center (Figure 24Aii). Due to the lack of microvessel formation within this 1 mg/mL peptide supplemented with 100 ng/mL VEGF, a different model of seeding endothelial cells only was pursued.

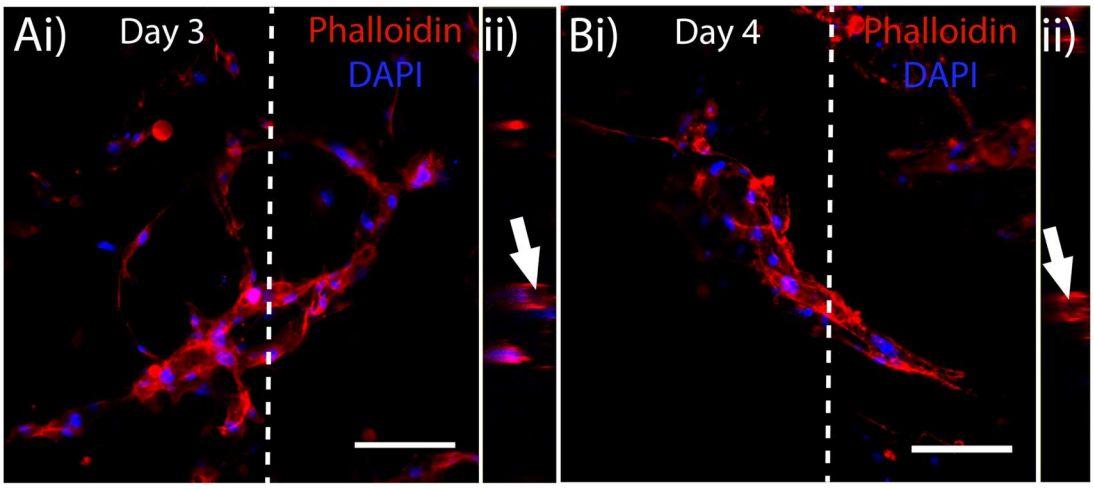

Figure 25. Microvessel formation within 1 mg/mL peptide with 100 ng/mL VEGF and 50 ng/mL PMA supplementation. Ai) Day 3 multicellular network within a 1 mg/mL peptide. Aii) Cross section of the multicellular structure shows almost complete lumen formation (white arrow). Bi,ii) Day 4 multicellular structure within 1 mg/mL peptide shows complete lumen formation (white arrow). Red: Texas Red Phalloidin. Blue: DAPI. Scale bar is 100 µm.

In order to isolate the effect of VEGF and PMA on the endothelial cells, pericytes were not seeded within the 1 mg/mL scaffolds. hCMEC/d3 were seeded at a density of 5 M/mL supplemented with 100 ng/mL VEGF and 50 ng/mL PMA. After three days in culture, a multicellular network could be observed within the 1 mg/mL peptide scaffold (Figure 25Ai). However, a cross section of this multicellular network at this time point

did not show complete lumen formation (Figure 25Aii). However, at day four of culture microvessels (Figure 25Bi) appeared with complete lumen formation (Figure 25Bii). Showing the ability for microvessels to form within the peptide scaffold in vitro is a crucial prerequisite prior to transplantation.

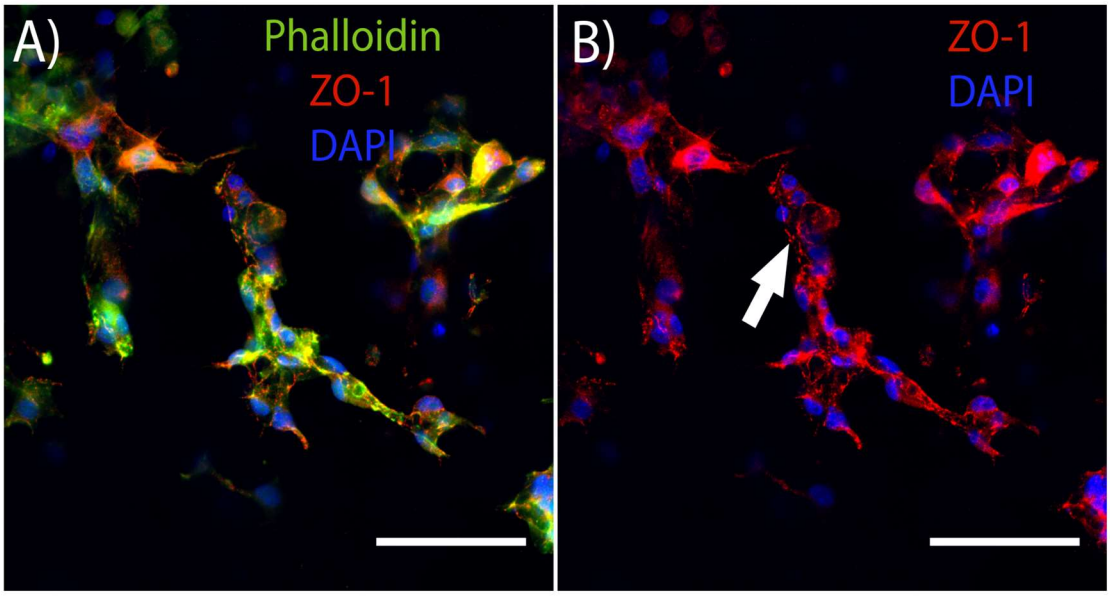

Figure 26. Day 5 barrier evaluation within 1 mg/mL peptide supplemented with 100 ng/mL VEGF and 50 ng/mL PMA. A) Merged image showing cell actin (green phalloidin), punctate tight junction staining (red), and cell nuclei (blue). B) Isolated tight junction staining showing punctate staining (white arrow). Scale bars are 100 µm.

In addition to demonstrating lumen formation, the integrity of the barrier was also assessed. After five days in culture gels were fixed and stained with ZO-1 antibody to determine the presence of tight junction formation within the microvessels. Merged image between phalloidin-FITC, ZO-1, and DAPI revealed microvasculature with a colocalized tight junction staining to the cell membranes (Figure 26A). Merged image

between ZO-1 and DAPI showed clear punctate tight junction staining indicative of a BSCB-integrity formation (Figure 26B). After proving the ability of the microvasculature within the 1 mg/mL peptide to form BSCB-integrity microvessels, we next transplanted these cellular peptides into a spinal cord injury contusion rat animal model to determine the matrix permissivity to host axon infiltration.

4.3.3 In vivo spinal cord injury contusion rat animal model.

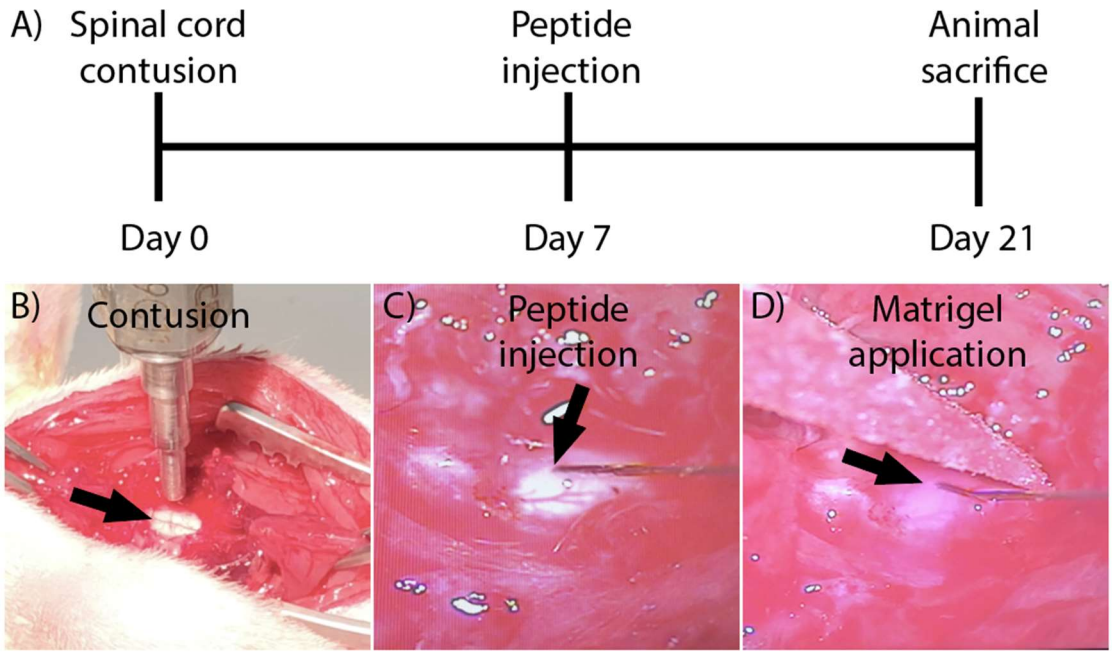

Figure 27. Sprague Dawley rat spinal cord contusion model. A) Experimental timeline with steps. B) Contusion setup showing exposed C4-C5 spinal cord (black arrow). C) Peptide injection setup (black arrow). D) Matrigel application over the injection location to prevent peptide leakage. Matrigel can be seen by transparent pink color (black arrow).

In vivo peptide transplantation experiments were conducted using the spinal cord injury contusion rat animal model. The overview of the experimental timeline with each step is shown in Figure 27A. On day zero, Sprague Dawley rats underwent laminectomy to expose cervical 4 and 5 spinal cord vertebrae where a 150,000 Dyne compression was

applied with 0 second dwell time using the IH Infinity Horizontal Impactor (Lexington, Model 0400). Application of the 150,000 Dyne force is considered a moderate spinal cord injury in which there is a visible behavioral deficit. The experimental setup for the compression is shown in Figure 27B, where the C-4/C-5 spinal cord is exposed with the weight apparatus in place. One week later the animals were injected with a peptide based scaffold that had a ratio of 5:1 hCMEC/d3 to hBVP conditions of the following final cell densities: high cellular density of 5 M/mL, low cellular density of 2.4 M/mL, and acellular conditions. At the time of the contusion at day zero, a medical suture was placed in close proximity to the epicenter of the impact in order to find the appropriate location for the peptide injections. 10 µL peptide injections were administered at a flow rate of 100 nL/s using a Micro-Syringe Pump Controller (Micro4). The peptide injection setup is shown in Figure 27C, where the 30-gauge injection needle is in place. In order to prevent the injected peptide form leaking out, the injection needle was left in place for at least two minutes prior to removal and 20 µL of Matrigel was applied over the peptide injection location (Figure 27D). Two weeks later animals were sacrificed and processed for immunohistochemistry staining.

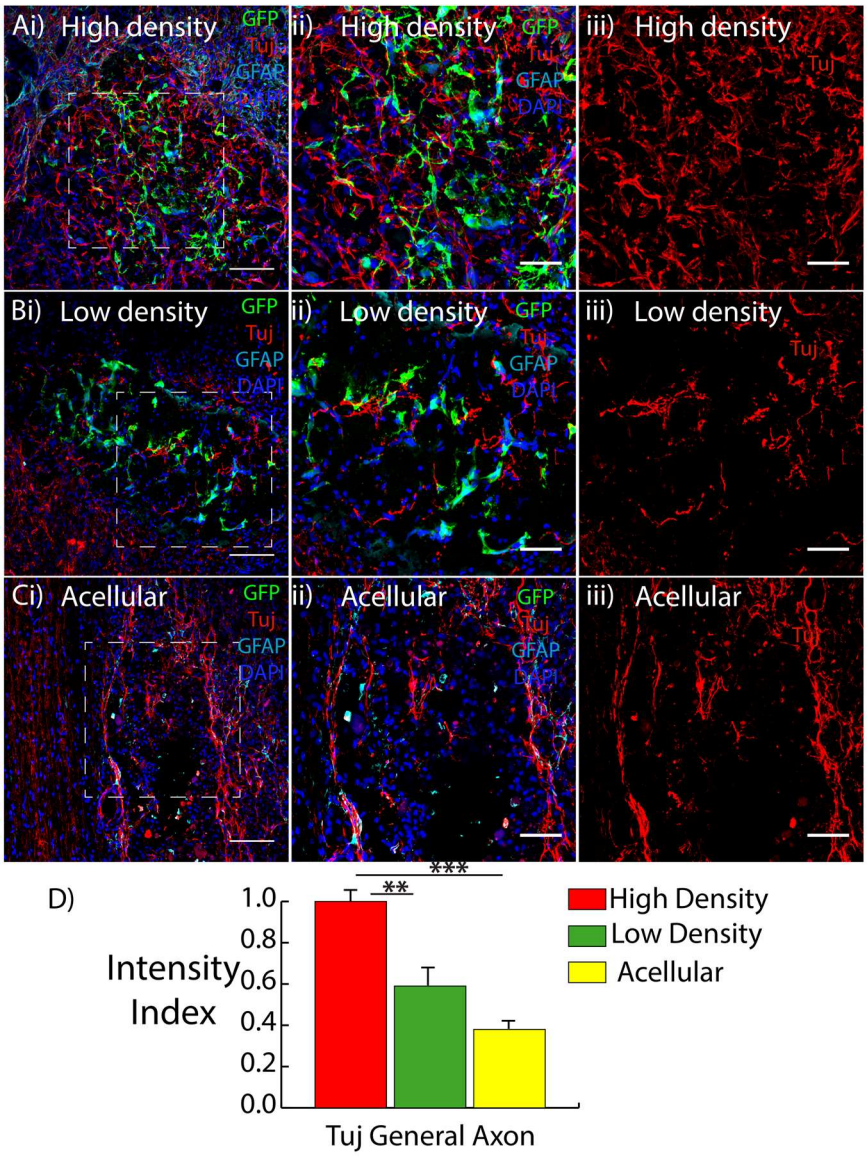

Figure 28. General Tuj axon infiltration within peptide transplants. Ai) High cellular density (5 M/mL) transplant at a low magnification showing transplanted cells (GFP), inflammation (GFAP), host general axons (Tuj), and cell nuclei (DAPI). Aii, iii) Inset showing magnified region from Ai) (white dashed line) and isolated channel showing general axons (Tuj). B) Low cellular density (5 M/mL) transplant showing low magnification (Bi) and magnified regions (Bii, Biii). C) Acellular transplant at low magnification (Ci) and magnified regions (Cii, Ciii). GFP hCMEC/d3 and GFP hBVP (green), Tuj (red), GFAP (cyan), DAPI (blue). Scale bars, 100 µm for Ai, Bi, and Ci, all others are 50 µm. Data are presented as mean + s.e.m. **P<0.01, ***P<0.001; statistical significance was calculated using Welch Two Sample t-test. Intensity values (n=6 per condition) normalized to High Density condition and from 2 IHC sections per condition.

4.3.3.1 Tuj-positive axon infiltration. Tuj expression within the peptide transplants verifies its increased permissivity to host axons. The highest host axon infiltration within the peptide transplants is seen in the high cellular density (5M/mL) condition (Figure 28Ai-Aiii), whereas the low cellular density (2.4 M/mL) condition has fewer infiltrating axons (Figure 28Bi-Biii). Similar to the low cellular density condition, the acellular peptide condition (Figure 28Ci-Ciii) shows fewer infiltrating host axons compared to the high cellular density condition. Correlation of the Tuj channel fluorescence intensity with the number of infiltrating host axons, shows that the high cellular density condition has axon infiltration levels that are significantly higher than the other two conditions (Figure 28D), demonstrating a correlation between endothelial cell density and axon infiltration.

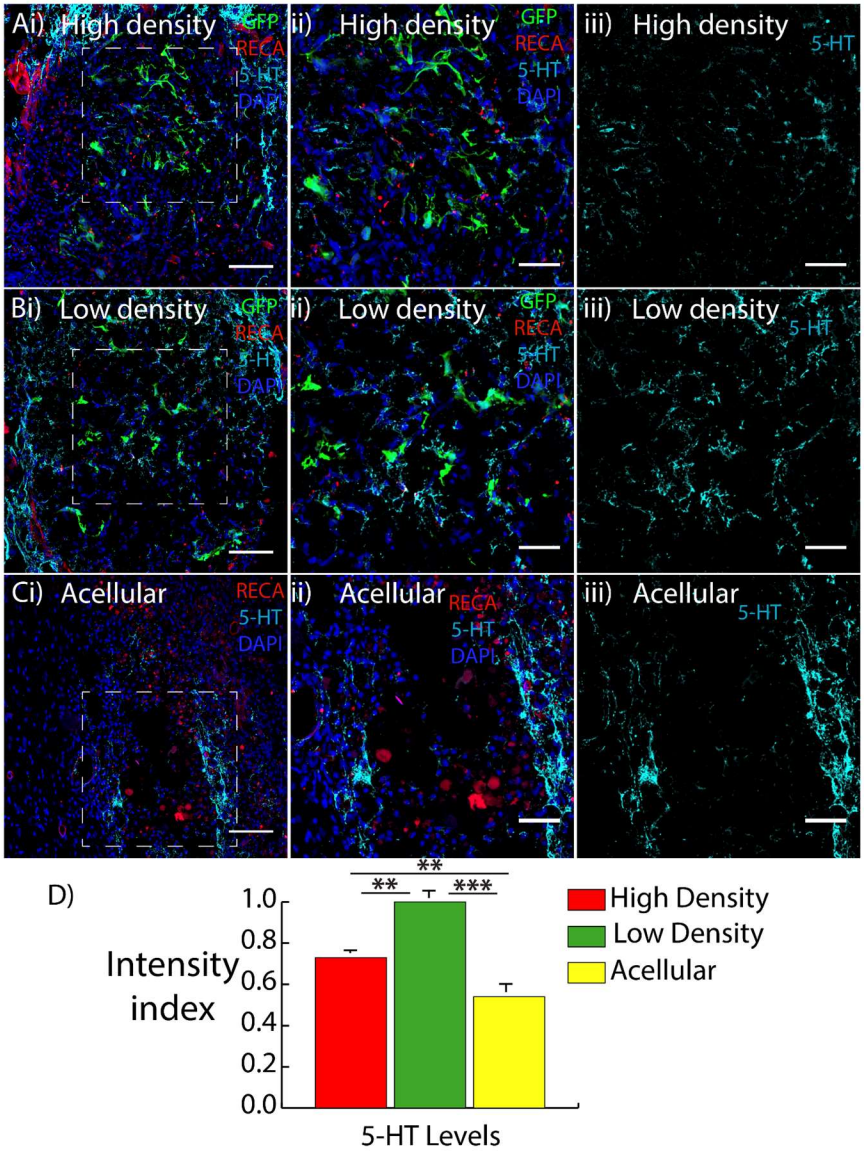

Figure 29. Serotonergic levels within peptide transplants. Ai) High cellular density (5 M/mL) transplant at a low magnification showing transplanted cells (GFP), host blood vessels (RECA), host serotonin (5-HT), and cell nuclei (DAPI). Aii, iii) Inset showing magnified region from Ai) (white dashed line) and isolated channel showing serotonin (5-HT). B) Low cellular density (5 M/mL) transplant showing low magnification (Bi) and magnified regions (Bii, Biii). C) Acellular transplant at low magnification (Ci) and magnified regions (Cii, Ciii). GFP hCMEC/d3 and GFP hBVP (green), RECA (red), 5-HT (cyan), DAPI (blue). Scale bars, 100 µm for Ai, Bi, and Ci, all others are 50 µm. Data are presented as mean + s.e.m. **P<0.01, ***P<0.001; statistical significance was calculated using Welch Two Sample t-test. Intensity values (n=6 per condition) normalized to Low Density condition and from 2 IHC sections per condition.

4.3.3.2 5-HT serotonin infiltration. 5-HT positive infiltration was observed in the low cellular density condition. The presence of 5-HT positive staining suggested the involvement of serotonergic neurons, which have many roles including the generation of locomotion (Ghosh & Pearse, 2014). The high cellular density of 5 million cells per milliliter injection (Figure 29Ai) resulted in significantly higher presence of serotonergic neurons within the scaffolds compared to acellular controls (Figure 29Ci). The low cellular density of 2.4 million cells per milliliter injection (Figure 29Bi) had the highest level of serotonergic neruons compared to the high cellular density (Figure 29Ai) and acellular injection (Figure 29Ci) conditions. Magnified images (Figure 29Aii, Bii, Cii) and isolated 5-HT fluorescence images (Figure 29Aiii, Biii, Ciii) for each condition were used to analyze the results. The intensity of the 5-HT- positive fluorescence was correlated with the amount of serotonergic neuron presence and the fluorescence intensity values were normalized to the low density condition. Quantification of this fluorescence showed statistical difference between each condition, including a difference between the high and low cellular density injections (Figure 29D). Thus, although the high cell density condition resulted in increased serotonergic levels, greater 5-HT positive level was observed in the low cellular density condition.

4.3.3.3 Microvessel formation.

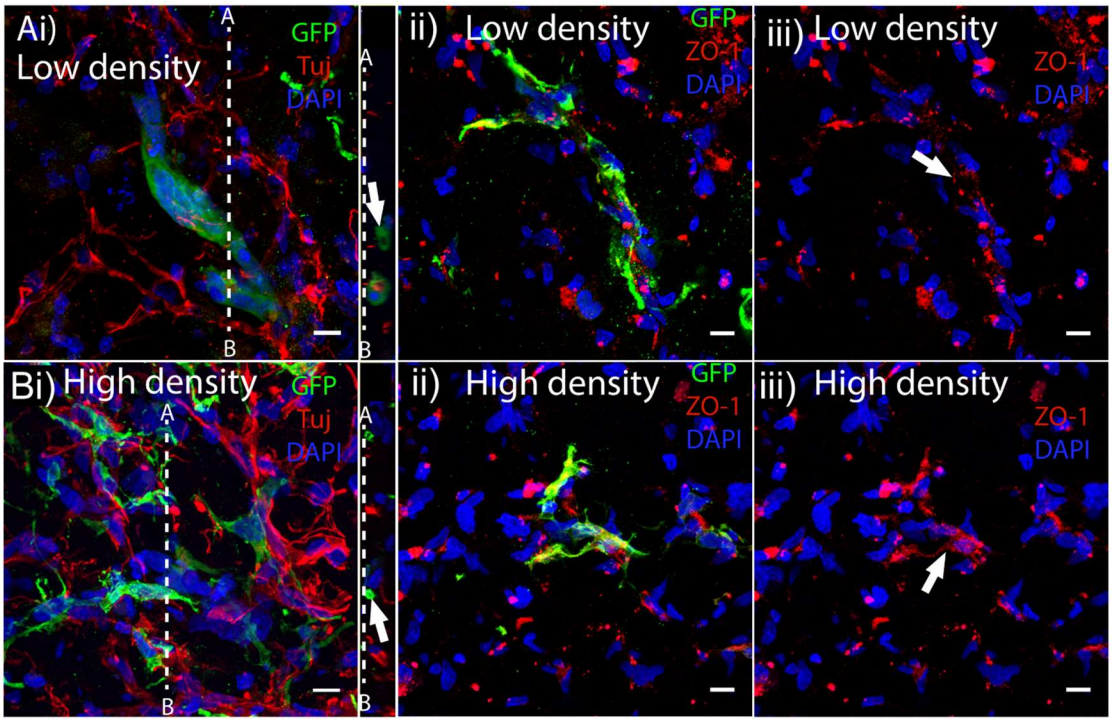

Figure 30. Blood-spinal cord barrier (BSCB)- integrity microvessel formation within transplants after two weeks in vivo. Ai) Low cellular density (2.4 M/mL) condition showing microvessel (GFP), host general axons (Tuj), and cell nuclei (DAPI). Microvessel cross section (dashed lines in Ai) showing a 1.88 µm lumen diameter (white arrow). Aii) Low cellular density transplant showing transplanted cells (GFP), tight junctions (ZO-1), and cell nuclei (DAPI). Aiii) Overlay between tight junctions and cell nuclei. Bi) High cellular density (5 M/mL) condition showing microvessel (GFP), host general axons (Tuj), and cell nuclei (DAPI). Microvessel cross section showing a 0.90 µm lumen diameter (white arrow). Bii) High cellular density transplant showing transplanted cells (GFP), tight junctions (ZO-1), and cell nuclei (DAPI). Biii) Overlay between tight junctions and cell nuclei. Green: hCMEC/d3, hBVP. Red: Tuj. Blue: DAPI. Scale bars are 10 µm.

Transplanted endothelial cells formed microvessels within the injury site by the two-week sacrifice. The low cellular density condition (Figure 30Ai) resulted in more multicellular resembling structures than within the high cellular density condition (Figure 30Bi). However, high magnification imaging showed the presence of 1.88 μm diameter lumens (Figure 30Ai) within the low density cellular condition and 0.90 μm diameter lumens (Figure 30Bi) within the high density cellular condition. Staining with a ZO-1 tight junction protein showed positive punctate cell membrane localization within the low density peptide condition (Figure 30Aii), but not in the high density peptide condition (Figure 30Bii). These results demonstrate the formation of microvessels in both cellular density conditions and microvessel barrier- integrity in the low cell density condition.

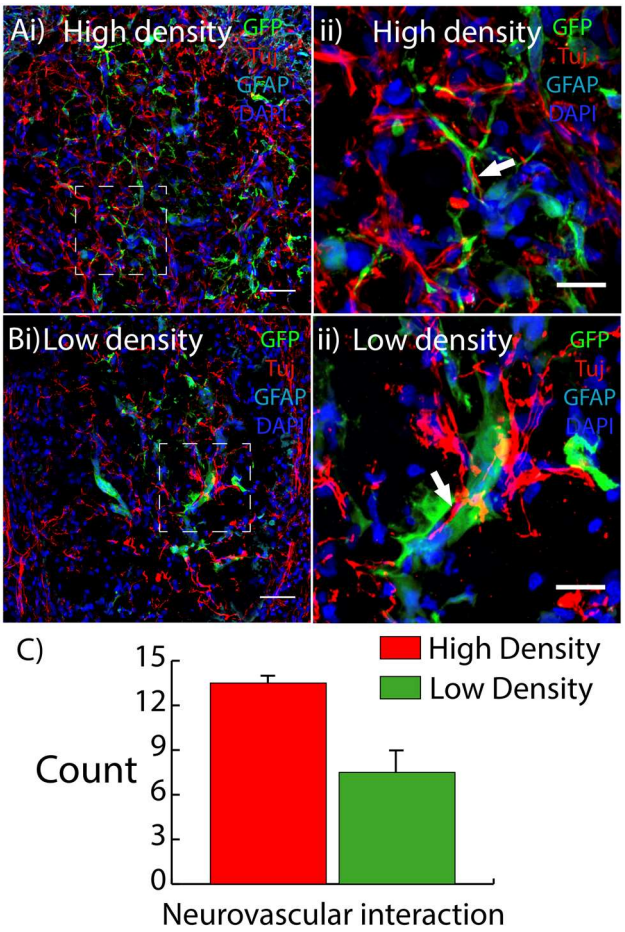

Figure 31. Neurovascular interactions within transplanted scaffolds after two weeks in vivo. Ai) Low magnification of high cellular density (5 M/mL) condition showing host axon interaction (Tuj) with transplanted microvessels (GFP). Aii) High magnification of inset from Ai) showing neurovascular interaction (white arrow). Bi) Low magnification of low cellular density (2.4 M/mL) condition showing host axon interaction (Tuj) with transplanted microvessels (GFP). Bii) High magnification of inset from Bi) showing neurovascular interaction (white arrow). Green: hCMEC/d3, hBVP. Red: Tuj. Cyan: GFAP. Blue: DAPI. Scale bars, 50 µm for Ai and Aii, 20 µm for Aii and Bii.

4.3.3.4 Neurovascular interaction. Transplanted cells formed neurovascular interaction with host axons. Low magnifications of high (Figure 31Ai) and low (Figure 31Bi) cellular density conditions indicated the close proximity between Tuj-positive host axons and GFP-labeled transplanted cells within the entire scaffold. Regions that clearly showed the neurovascular interactions have been magnified (Figure 31Aii, Bii) to show greater detail. Quantification of the number of interactions showed no statistical difference between the high and low cellular conditions (Figure 31C). These results demonstrate that the neurovascular interaction was not dependent on the cellular density within the transplants.

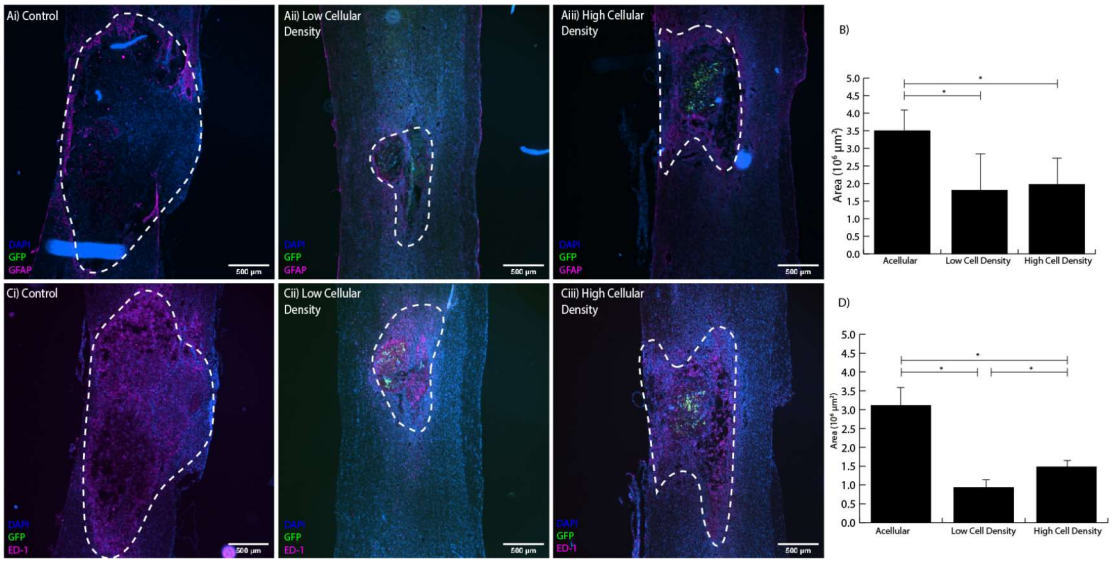

Figure 32. Quantification of glial scar and inflammation following injection of peptide hydrogels. Reactive gliosis in response to peptide hydrogels in (Ai) acellular peptide, (Aii) low cellular density, and (Aiii) high cellular density. DAPI (blue), GFP (green), GFAP (magenta). Quantification of area of gliosis in (B). (C) Inflammatory response to peptide injections, (Ci) acellular peptide, (Cii) low cellular density, and (Ciii) high cellular density. (D) Inflammation area values. Data presented as mean ± s.d. *P < 0.05.

4.3.3.5 Evaluation of inflammation and glial scarring following transplantation.

After demonstrating that the presence of microvessels significantly increased the axon density at the injury site, we interrogated their response on inflammation and scarring. Antibodies for glial fibrillary acidic protein (GFAP) and ED-1 were used to assess these responses. Figure 32A indicates that the GFAP-positive area was significantly reduced in animals receiving cell-seeded peptide injections, though there was no significant difference between the two cell densities (Figure 32B). This result suggests that the size of the glial scar was reduced in response to the cell-seeded scaffold. A similar response was found when using ED-1 to stain for macrophages and microglia (Figure 32C). The area of positive-ED-1 staining in the acellular condition was present throughout the site of injury. Quantification of the positive-ED-1 area indicated a significant reduction in both cell-seeded scaffolds, though again there was no significant difference between the two cell densities. Taken together, these results suggest that the addition of BSCB-integrity microvessels attenuates inflammation and scarring, but the effect is not dependent on the density of transplanted cells.

4.4 Summary of Results

The research presented here evaluated the central hypothesis that aligned blood vessels promote and guide axon growth within permissive scaffolds. The construction of an in vitro 3D blood-brain barrier (3D) showed that mechanical stress regulated the integrity of the barrier. The formation of barrier-containing microvessels created the ability to transplant vascularized scaffolds into a rat hemisection model of spinal cord injury. Finally, the efficacy of a self-assembling peptide hydrogel to increase the permissivity of these scaffolds was assessed.

The objective of the first specific aim was to pattern a vessel within a microfluidic device that contained barrier-integrity vasculature. Pulling an acupuncture needle from a collagen-hyaluronan hydrogel created a 180-µm void that could be seeded with endothelial cells. The application of luminal flow applied shear stress on the endothelial lumen that caused endothelial cells to form tight junctions. Immunocytochemistry and imaging analysis via a transmission electron microscope was sued to visualize protein localization and microstructure of the junctions. However, an initial pilot transplantation study in a Sprague Dawley spinal hemisection injury model indicated that the endothelial cells within the 180-µm-diameter vessels did not remain viable. Interestingly, host axons and blood vessels infiltrated the luminal side of the vessels, even though the endothelial cells were not viable. Overall, these initial experiments provided insight into the formation of barrier function in vitro, but indicated that an alternative approach was needed for in vivo experiments moving forward.

Given the disparity in size between the transplanted 180-µm-diameter vessels and the host microvasculature, experiments were conducted to create microvasculature that still featured tight junctions, but with diameters of approximately 30-µm or less. To accomplish this goal, a co-culture of endothelial cells and pericytes formed microvessels spontaneously within five days of seeding into a collagen-hyaluronan composite scaffold. In order to align these microvessels prior to transplantation experiments, interstitial fluid flow was applied using a custom-designed microfluidic device. The low shear stress exerted on the microvasculature was enough to stimulate alignment with the direction of fluid flow. In order to verify barrier integrity of the vessels, tight junctions were visualized using immunocytochemistry and dextran exclusion permeability assays. This

approach provided a means to transplant aligned vasculature that had similar dimensions to host vasculature.

The objective of the second specific aim was to explore intrinsic neurovascular interaction between axons and microvessels to guide axon growth. Prior to transplantation, initial experiments were performed to determine whether axons from neural progenitor cells (NPC) would align with the microvessels in vitro. The interstitial fluid used for perfusion of the hydrogels to initiate microvessel alignment was supplemented with NT-3 in order to induce the NPCs to differentiate into neuronal cells instead of glial cells. After five days of interstitial fluid perfusion supplemented with NT-3, Tuj- positive axons were localized along the length of aligned microvessels. In order to determine whether the Tuj-positive axon alignment was a result of the neurovascular interaction with the microvessels or a flow-induced effect, the cd44 receptor on endothelial cells was knocked down using siRNA. Since cd44 was needed for microvessel alignment, reducing the expression of this receptor resulted in microvessels uncoupled from the direction of fluid flow. Using this this method, the Tuj-axon alignment was determined to be the result of the neurovascular interaction and not a flow mediated effect.

After verifying neurovascular interaction in vitro, scaffolds with and without aligned microvessels were transplanted into an animal hemisection injury model. In contrast to the 180-μm-diameter vessels, the microvessels remained viable after three-weeks in vivo. In validation of the NPC in vitro experiments, the host axons infiltrated the vascularized scaffold in an orientation dictated by the transplanted microvessels. The axons that infiltrated the scaffolds were general Tuj-positive axons as well as CGRP-

positive regenerating axons, a marker for sensory tract axons. However, despite the ability to control axon direction within the scaffolds, the number of infiltrating axons was low and warranted a method to increase the permissivity of the scaffold in order to facilitate functional recovery.

The third and final specific aim focused on increasing host axon permissivity within the transplanted scaffolds using a nanofiber self-assembling RADA-16I peptide. Initial experiments verified the formation of barrier integrity vasculature within the peptide hydrogel in vitro using the endothelial cell method. A novel microfluidic device was developed to account for the pH-sensitive polymerization of the RADA-16I peptide. Barrier integrity was again verified using immunocytochemistry, which showed the presence of localized tight junctions at the cell-cell junctions. Additionally, dextran exclusion permeability assays demonstrated that the permeability of the vasculature was comparable to published values for permeability of vasculature in the central nervous system. After verifying barrier integrity in vitro, cell-seeded peptide scaffolds were injected into a Sprague Dawley model of compression-induced spinal cord contusion. A contusion injury model was chosen since the peptide was injectable, and thus more relevant for clinical applications. At three weeks post-transplantation, there was significantly higher infiltration of both general Tuj-positive axons and serotonergic 5-HT-positive axons in comparison to acellular controls. In addition, the transplanted cells formed microvessels that exhibited CNS-barrier integrity, as verified by immunohistochemistry for a tight junction marker. These findings demonstrated that the RADA-16I scaffold could increase the permissivity of the vascularized scaffold, further advancing the field to a bioengineered approach to repairing spinal cord injury.

Chapter V

Discussion

5.1 Application of Mechanical Stress to the 3D Model of the 180-µm Blood-Brain Barrier

The initial 180-µm-diameter pre-patterned vascular structure establishes the ability to form barrier function in vitro. In addition to being the first demonstration of a 3D, deformable model of barrier function, the model also can assess the effect of mechanics on barrier function. Previous models of the CNS vasculature are limited to studying the effect of shear stress applied to the endothelium by blood flow, whether in 2D models or 3D models that rely on undeformable, synthetic meshes or lack perfusion. Yet there is substantial evidence suggesting that the pulsatile radial strain exerted by blood flow on the arterial tree is crucial for normal cardiovascular physiology (X. Guo & Kassab, 2004). The 3D barrier model decouples shear stress from cyclic stretch in order to elucidate the effect of these mechanical stimuli on CNS structure and function. The findings suggest that both stress and stretch are important regulators of barrier function. In fact, the permeability studies indicate that mechanical stimulation is even more crucial for barrier formation than interaction with astrocyte endfeet, which raises the question of how critical astrocyte endfeet interaction with the endothelium is for CNS function. Certainly, there are larger cerebral arterioles with a substantial muscular media layer separating astrocyte endfeet from the endothelium that exhibit functioning CNS. Additionally, the lack of pericytes in the model also suggests that pericyte interaction with the endothelium may not be required to facilitate a secure barrier for this 180-µm diameter vascular model.

The 180-μm vascular model has a benefit in identifying wall strain as a regulator of barrier function, which has clear implications for the pathogenesis of neurological diseases. The primary risk factor associated with Alzheimer's and other dementias is increasing age, which is characterized by stiffening of the vascular wall. In fact, results from immunohistochemical studies suggest that small and medium-sized arterioles are the primary source of leaked plasma components that enter into the brain tissue as a result of CNS compromise, which has been causally linked to diseases such as Alzheimer's disease and in delirium and post-operative cognitive decline in the elderly (Acharya et al., 2015; Clifford et al., 2008). Vascular wall strain is presumably decreased as the wall stiffens, which may provide a mechanically-induced mechanism contributing to CNS breakdown. The stress generated in the wall should be directly correlated to the pressure within the vessel, so the strain is dependent upon the compliance of the wall. This could also explain why arterioles and not venules exhibit perivascular “leak clouds” reflecting the influx of plasma components into the brain parenchyma in Alzheimer's disease (Clifford et al., 2008). The molecular basis for stretch-induced barrier homeostasis provides an additional area of further research. Force-mediated cadherin membrane localization has been associated in endothelial cells with a Rho/ROCK- mediated pathway (Liu et al., 2010), which provides a starting point for investigating the cerebral vasculature.

5.2 Neurovascular Interaction to Guide Axon Growth

Due to the inability of scaffolds containing 180-μm diameter vessels to remain viable following transplantation, an alternative approach was used to fabricate microvessels on the same scale as the host vasculature of a rat spinal cord. Previous

studies have shown pericytes or vascular endothelial growth factors (VEGF) must be added to facilitate spontaneous assembly of vacular structures. Endothelial cells alone, without growth factors, do not self-assemble to form vessels, but adding pericytes causes microvascular formation. Pericytes help the endothelial cells mature and form vessels through direct physical contact and paracrine signaling (Bergers & Song, 2005). Similarly, VEGF directly stimulates endothelial cell filopodias to extend their tips and initiate vasculogenesis (Gerhardt et al., 2003). Due to the cytoprotective effects of pericytes as well as release kinetics of VEGF, pericytes are used to create barrier integrity microvessels for these experiments.

The microvessels are aligned by flow-induced shear stress applied to the cell-seeded scaffolds prior to transplantation. The application of interstitial fluid flow through hydrogels exerts a shear stress on the microvessels that activates mechanosensing complexes within the cells. Our experiments show that cd44 is involved in this mechanotransduction, since knock-down experiments with siRNA inhibited flow-induced microvessel alignment. Interestingly, the addition of blebbistatin, which inhibits myosin II, also inhibits microvessel alignment, indicating that Rho/ROCK signaling is also involved in the response of these vessels to shear stress. Overall, the ability to disrupt alignment while applying interstitial fluid flow is critical in determining whether axon alignment is caused by the direction of fluid flow or the orientation of the microvessels.

Exploiting the intrinsic interaction between neural and vascular cells holds great potential for directing axon growth in regenerative applications designed for repair and restoring connectivity in the CNS. We used interstitial fluid flow to align microvessels exhibiting BSCB-integrity within transplantable scaffolds, and then investigated the

ability of these vessels to dictate axon orientation. Our results demonstrate that microvessels guide axon growth from both neural progenitors in vitro and infiltrating neurites in vivo. A proof-of-concept transplantation study in a hemisection spinal cord injury model corroborated the in vitro results by demonstrating that axons infiltrating the scaffold aligned with the patterned microvasculature. Determining that aligned microvessels guide the direction of axon growth has important implications for regenerative approaches in the CNS, specifically in the spinal cord where the ascending and descending neural tracts align primarily along the rostral-caudal axis and the challenge is not only to promote regeneration, but also to provide directional cues.

We observed that seeding a co-culture of vascular pericytes and cerebral microvascular endothelial cells within a collagen and hyaluronan composite scaffold spontaneously formed microvessels featuring barrier properties. After several days in culture, the microvessels exhibited tight junctions and low permeability values characteristic of the CNS-vasculature. The barrier formed in microvessels exposed to both perfused and static conditions. This result appears to contradict our previous finding in the 180-μm-diameter vascular model that tight junction formation requires application of 0.7 dyn/cm^2 of fluid shear stress to the lumen (Partyka et al., 2017). However, the mode and magnitude of shear stress applied to endothelial cells by bulk perfusion differ from that exerted by luminal flow, and likely changes as the cells form microvessels. Moreover, the geometry of our previous model features a diameter of 180-μm, which is an order of magnitude greater than the ~10 μm-diameter microvessel model. Thus, the disparity regarding the role of fluid shear stress suggests that vessel diameter affects barrier function. A recent study implicating the radius of curvature of a substrate as an

important regulator of cell signaling and morphology (Bade, Kamien, Assoian, & Stebe, 2017) lends credence to vessel diameter regulating barrier formation.

Although CNS-vessel integrity is required for functional incorporation into the host vascular bed, our results do not interrogate whether barrier function is required to guide axon growth. A previous study focused on the peripheral nervous system suggests that barrier formation is not required for axonal guidance: non-CNS endothelial cells stimulated and directed the growth of axons from a dorsal root ganglion through VEGF-mediated paracrine signaling (Grasman & Kaplan, 2017). VEGF is a growth factor associated with the growth of both the vascular and neural systems in the central nervous system (Lazarovici, Marcinkiewicz, & Lelkes, 2006), and may contribute to the mechanism underlying the vascular-guided axon growth observed here regardless of the barrier integrity of the microvessels. However, inspection of the immunocytochemistry data indicates close proximity between axons and microvessels, which suggests a juxtacrine signaling mechanism. The basal lamina, a crucial component of the neurovascular unit (del Zoppo, 2010), may contribute to this mechanism. Given that previous studies have found collagen IV and laminin, major components of the endothelial basal lamina, induce and guide axon growth (Yu, Dillon, & Bellamkonda, 1999; Zhu et al., 2018), secretion of these proteins by the cerebral endothelial cells may mediate neurovascular interaction.

Our results demonstrate that patterned vasculature induces axon infiltration from the host and guides their growth, indicating the potential of this scaffold to support axon connectivity and ultimately functional benefits in the damaged spinal cord. SCI creates a complex and inflammatory microenvironment that inhibits axon growth and impedes

spontaneous regeneration (Silver & Miller, 2004). The injury environment, which lacks proper blood supply, also presents a challenge to the viability of cells transplanted into the injury site in regenerative applications (Hill et al., 2007). Previous studies indicate that transplanting conduits with proangiogenic factors (Bakshi et al., 2004; Saglam et al., 2013; Zeng et al., 2011) improves neuroregeneration, suggesting the benefit of delivering oxygen and nutrients through vascularization. Furthermore, an imaging analysis of vascular and axonal networks in the injured spinal cord found that axon growth rate was substantially increased in close proximity to vasculature (C. Dray, G. Rougon, & F. Debarbieux, 2009). Therefore, aligned microvessels have the dual benefit of providing the basis for a vascular bed within the scaffold to promote cell survival and directing the growth of regenerating axons.

5.3 Vascularized RADA 16-I Peptide Scaffold Increases Host Axon Infiltration

Despite demonstrating that neurovascular interaction could be exploited for regenerative approaches, the collagen-hyaluronan scaffolds did not achieve a sufficient amount of axon infiltration for functional recovery. One of the greatest challenges facing scaffolds for spinal cord regeneration is the insufficient number of axon infiltration (Krych et al., 2009). In order to increase the permissivity of the scaffolds, the hydrogel material was changed to a synthetic RADA 16-I nanofiber peptide. This peptide has been previously demonstrated high permissivity and strong tissue-scaffold integration in vivo (J. Guo et al., 2007). In our own experiments, using this new matrix platform, we find that the peptide both supports the growth and maturity of vasculature and infiltration of increased axon density. Although previous studies have shown axon infiltration using both acellular and cellular scaffolds (J. Guo et al., 2007; Stokols & Tuszynski, 2006),

outgrowth of axons from a transplanted scaffold and consequent synaptogenesis have yet to be observed. Vascularizing RADA-16I is a promising approach to achieve this goal.

Our results suggest that the formation of BSCB-integrity microvessels within a self-assembling RADA-16I hydrogel increases axon density and reduces inflammation and scarring at the site of a contusion SCI. Although it's unclear whether the axons present were spared from the initial injury or infiltrating the damaged area, the presence of the microvessels had a positive effect by either supporting the viability of the spared axons or encouraging the growth of regenerating axons. Given that previous studies have demonstrated the ability of transplanted microvessels to anastomose with host vasculature, it is possible that the microvessels benefit the injury site through the delivery of oxygen and nutrients. Recent studies have also showed that vascular cells secrete neuroprotective factors (Nakahashi et al., 2000), which is another possible mechanism by which the transplanted microvessels can augment axon density. Regardless of the underlying mechanism, the results of this study establish the benefit of transplanting microvessels within a RADA-16I peptide hydrogel.

Previous studies have demonstrated the effectiveness of RADA-16I scaffolds to incorporate with the damaged CNS and be permissive to axon growth. Interestingly, we found that the RADA-16I hydrogel exhibits mechanical properties that substantially differ from both physiological CNS tissue and glial scars. Rheometry indicated a lower storage modulus than previous measurements of both spinal cord tissue and glial scars (Moeendarbary et al., 2017). Furthermore, with a loss angle of only 2 degrees, the hydrogel is mostly elastic, which is in stark contrast to the viscoelastic properties of CNS tissue (Ramo, Troyer, & Puttlitz, 2018). Nonetheless, the mechanical properties are

sufficient to support the formation of microvessels and the growth of adjacent host axons. And our results show that these microvessels significantly increase the effectiveness of the scaffold to promote axon growth and reduce glial scarring and inflammation.

A caveat of the approach described in this study is the lack of alignment of the microvessels within the scaffold. Because the microvessels form in the scaffold after transplantation, they cannot be pre-patterned. The reduced storage modulus of the peptide hydrogel precludes the ability to polymerize the scaffold prior to transplantation, necessitating the injection technique described here. The ability to align the microvessels can guide the growth of axons at the injury site, as observed during both spinal cord wound healing (Cyril Dray et al., 2009) and in previous vascularized collagen-hyaluronan composite scaffolds (Partyka et al., 2019). Exerting control over axonal orientation, specifically in the rostral-caudal direction, is a substantial benefit of vascularized scaffolds. Therefore, future studies to control the orientation of transplanted endothelial cells and the microvessels they form following transplantation are crucial. Patterning vasculature within a permissive peptide scaffold like RADA-16I holds great promise for realizing functional improvements following SCI.

Nonetheless, the results of this study establish vascularization as a potential means to improve scaffolds for SCI repair. Our findings indicate that the presence of the microvessels addresses the secondary aspect of SCI, since both GFAP and ED-1 staining, markers for activated astrocytes and macrophage/microglia respectively, were reduced in response to cell-seeded scaffolds. A previous study reports that an upregulation of cytokine growth factors such as IL-6 that is seen during inflammation leads to a diminished axon growth (Lacroix, Chang, Rose-John, & Tuszynski, 2002). Attenuating

the effects of secondary injury and in turn decreasing the size of the glial scar has the potential to facilitate neuroregeneration, and several other approaches including using chondroitinase ABC (Bradbury & Carter, 2011) and other enzymes to degrade the scar have the same goal. However, the approach of delivering a vascularized scaffold can address scar formation while concurrently delivering nutrients and oxygen to regenerating axons. Yet, although this data indicates that the vascularized scaffold increases axon density and reduces inflammation and scarring, future work is needed to quantify the behavioral response of injured animals and fully validate this strategy.

5.4 Conclusions, Impact, and Future Directions

The specific aims of this dissertation have led to the following conclusions:

I. Pre-patterned vessels exhibit barrier-integrity within a microfluidic device in vitro.

II. Neurovascular interaction can be used to guide axon growth in the injured spinal cord.

III. Rada-16I peptide can be vascularized with barrier integrity microvessels to increase host axon infiltration and to attenuate inflammation and scarring.

The implications of this study are that vascularized scaffolds hold great promise for the treatment of spinal cord injury. These studies demonstrate that transplanting microvessels have the potential to address both primary and secondary aspects of spinal cord injury. The results indicate that patterned barrier-integrity microvessels are able to control host axon infiltration in the rostral-caudal direction of the spinal cord and provide the required nutrients for sustained axon proliferation with a reduced inflammatory effect. Additionally, using the self-assembling peptide hydrogel augments the number of

infiltrating axons and reduces both the inflammation and glial scarring. Taken together, this work advances the field of tissue engineering and regenerative medicine by using neurovascular interaction within vascularized scaffolds for the first time to repair the damaged spinal cord.

Though this work does much to advance the field of tissue engineering and regenerative therapies, the results identify several unaddressed questions.

I. To what extent do the vascularized RADA-16I peptide hydrogels facilitate an observable functional recovery in the injured animals?
II. What is the ideal mechanical property of a spinal cord transplant, considering that the most axon infiltration occurred in the scaffold with the lowest storage modulus, yet most elastic properties?
III. Can microvessels be aligned within the peptide-based scaffold post-transplantation using an artificially induced biochemical gradient, exercise-induced mechanical stimulation, or externally applied magnetic fields?
IV. Can the incorporation of microvessels within a scaffold patterned with cylindrical voids achieve axon infiltration and outgrowth following spinal cord injury?

The first question is the most straightforward to address in future experiments. Behavioral analysis can be conducted using the Basso, Beattie, and Bresnahan (BBB) scale, which is designed specifically for rat evaluation after SCI (Basso, Beattie, & Bresnahan, 1995). Since both the hemisection (Wang, Huang, He, & Li, 2014) and contusion (Jin et al., 2011) spinal cord injury models result in low BBB scores two to three days after injury, this injury paradigm is adequate for this study. The results

obtained would determine the extent to which the model needs to be improved. For example, if the BBB scores would be low then the focus should be on aligning the microvessels within the scaffold to guide axons across and out of the scaffold. After functional recovery would be validated using the BBB scores, identifying the type of axons regenerating into the scaffolds would predict the degree of recovery possible. For example, once functional motor recovery is present, corticospinal tract neurons within the scaffold have to be present as well. However, the presence of sensory neurons from the spinothalamic or the dorsal column medial lemniscus tracts, would suggest that there would be pain and temperature recovery as well as fine touch, vibration, and proprioception recovery, respectively.

The results of this dissertation yield a good deal of insight into the question related to mechanical properties of the scaffold (II). It's clear that the biochemical properties of the scaffold and ligand presentation affect axon growth cones, but the mechanical properties of the scaffold are likely large determinants of axon infiltration. AFM studies indicate that in contrast to fibrotic scarring in tissues outside the central nervous system, the glial scar exhibits a lower stiffness than surrounding tissue in the spinal cord (Moeendarbary et al., 2017). The peptide scaffold has a substantially reduced storage modulus than the collagen-hyaluronan composite scaffold as well as a significantly lower loss angle. Additionally, reducing the concentration of the collagen-hyaluronan scaffold also yielded increased infiltration. Yet, given that each of these changes affects ligand presentation to the cells, this study cannot conclusively conclude whether a reduced storage modulus is beneficial for axon growth. Future studies using

scaffolds that can selectively tune the mechanical properties independent of ligand presentation are required to address this question.

A substantial caveat of the RADA-16I is the inability to align the microvessels due to its injectable nature, which is the basis for future directions III. One potential method to align microvessels within the injectable peptide scaffold could be by creating a VEGF gradient in the rostral-caudal direction of the spinal cord. Cellular alignment using a VEGF-gradient has been shown in previous in vitro studies (Nguyen et al., 2013; Shin et al., 2011), but it has not been applied in vivo as a way to regenerate an injured spinal cord. Being able to align microvasculature in vivo within the peptide scaffold could augment functional recovery by increasing the growth of axons through and out of the scaffold.

Finally, the initial transplantation with the 180-µm diameter vessel indicated that axons preferred aligned channels within the scaffold to infiltrate, thus identifying an alternative approach to illicit axon infiltration. Future studies could combine the benefits of vascularizing scaffolds with established approaches to fabricate channels aligned in the rostral-caudal direction. One approach to achieve this method involves 3D printing scaffolds. The benefit of 3D printing technology is the remarkable precision at which scaffolds can be created with channels that could dictate axon direction(Grigoryan et al., 2019) . A published study demonstrates the ability to 3D print scaffolds with channels and loaded cells that cause axon infiltration, synapse relay with the transplanted cells, and ultimate functional recovery following SCI (Koffler et al., 2019). Since nascent vasculature tends to be “leaky” initially, the 3D printed scaffolds should be seeded with a co-culture model of endothelial cells and pericytes for a few days in vitro prior to

transplantation. This combination of 3D printed scaffolds and CNS-barrier integrity vasculature could increase the speed at which functional recovery is occurring.

In the future, moving away from benchtop research to clinical trials, the origin of the cells used for these vascularized transplants must be modified, since using immortalized cell lines is incompatible with viable treatment strategies. Autologous cells can be obtained using autologous drafts in which stem cells are derived from the host or through induced pluripotency. Given that our findings show promise in both acute (hemisection) and chronic (contusion) injuries, this strategy is compatible with patient-derived cells. Using autologous drafts, host stem cells would be drawn from bone marrow or blood and then purified and induced into brain pericytes and brain endothelial cells.

Chapter VI

Detailed Protocols

6.1 Wafer Development Using Soft Lithography

Materials needed

3-inch Silicon wafer (VWR- 102095-792)
SU-8 2025 Photoresist (MicroChem)
Developer solution (Propylene glycol methyl ether acetate- PGMEA (MicroChem)
Aluminum foil
10 mL plastic syringe
180 µm acupuncture needles (DBC)
5”-diameter circular glass beaker (open top)
Trichloro silane (Sigma, 78560-45-9)

Equipment needed

UV Photolithography machine
Rocker
Hot plate
Heating oven
Desiccator

Procedure

1. Place a clean silicon wafer on hot plate preheated to 60ºC for 5 minutes.
2. Using a 10 mL plastic syringe pour 7 mL SU-8 photoresist on the wafer without spilling over the edge.
3. Move any air bubbles to the center of the wafer using the tip of the 10 mL plastic syringe.
4. Use aluminum foil to create a cover to place over the wafer so that it’s protected from daylight.
5. Increase temperature on the hot plate to 95ºC and bake overnight.
6. Lower the temperature to 60ºC and remove any air bubbles by popping them using a 180 µm diameter acupuncture needle
7. Increase the temperature back to 95ºC and leave for 10 minutes until the surface looks homogenous after removing any air bubbles.
8. Turn off the hot plate and allow the wafer to cool for 15 minutes.
9. Transfer the wafer to the UV photolithography machine and place a printed photo mask with the desired design to be fabricated. Use clear scotch tape at the edge of the photo mask to secure it in place.
10. Turn on the UV photolithography machine and apply 200 Watt UV light for 2 hours.

11. Remove the photo mask from the wafer and submerge the wafer in a 5" diameter circular glass container with an open top that has 10 mL of developer solution for 15 minutes.
12. Remove the developer solution and replace with 15 mL new developer solution for another 15 minutes. Perform this step until all of the uncured SU-8 photoresist has been removed.
13. Place the developed wafer in a desiccator that has a few drops of silane for overnight.
14. Remove wafer from the desiccator and proceed to create PDMS stamps.

6.2 PDMS Stamp Fabrication

Materials needed

Poly-dimethylsiloxane (PDMS) (Corning)
Curing agent (Corning)
Plastic cup
Transfer pipette
P100 plastic dish
Developed wafer (described in "wafer development using soft lithography" section)
Razor blade
50 mm Aluminum dish

Equipment needed

Desiccator
Heating oven
Plasma Oxidizer

Procedure day 1

1. Mix 50 g PDMS with 5 g curing agent (ratio of 10:1) and remove air bubbles by placing the mixture in a desiccator for 10 minutes.
2. Pour 1 mL of the PDMS mixture on the bottom of the P100 plastic dish to secure the developed silicon wafer in place by baking this setup at 60ºC in the heating oven for 10 minutes.
3. Remove the plastic dish from the heating oven and pour 10 mL of the PDMS mixture over the features on the developed wafer.
4. Place the PDMS mixture covered developed wafer in the desiccator for 10 minutes to remove any air bubbles.
5. Add the remaining PDMS mixture to the developed wafer and remove any air bubbles again by placing this in the desiccator for 10 minutes.
6. Place the PDMS mixture covered developed wafer in the heating oven at 60ºC to fully polymerize overnight.

Procedure day 2

1. Gently peel the PDMS negative mold from the developed wafer.
2. Cut the negative mold at the edge of the pattern using a razor blade.
3. Plasma oxidize the negative mold at full power for 1 minute.
4. Place the negative mold in a desiccator containing a separate plastic dish that has a drop of silane overnight.

Procedure day 3

1. Mix 50 g PDMS with 5 g curing agent mixture for 1 minute and place in the desiccator for 10 minutes.
2. Pour 1 mL PDMS on the bottom of a 55 mm aluminum dish.
3. Place the negative mold on top of the PDMS covered aluminum dish.
4. Bake the aluminum dish with its contents for 10 minutes at 80ºC.
5. Remove the aluminum dish and pour 10 mL PDMS on top of the negative mold and desiccate for 10 minutes to remove air bubbles.
6. Pour the remaining PDMS mixture over the negative mold and degas once more for 10 minutes.
7. Transfer this negative mold to the heating oven to bake overnight at 80ºC.

Procedure day 4

1. Gently peel the positive mold, which is now called the stamp layer, from the negative mold and cut individual stamps with a razor blade at the periphery of the device features.
2. Plasma oxidize the stamps at full power for 1 minute.
3. Place the stamps in a desiccator containing a separate plastic dish that has a drop of silane overnight.
4. The next day the stamps are ready to be used for microfluidic device fabrication.

6.3 Microfluidic Device Fabrication

Materials needed

Plastic cups
2” by 3” glass slides (VWR)
Polydimethylsiloxane (PDMS)
Curing agent
Transfer pipette
Silicon wafer with a rectangular well
Razor blade (VWR)
22 mm by 22 mm glass cover slip (VWR)

Equipment

Heating oven
Plasma oxidizer
Desiccator
Weight scale
Spin coater
Hot plate

Procedure

1. Mix PDMS and curing agent in a plastic cup at a 10:1 ratio for 1 minute. From herein this mixture will be referred to as PDMS.
2. Place the plastic cup to degas in a desiccator for 10 minutes or until all air bubbles have been removed from the PDMS.
3. Use a transfer pipette to pour 1 mL of PDMS on top of previously fabricated stamps.
4. Place the PDMS covered stamps in the desiccator to degas for 10 minutes.
5. Pour 1 mL PDMS on a 2" by 3" glass slide.
6. Place this glass slide on a spin coater and spin at 1,000 revolutions per minute for 15 seconds.
7. Transfer this glass slide to a heating oven preset to 150ºC for 3 minutes.
8. Remove the glass slide from the heating oven and invert the desiccated PDMS covered stamps to the thin PDMS layer covered glass slide. (Do this step slowly without introducing any bubbles).
9. Place the inverted stamps on the glass plate to the heating oven for 7 minutes.
10. Pour 1-2 mL PDMS onto a silicon wafer with a rectangular well in the middle.
11. Place the PDMS covered silicon wafer on a hot plate preheated to 80ºC for 3 minutes.
12. Remove the silicon wafer from the hot plate once the PDMS has reached medium polymerization consistency.
13. Peel the medium-level polymerized PDMS layer, which will now be referred to as the "sticky" layer, and lay it flat on top of a clean lab bench surface.
14. Remove the inverted stamps from the heating oven and gently peel the stamps from the PDMS layer, which will now be referred to as the device feature layer.
15. Place the device feature layer inside the plasma oxidizer for 20 seconds at half of the maximum intensity.
16. Cut the device feature layer 3 mm from the closest feature edge using a razor blade and through the needle guides to leave an opening.
17. Place the cut-device feature layer on top of the "sticky" layer fabricated in step 13 above.
18. Cut out 2 "sticky" layers per device with a razor blade by using the cut-device feature layer as a template.

19. Place the cut-device feature layer on a 22 mm by 22 mm glass cover slip without introducing any air bubbles between the feature layer and the glass cover slip.
20. Take the 2 “sticky” layers and place them directly on the cut-device feature layer.
21. Place the assembled three-layer microfluidic device to fully polymerize at 150ºC for 30 minutes or at 80ºC for overnight.

6.4 Plasma Etching

Materials needed

P100 plastic plates
Microfluidic device feature layers

Equipment

Plasma etcher

Procedure

1. Place microfluidic sample on a plastic plate and slide into the main glass chamber.
2. Turn on the pump (flip switch up).
3. Turn on the power (press button).
4. Turn on the vacuum (button).
5. Push the glass chamber door to seal the central chamber.
6. Close the main door.
7. Wait until the inside pressure drops below 700 mTorr.
8. Press radio frequency (RF) button and fine tune the knob to desired power level.
9. You should see a light purple color in the central chamber.
10. After 30 seconds press the RF button to turn off the plasma.
11. Press vent and wait for glass chamber door to open.
12. Turn off vent.
13. Press the vacuum button for 5 seconds and press it again to turn off.
14. Turn off the pump and close the main door.
15. Turn off the main power by pressing the power button.

6.5 Microfluidic Device Acid Etching

Materials needed

Sulfuric acid H_2SO_4 (VWR, 7664-93-9)
Polymerized microfluidic device
Razor blade
4 mg/mL or 10 mg/mL collagen stock
PBS
P100 plastic dish

Equipment

200 µL pipette
Portable UV light with short frequency setting

5M H_2SO_4 sulfuric acid preparation

1. Add 5.33 mL stock sulfuric acid to 14.67 mL of deionized water.

Dilute collagen preparation

1. Aliquot 5µL of 4 mg/mL collagen stock into a 15 mL conical test tube.
2. Add 995 µL PBS to the test tube and mix using a 1000 µL pipette to create the 20 µg/mL collagen concentration.
3. If a 10 mg/mL collagen stock is used then for a 5 µL aliquot, dilute in 2,495 µL PBS.

Acid etching procedure

1. Puncture holes with a standard acupuncture above the central chamber in the 4 corners.
2. Inject 50 µL of 10 N sulfuric acid through one of the ports using a 200 µL pipette and leave on the lab bench for 90 minutes at room temperature.
3. Remove the acid by washing the central chamber with 50 µL distilled water a total of five times.
4. Transfer the microfluidic device to a P100 plastic dish.
5. Inject 50 µL of 20 µg/mL collagen into the central chamber and apply UV light over the microfluidic device using a portable UV device with the frequency set to short wave for 30 minutes at room temperature.
6. Store the sterilized microfluidic device at 4ºC in the fridge.

6.6 Tissue Culture Laminar Hood General Sterilization

Materials needed

70% ethanol spray bottle
Disposable latex gloves
Paper towels
White laboratory coats

Equipment

Tissue culture laminar flow hood

Procedure

1. Wash hands in soap for 1 minute and dry completely prior to entering the laboratory.
2. Enter the lab with the appropriate size lab coat.
3. Put on the appropriate size disposable latex gloves.
4. Spray outside glass of the laminar hood with 70% ethanol and wipe with paper towel until dry.
5. Spray gloves with 70% ethanol and rub hands until dry prior to entering the laminar flow hood.
6. Spray inside area of the laminar flow hood with 70% ethanol and wipe with paper towel until dry.

Additional notes

1. Whenever working in the laminar hood, always imagine an invisible tube propagating form each open container that must never be crossed with one's own hands. In the event this happens, sterility of that open container is compromised.
2. Whenever working in the laboratory, always wear lab coat and disposable latex gloves.

6.7 Tissue Culture Cell Medium Preparation

Materials needed

Endothelial basal medium (EBM-2, Lonza, #190860)
Ascorbic acid (Sigma, #A4544)
Chemically defined lipid concentrate (Life Technologies, # 11905031)
Ethyl alcohol absolute (Decon Labs, 64-17-5)
Fetal bovine serum (FBS) (VWR)
human basic fibroblast growth factor (hBFGF) (Sigma, #F0291) (Gibco, #PHG0023)
HEPES 1M (Life Technologies, #15630-080)
Hydrocortisone 1mg (Sigma, #H0135)
Penicillin (10,000 units/ml) & Streptomycin (10,000 µg/ml) (Life Technologies, #15140-122)
Distilled water

Equipment needed

Tissue culture laminar flow hood
Aspirator vacuum flask

Solution preparation

Ascorbic acid

1. Prepare 1 mg/mL concentration of ascorbic acid in distilled water.
2. Sterile filter the solution with a 0.2 µm filter.
3. Prepare 3-5 mL aliquots and store in -20ºC freezer.

bFGF solution

1. Prepare 50 µg/mL stock solution by dissolving 25 µg bFGF in 500 µL PBS.
2. Mix 50 µL of this stock solution with 12.5 mL of EBM-2 to make a 200 ng/mL bFGF solution.
3. Prepare aliquots and store in the -20ºC freezer.

Hydrocortisone solution

1. Dissolve 1 mg hydrocortisone in 1 mL ethyl alcohol absolute to make a 2000X hydrocortisone solution.
2. Prepare 100 µL aliquots and store in the -20ºC freezer.

Endothelial Growth Medium (EGM) preparation

1. Remove EBM-2 bottle (500 mL) from 4ºC fridge and place in tissue culture laminar hood.
2. Remove ascorbic acid, bFGF, FBS, hydrocortisone, and penicillin-streptomycin from -20ºC freezer and place in tissue culture laminar hood and allow these reagents to thaw.
3. Remove 45.25 mL EBM-2 from the stock EBM-2 bottle and place in a 50 mL test tube at 4ºC.
4. Add 2.5 mL 1 mg/mL ascorbic acid to the EBM bottle for a final concentration of 5 µg/mL.
5. Add 2.5 mL 200 ng/mL bFGF to the EBM bottle for a final concentration of 1 ng/mL.
6. Add 5 mL of chemically defined lipid concentrate for a final concentration of 1/100.
7. Add 25 mL of FBS for a final concentration of 5%.
8. Add 5 mL of 1M HEPES for a final concentration of 1.4 µM.
9. Add 5 mL penicillin-streptomycin for a final concentration of 1%.

10. Label the EBM-2 bottle with endothelial growth medium (EGM) complete, date, and name initials.
11. Transfer the EGM complete bottle to 4ºC fridge for storage.

Dulbecco Modified Eagle Medium (DMEM) preparation

1. Remove DMEM bottle from 4ºC fridge and place in tissue culture laminar hood.
2. Add 50 mL FBS to the stock DMEM bottle.
3. Add 10 mL Amino acid solution to the stock DMEM bottle.
4. Add 5 mL penicillin-streptomycin to the stock DMEM bottle.
5. Label the DMEM bottle with DMEM complete, date, and name initials.
6. Transfer the DMEM complete bottle to 4ºC fridge for storage.

Astrocyte Growth Medium (AGM) preparation

1. Remove astrocyte bullet kit from freezer and Astrocyte Basal Medium (ABM) from 4ºC fridge.
2. Place bullet kit contents (FBS, ascorbic acid, rhEGF, GA-1000, insulin, and L-Glutamin) in the foam antibody floater in a 37ºC water bath for 15 minutes.
3. Use 5 mL stripette to transfer all the bullet kit contents to the ABM stock solution.
4. Place the AGM sticker over the ABM sticker on the bottle.
5. Label the bottle with AGM complete, date, and name initials.

6.8 Tissue Culture Cell Maintenance

Materials needed

Specific cell medium (EGM, DMEM, AGM)
Tissue culture plates (P100)
5 mL and 10 mL glass stripettes
Glass Pasteur pipettes (VWR)
1000 µL pipette
70% ethanol spray bottle
0.05% trypsin (VWR)
PBS
Dimethyl sulfoxide (DMSO) (VWR, 67-68-5)
Fetal Bovine Serum (FBS) (VWR)
Freezing down 1-2 mL conical vials (cryo-vials)
Isopropyl lab-grade alcohol (Sigma-Aldrich, 67-63-0)
Distilled water
15 mL test tubes

Permanent marker

Equipment needed

Laminar flow hood
-80ºC Isopropyl alcohol conical vial container
-80ºC freezer
Incubator
Liquid nitrogen Dewar
Water bath
Vacuum aspirator
Centrifuge

Cell thawing

1. Aliquot 4 mL of cell-type appropriate medium to a 15 mL test tube by using a 5 mL stripette. Allow to sit at room temperature for 10 minutes.
2. Remove the desired cell-type vial from the liquid nitrogen Dewar.
3. Submerge ¾ of the vial in a 37ºC water back for 1 minute while gently swirling the vial in a circular motion. Remove once vial appears to be thawed.
4. Pipette the 1 mL cell solution contents to the previously aliquoted 4 mL medium.
5. Using a 1000 µL pipette, gently mix the solution for 30 seconds.
6. Centrifuge the 15 mL conical vial containing the 5 mL of cell/medium solution for 5 minutes at 160 G.
7. Aspirate the supernatant while keeping the cell pellet intact at the bottom of the 15 mL test tube.
8. Resuspend the cell pellet in 1 mL of medium and plate this 1 mL cell medium solution into 2 – P100 plates. For endothelial cells, use gelatin coated plates.
9. Add medium to the P100 plates to bring the total medium volume to 8 mL per plate for endothelial cells, 12 mL for astrocytes, and 12 mL for pericytes.
10. Check under the brightfield microscope for the presence of suspended cells.
11. Transfer plates to an 37ºC incubator with 5% CO_2 and appropriate levels of distilled water in the water reservoir at the bottom of the incubator.

Cell feeding

1. Remove cell medium from 4ºC and place in tissue culture laminar hood for 15 minutes.
2. Transfer cell plate form the incubator to the stage of a brightfield microscope.
3. Verify that the cells are attached and that the color of the medium is clear.
4. Transfer the cell plate to the tissue culture laminar hood.
5. Use a new glass Pasteur pipette to aspirate the medium from the plate by tilting the plate towards you.
6. Add 2 mL of PBS to the cell plate and gently swirl the cell plate in all directions so that the solution covers the entire surface area of the plate.

7. Aspirate the solution and add 8 mL of EGM for endothelial cells, 12 mL of AGM for astrocytes, and 12 mL of DMEM for pericytes.
8. Transfer the cell plate back to the incubator.

Cell splitting

1. Remove cell medium from 4ºC and place in tissue culture laminar hood for 15 minutes.
2. Transfer cell plate form the incubator to the stage of a brightfield microscope.
3. Verify that the cells are attached and that the color of the medium is clear.
4. Transfer the cell plate to the tissue culture laminar hood.
5. Use a new glass Pasteur pipette to aspirate the medium from the plate by tilting the plate towards you.
6. Add 2 mL of PBS to the cell plate and gently swirl the cell plate in all directions so that the solution covers the entire surface area of the plate.
7. Aspirate the solution, add 1 mL of 0.05% trypsin, and incubate at 37ºC for 5 minutes.
8. Transfer cell plate form the incubator to the stage of a brightfield microscope.
9. Verify that the cells are detached from the plate.
10. Transfer the cell plate to the tissue culture laminar hood.
11. Using the 5 mL pipette, pipette 4 mL of medium to the cell plate.
12. Swirl the plate gently for 10 seconds and tilt the plate towards you.
13. Pipette the 5 mL solution into a 15 mL conical test tube.
14. Pipette 10 µL of the solution to a hemocytometer and count the cells.
15. Centrifuge the 15 mL test tube at 160 G for 5 minutes.
16. Aspirate the supernatant and resuspend the cell pellet in 1 mL of medium.
17. Using the counted cell number, add the appropriate cell solution volume so that 200,000 cells are plated per P100 dish.
18. Bring the total cell medium volume per dish to 8 mL of EGM for endothelial cells, 12 mL of AGM for astrocytes, and 12 mL of DMEM for pericytes
19. Transfer the cell plate back to the incubator.

Cell counting

1. Pipette 10 µL of the cell solution to a hemocytometer.
2. Count the number of cells in the 16 (4 by 4) boxes per quadrant (4 quadrants total).
3. Multiply the average of the total 4 cell counts from the 4 quadrants by 10,000. This number has units of cells per mL.
4. Multiply this number by the total volume of cell solution and the new number gives the total number of cells.
    a. For example, to achieve a 2 M/mL seeding density for a 100 µL gel perform the following:
        i. Have the cell density of the suspended cells ready in units of cells/mL.

ii. For 100 µL gel we need 200,000 cells. (100µL/1000µL*2M/mL)
iii. To calculate the volume to draw in mL from the suspended cell solution we divide the number of cells needed by the cell density of the suspended cell solution.

Cell freezing

1. Remove DMSO from -20ºC freezer and place at room temperature until the solution thaws. This can take up to 2 hours depending on the volume of the aliquot.
2. Remove FBS aliquot from 4ºC fridge and place in tissue culture laminar hood.
3. Count the total number of cells for freezing (Always freeze round number of cells such as 1 million, 2 million, etc.)
4. Centrifuge cell solution at 160G for 5 minutes.
5. Prepare the required number of freezing conical vials (cyrovials) by labeling each vial with a +1 passage than the cell passage currently being centrifuged. Additionally, add cell type, date, and your name initials on the cyrovial using a permanent marker.
6. Each 1 million of cells will be frozen in 1 mL of final solution volume.
7. Divide the final solution volume in half and take this amount of FBS and add to a test tube (solution A).
    a. For example, to freeze 1 million cells there will be a final solution volume of 1 mL. Add 0.5 mL FBS to a test tube (solution A).
8. Take 10% of the final solution volume and take this amount of DMSO and add it to a new test tube (solution B). For endothelial cells freeze down final solution volume in 5% DMSO.
    a. For example, to freeze 1 million cells there will be a final solution volume of 1 mL. Add 0.10 mL DMSO to a test tube (solution B).
9. Add the total volume in solution A and solution B, and subtract this from the final solution volume. Take this remaining solution volume and add this amount of FBS to solution B.
    a. For example, to freeze 1 million cells there will be a final solution volume of 1 mL. The volume of FBS that needs to be added to solution B is: 1 mL – 0.5 mL – 0.10 mL= 0.40 mL
10. Remove the cell solution from the centrifuge and aspirate the supernatant.
11. Resuspend the cell pellet in solution A and mix gently with a 200 µL pipette.
12. Slowly add solution B to solution A and mix gently with a 200 µL pipette.
13. Transfer the mixed solution to each prepared cryovial at 1 mL per vial.
14. Place all the cyrovials in a -80ºC isopropyl alcohol container that has been equilibrated to room temperature for at least 30 minutes.
15. Transfer the isopropyl container to a -80ºC freezer for 1-2 days.
16. Transfer the cryovials to the liquid nitrogen Dewar.

Additional notes

1. Whenever working with cells always change the glass Pasteur pipette for a new one when aspirating with the vacuum aspirator.
2. Always label cell plates with the appropriate passage number, cell type, date, and your name initials.

6.9 Collagen Preparation

Materials needed

70% ethanol spray bottle
Forceps
Collagen-I (MP Biomedical #0215002683)
Acetic acid, glacial 99.9+% (Fisher Scientific #64-19-7)
Sterile distilled water
Parafilm
50 mL conical test tube

Equipment

Tissue culture laminar flood hood
Weight scale
Glass vial with a flat bottom
Autoclave

Acetic acid pH calculation

1. pKa of acetic acid= 4.76
2. $4.76 = -\log_{10}Ka$
3. $Ka = 10^{-4.76}$
4. $Ka = [H_3O^+][CH_3COO^-]/[CH_3COOH] = x^2/0.2-x$
5. $x^2 = 0.02 \times 10^{-4.76}$
6. $x = 5.895 \times 10^{-4}$
7. $pH = -\log (5.895 \times 10^{-4})$
8. pH= 3.2295

0.02 M acetic acid calculation

1. Density: 1005 g/ L.
2. Molecular weight: 60.05 g/mol.
3. Want 40 mL 0.02 M acetic acid solution.
4. Stock solution of acetic acid is 16.74 M (density/molecular weight).
5. $c_1v_1=c_2v_2$
6. v_1 = (0.02M x 40 mL)/ 16.74 M = 0.0478 mL of acetic acid

Acetic acid preparation

1. Transfer stock acetic acid from room temperature and place in tissue culture laminar hood.
2. Sterilize distilled water using the autoclave.
3. Aliquot 20 mL sterile distilled water in a 50 mL conical test tube.
4. Add 47.8 µL of 0.02M acetic acid to the 20 mL distilled water slowly.
5. Bring the total solution volume to 40 mL by adding more sterile distilled water.
6. Place 0.02M acetic acid solution in 4ºC in the fridge.

Collagen preparation

1. Remove stock collagen bottle and 0.02M acetic acid from 4ºC fridge and place in tissue culture laminar hood.
2. Sterilize glass vial in the autoclave and sterilize forceps with 70% ethanol.
3. Weigh the empty glass vial.
4. Transfer collagen from the stock bottle to the sterilized glass vial using the forceps in the culture hood.
5. Weigh the collagen containing glass vial and determine the amount of 0.02M acetic acid to add. Make either 10 mg/mL or 4 mg/mL collagen stock solutions. For a 10 mg collagen weight add 1 mL of 0.02M acetic acid to make 10 mg/mL stock collagen solution for add 2.5 mL 0.02M acetic acid to make 4 mg/mL stock collagen solution.
6. Add the desired amount of 0.02M acetic acid to the collagen containing glass vial in the culture hood.
7. Wrap parafilm around the edge of the cap of the collagen bottle and storage at 4ºC.
8. Place the glass vial on a rocker on a low speed setting for 1-2 days at 4ºC. Once the collagen has solubilized then the collagen solution is ready for usage.

Additional notes

1. Use the collagen solution within 4 weeks after preparation.

6.10 Gelatin Coating of Cell Culture Plates

Materials needed

Gelatin powder (Sigma-Aldrich, 9000-70-8)
Tissue culture plates
10 mL glass stripette
500 mL glass bottle
Weight boat

Equipment

Autoclave
Weight scale
Tissue culture laminar flow hood

Gelatin preparation

1. Weigh 0.5 g gelatin powder in a weight boat.
2. Add the 0.5 g gelatin to an empty, clean, and dry 500 mL glass bottle.
3. Add 500 mL of Millipore (MillQ) water to the 500 mL glass bottle.
4. Swirl the bottle to mix the gelatin.
5. Autoclave the 500 mL glass bottle.
6. Cool the 0.1% gelatin solution to room temperature.
7. Store the 0.1% gelatin solution at 4ºC. Use this solution within two months of preparation.

Gelatin plate coating

1. Place the plates to be gelatin coated inside the tissue culture hood.
2. Add 0.1% gelatin solution to cover the entire bottom surface of the plates. For 6 well plates use 0.5 mL 0.1% gelatin solution per well. For p100 plates use 2 mL 0.1% gelatin solution.
3. Tilt the plates in a circular motion for the gelation solution to cover the entire surface area of the plate.
4. Leave in the tissue culture hood for a minimum of 4 hours before using or preferably in the tissue culture hood overnight with the laminar air flow turned on.

6.11 Immunofluorescence Studies

Staining for tight junctions and actin

Materials needed

PBS
4% paraformaldehyde (VWR)
Dissecting forceps with curved tips
Triton X-100 (Sigma-Aldrich, 9002-93-1)
Bovine serum albumin (BSA) (VWR)
ZO-1 (anti-rabbit) (Cell Signaling Tech)
Alexa Fluor 555 (anti-rabbit) (Cell Signaling Tech)
DAPI (Hoechst) (Invitrogen, SLF2020)

Fixing

1. Wash sample with 2-3 mL PBS three times at room temperature.
2. Add 2-3 mL 4% paraformaldehyde per sample for 20 minutes at room temperature.
3. Repeat step 1.

Permeabilizing

1. Remove sample from microfluidic device using dissecting forceps with curved tips and place in individual well in a 6-well plate.
2. Add 0.5 mL 0.2% Triton X-100 (diluted in PBS) per sample for 20 minutes at room temperature.
3. Wash sample with 0.5 mL PBS three times at room temperature.
4. Add 0.5 mL of Phalloidin (1:100 dilution in PBS) and DAPI (1:500 dilution in PBS) per sample for 45 minutes at 37°C.
5. Repeat step 3.
6. Sample ready to be imaged unless need to stain for tight junctions (follow "Blocking" section below)

Blocking

1. Add 0.5 mL 3% BSA (diluted in PBS) for 30 minutes at room temperature.
2. Wash sample with 0.5 mL PBS three times at room temperature.

Primary/secondary staining

1. Add ZO-1 (1:250 dilution in PBS) and 3% BSA (dilution in PBS) for overnight at 4ºC.
2. Next day wash sample with 0.5 mL PBS three times at room temperature.
3. Add Alexa Fluor 555 (1:500 dilution in PBS) for 1 hour at 37ºC.
4. Wash sample with 0.5 mL PBS three times at room temperature.

Staining for tight junctions and axons

Materials needed

PBS
4% paraformaldehyde
Dissecting forceps with curved tips
Triton X-100 (Sigma-Aldrich, 9002-93-1)
Normal donkey serum (Immuno Reagents, sp-072-vx10)
ZO-1 (anti-rabbit) (anti-rabbit) (Cell Signaling Tech)
Beta-III Tubulin Tuj1 (anti-mouse) (Biolegend)
Alexa Fluor 555 (anti-rabbit) (anti-rabbit) (Cell Signaling Tech)

DyLight 650 conjugate (anti-mouse) (Immuno Reagents)
DAPI (Hoechst) (Invitrogen, SLF2020)

Equipment

Laser scanning confocal microscope (Nikon A1R)

Fixing

1. Wash sample with 2-3 mL PBS three times at room temperature.
2. Add 2-3 mL 4% paraformaldehyde per sample for 20 minutes at room temperature.
3. Repeat step 1.

Blocking/Permeabilizing

1. Remove sample from microfluidic device using dissecting forceps with curved tips and place in individual well in a 6-well plate.
2. Add 0.5 mL 0.2% Triton X-100 (diluted in PBS) per sample for 20 minutes at room temperature.
3. Wash sample with 0.5 mL PBS three times at room temperature.
4. Add 0.5 mL 10% normal donkey serum (diluted in PBS) per sample for 10 minutes at room temperature.
5. Repeat step 3 (not required).
6. Remove normal donkey serum.

Primary/secondary staining

1. Incubate with 0.5 mL per sample of ZO-1 (1:250 dilution in PBS), Tuj (1:500 dilution in PBS), and 2% normal donkey serum (diluted in PBS) for 2 hours at room temperature.
2. Wash sample with 0.5 mL PBS three times at room temperature.
3. Incubate with 0.5 mL per sample of Alexa Fluor 555 (1:500 dilution in PBS), 650 Conjugate (1:500 dilution in PBS), DAPI (1: 500 dilution in PBS), and 2% normal donkey serum (diluted in PBS) for 1 hour at room temperature.
4. Repeat step 2.
5. View sample using confocal microscope.

6.12 Sample Preparation for Scanning Electron Microscope

Materials needed

PBS

Glutaraldehyde (VWR)
Ethanol
SEM stage stud
Double-faced carbon conductive adhesive tape
Carbon adhesive tab (12 mm diameter)
Distilled water

Equipment

Sputter Coater (Cressington model 6002-8)
Scanning electron microscope (Phenom Pure model 800-07332)
Freeze drying instrument (Labconco- FreezeZone 4.5 Plus)

Preparation

1. Wash sample with 2-3 mL PBS three times at room temperature.
2. Incubate sample in 2-3 mL 5% glutaraldehyde for 30 minutes at 4ºC (dilution in distilled water).
3. Wash sample with 2-3 mL PBS three times at room temperature.
4. Sequentially dehydrate sample in 2-3 mL of 20%, 50%, 70%, 90%, and 100% ethanol for 10 minutes at room temperature. (all dilutions in distilled water)
5. Place sample in freeze drying instrument for 2 hours.

Sputter coating

1. Remove top layer of microfluidic device to expose the sample.
2. Place a double-faced carbon conductive adhesive tape on a carbon adhesive tab.
3. Place sample on the side of the tab that is covered by the adhesive tape.
4. Place the entire tab (containing the sample) inside the sputter coat holder.
5. Sputter coat for 8 seconds with 30 mA current.
6. View sample using the scanning electron microscope.

6.13 Blood-Brain Barrier Model (180 µm Diameter) Fabrication

Materials needed

180 µm sterile acupuncture needles (DBC)
Dilute collagen coated microfluidic devices
10 mg/mL collagen solution
Sterile distilled water
0.1 M NaOH (VWR)
10x PBS
hCMEC/d3 cells (Dr. Nagele)
Normal human astrocytes (NHA) (Lonza)

Matrigel (10 mg/mL stock) (Corning)
Extra Link (HyStem kit, Glycosan)
Hyaluronan- HA- Thiol-modified (Hystem kit, Glycosan).
AGM (Lonza)
EGM (Lonza)
Sterile flat forceps

Equipment

Incubator
Tissue culture laminar flow hood
Aspirator vacuum flask

Protocol

1. Place sterile dilute collagen coated microfluidic device inside the tissue culture laminar hood.
2. Prepare 180 µm acupuncture needles by placing them inside the tissue culture hood.
3. Prepare NHA at a seeding density of 1 M/mL and centrifuge the cells at 160 G for 5 minutes.
4. Remove 0.1 M NaOH, 10x PBS, distilled water, and HA from 4ºC fridge.
5. Per device make 50 µL total hydrogel volume.
6. In a 15 mL conical test tube add these reagents together in the following order: 5 µL 10x PBS, 5 µL 0.1 M NaOH, 2.5 µL distilled water, and 5 µL HA.
7. Place all of these reagents back at 4ºC in the fridge and remove Matrigel and Xtra Link from 4ºC fridge.
8. Add 5 µL Matrigel and 2.5 µL Xtra Link to the previous solution of reagents.
9. Place the matrigel and Xtra Link back at 4ºC in the fridge and take out the 10 mg/mL collagen solution.
10. Aspirate the supernatant from the cell pellet.
11. Pipette 25 µL of 10 mg/mL collagen solution in a pipette tip and quickly return the 10 mg/mL collagen solution back at 4ºC in the fridge.
12. Return to the tissue culture hood and pipette the collagen in with the other reagents gently for 1 minute without introducing any air bubbles.
13. Resuspend the cell pellet with the hydrogel mixture solution carefully for 1 minute.
14. Aspirate dilute collagen from the central chamber of the microfluidic device.
15. Inject 50 µL solution into the central chamber of the microfluidic device through an open port above the central chamber.
16. Place 180 µL acupuncture needles in through the needle guides and gently push until slight resistance is felt.

17. Carefully transfer the p100 plastic plate containing the microfluidic device with the needles inside the collagen hydrogen to a 37ºC incubator for 10 minutes.
18. Remove the microfluidic device from the incubator and add 150 µL of AGM on top of the microfluidic device above the central chamber.
19. Place the device back in 37ºC incubator for another 40 minutes.
20. Prepare hCMEC/d3 cells at a seeding density of 5 M/mL.
21. Remove the device from the incubator and place inside the tissue culture hood.
22. Using sterile flat forceps gently grab and pull the needle tips.
23. Centrifuge hCMEC/d3 cells at 160 G for 5 minutes.
24. Aspirate supernatant and resuspend in the proper volume of EGM to achieve a density of 5 M/mL.
25. Inject 10 µL of the cell EGM solution into the cell seeding port on the microfluidic device.
26. Place the device in the incubator for 10 minutes.
27. Remove the device and inject another 10 µL into the same cell seeding port on the microfluidic device.
28. Invert the device upside down and place in the incubator for 10 minutes.
29. Remove the device from the incubator and connect to flow pump.

6.14 Perfusing Microfluidic Devices with Flow

Materials needed

Microfluidic device that has been cell seeded
Tubing
Plastic syringes (BD)
6 well plate
Silicon grease (Bayer)
EGM complete

Equipment needed

Syringe pump (Genie Touch) (Kent Scientific)
Dremmel
Brightfield microscope

Protocol

1. Place microfluidic device inside the tissue culture hood.
2. Drill 4 mm in diameter circular holes in a single well of a 6 well plate above where the tubing will attach to the microfluidic device.
3. Place the genie touch syringe pump inside the culture hood.

4. Aliquot the needed volume of EGM. A single device required 5 mL of EGM for the syringe and 8 mL EGM for the well to fully cover the microfluidic device.
5. Connect the syringe to the syringe pump and prime the line.
6. Connect the end of the metal rubber tubing to the desired flow port on the microfluidic device.
7. Set the desired flow rate on the pump. For the 180 µm diameter BBB model, the flow rate was set to 2.4 µL/min and for the microvascular model, the flow rate was set to 0.72 µL/min.
8. Click run on the syringe pump and gently apply sterile grease to seal the air vents and the needle guides.
9. Transfer the flow connected device to the stage of a brightfield microscope to ensure uninterrupted flow application.
10. Transfer device to 37ºC incubator for 5 days. Be sure to check on experiment daily and refill the syringes with medium as necessary.

6.15 Microvasculature (~10 µm Diameter) Fabrication within Collagen/HA Model

Materials needed

Dilute collagen coated microfluidic devices
10 mg/mL collagen solution
0.1 M NaOH
10x PBS
hCMEC/d3 cells
hBVP (University of Pennsylvania)
Matrigel (10 mg/mL stock)
5 mg/mL Hyaluronan- (HA)- Not crosslinked (Sigma Aldrich, 9067-32-7)
6.67 mg/mL Hyaluronan- (HA)- Not crosslinked (Sigma Aldrich, 9067-32-7)
EGM complete
20 mg/mL collagen
10 mg/mL collagen

Equipment

Incubator
Tissue culture laminar flow hood
Aspirator vacuum flask

HA preparation

1. Remove HA from -20ºC freezer and weigh 10 grams in a weight boat on a weight scale.
2. Transfer the 10 grams HA powder to a glass vial with a flat bottom.

3. Add 2 mL sterile MilliQ deionized water to the glass vial for a concentration of 5 mg/mL. If making the 6.67 mg/mL concentration solution, then add 1.5 mL sterile MilliQ deionized water.
4. Transfer the glass vial to a rocker at 4ºC for 1-2 days.
5. Place the HA stock solution back to -20ºC freezer.

Protocol

1. Place sterile dilute collagen coated microfluidic device inside the tissue culture laminar hood.
2. Prepare hCMEC/d3 cells at a seeding density of 2 M/mL and prepare hBVP cells at a seeding density of 0.4 M/mL.
3. Centrifuge the cells at 160 G for 5 minutes.
4. Remove 0.1 M NaOH, 10x PBS, and HA from 4ºC fridge.
5. Per device make 25 µL total hydrogel volume.
6. In a 15 mL conical test tube add these reagents together in the following order: 2.5 µL 10x PBS, 2.5 µL 0.1 M NaOH, and 11.25 µL HA-6.67 mg/mL (in vitro collagen/HA formulation). 2.5 µL 10x PBS, 1.25 µL NaOH, and 15 µL HA- 5 mg/mL (in vivo collagen/HA transplantation formulation).
7. Place all of these reagents back at 4ºC in the fridge and remove Matrigel from 4ºC fridge.
8. Add 2.5 µL Matrigel to the previous solution of reagents.
9. Place the matrigel back at 4ºC in the fridge and take out the 10 mg/mL collagen solution.
10. Aspirate the supernatant from the cell pellet.
11. For the in vitro collagen/HA formulation pipette 6.25 µL of 20 mg/mL collagen solution in a pipette tip and quickly return the 20 mg/mL collagen solution back at 4ºC in the fridge. For the in vivo collagen/HA transplantation formulation use 6.25 µL of 10 mg/mL collagen stock solution instead.
12. Return to the tissue culture hood and pipette the collagen in with the other reagents gently for 1 minute without introducing any air bubbles.
13. Resuspend the cell pellet with the hydrogel mixture solution carefully for 1 minute.
14. Aspirate dilute collagen from the central chamber of the microfluidic device.
15. Inject 25 µL solution into the central chamber of the microfluidic device through an open port above the central chamber.
16. Carefully transfer the p100 plastic plate containing the microfluidic device to a 37ºC incubator for 20 minutes.
17. Remove the microfluidic device from the incubator and add 150 µL of EGM on top of the microfluidic device above the central chamber.
18. Place the device back in 37ºC incubator for another 40 minutes.
19. Remove the device from the incubator and connect to flow pump.

6.16 Microvasculature (~10 μm Diameter) Fabrication within the Peptide Model

Materials needed

Dilute collagen coated microfluidic devices
hCMEC/d3 cells
10 mg/mL stock RADA 16-I peptide (Corning)
2 mg/mL RADA 16-I peptide
EGM complete
Human -Vascular endothelial growth factor (VEGF) (VWR)
Phorbol-12-myristate 13-acetate (PMA) (#1544-5) (VWR)
6 well plate
20% sucrose
10% sucrose
FBS
Ice cubes
50 mL conical test tubes

Equipment

Ultrasonic water bath sonicator
Incubator
Tissue culture laminar flow hood
Aspirator vacuum flask
Lab ice machine
Rocker
37ºC hot room

2 mg/mL peptide preparation

1. Take 100 μL of 10 mg/mL stock peptide and add to 15 mL test tube containing 400 μL sterile distilled water.
2. Sonicate this 2 mg/mL peptide solution for 30 minutes in the ultrasonic water bath sonicator at room temperature.

VEGF preparation

1. 10 μg stock VEGF powder was reconstituted in 100 μL 0.1% bovine serum albumin (BSA) for a concentration of 0.1 mg/mL.
2. 25 μL aliquots of 4 μL each were placed in -20ºC freezer for storage.

PMA preparation

1. Solubilized 5 mg PMA in 5 mL DMSO for a stock solution concentration of 1 mg/mL.
2. Aliquoted into 200 μL 25 vials and placed at -20ºC freezer for storage.

20% Sucrose preparation

1. Weigh out 8 grams of sucrose in a weight boat on the weight scale and add to a 50 mL conical test tube.
2. Add distilled water until the 40 mL mark is reached on the 50 mL conical test tube.
3. Place 40 mL sucrose solution on a rocker at a medium setting for 10 minutes at 37ºC (hot room).
4. After visually inspecting that all of the sucrose has dissolved, sterile filter using a 0.2 µm sterile filter by connecting to a vacuum flask aspirator.
5. Store 20% sucrose solution at 4ºC in the fridge.
6. To make 10% sucrose solution, use the same protocol with the exception of weighing out 4 grams of sucrose instead of 8 grams.

Protocol

1. Place sterile dilute collagen coated microfluidic device inside the tissue culture laminar hood.
2. Prepare hCMEC/d3 cells at a seeding density of 5 M/mL.
3. Centrifuge the cells at 160 G for 5 minutes.
4. Remove 2 mg/mL peptide, 20% sucrose, 10% sucrose, FBS, EGM from 4ºC fridge and place all of these reagents in a bucket filled with ice.
5. Per device make 25 µL total peptide volume.
6. Aspirate the supernatant from the cell pellet and resuspend in 1 mL 10% sucrose.
7. Centrifuge the cells at 160 G for 5 minutes.
8. Aspirate the supernatant from the cell pellet and resuspend in 12.5 µL 20% sucrose by mixing gently with a P200 pipette for 15 seconds.
9. Add 12.5 µL 2 mg/mL peptide solution to the 12.5 µL cell sucrose solution and mix gently with a P200 pipette for 30 seconds.
10. Aspirate dilute collagen from the central chamber of the microfluidic device.
11. Inject 25 µL peptide/sucrose/cell solution into the central chamber of the microfluidic device through an open port above the central chamber.
12. Carefully place the microfluidic device to a well of a 6 well plate.
13. Carefully add 100 µL of EGM complete with 10% FBS on top of the microfluidic device above the central chamber where the open ports are for 1 minute at room temperature.
14. Carefully add 8 mL of EGM complete with 10% FBS to the well containing the microfluidic device.
    a. To make EGM complete supplemented with 10% FBS, mix 0.4 mL FBS with 7.6 mL EGM complete supplemented with 5%.
15. Transfer the 6 well plate to 37ºC incubator for 60 minutes.
16. Prepare 8 mL EGM complete supplemented with 100 ng/mL VEGF and 50 ng/mL PMA and keep in ice bucket while the peptide is being incubated.

a. Aliquot 8 mL EGM complete into a 15 mL conical test tube and add 8 µL 0.1 mg/mL VEGF and 0.4 µL 1 mg/mL

17. Remove the 6 well plate with the microfluidic device from the incubator and replace the medium with the one prepared in step 17.
18. Place the 6 well plate back in the 37ºC incubator for 5 days.

Additional notes

1. Once the peptide is injected into the microfluidic device, be sure to carefully add and change medium using a 200 µL pipette. Any sudden movements in the medium can disrupt the peptide, especially while the peptide is being polymerized.

6.17 Scaffold Transplantation into Sprague Dawley Spinal Cord Hemisection Animal Model (Collagen/HA Scaffolds)

Materials needed

Collagen/HA scaffolds
70% ethanol spray bottle
Shipping Styrofoam box
Forceps
10 mg/kg Cyclosporine A

Protocol

1. Transfer day 2 collagen/HA scaffolds to Drexel University Medical School Queen Lane campus in a Styrofoam shipping box that has been sprayed with 70% ethanol on the outside and inside.
2. After arriving at Drexel University, immediately transfer scaffolds to 37ºC incubator until the animals are ready for transplantation.
3. All animals have been administered cyclosporine three days prior to surgeries and during the period after transplantation.
4. Perform laminectomy at the C4-C5 spinal cord level and aspirate to create an acute hemisection injury.
5. Remove scaffolds from the incubator and use sterile forceps to break out the scaffolds from the microfluidic device chambers.
6. Drop the scaffolds in the cavity formed by the hemisection injury.
7. Suture the dura over the cavity to secure the transplant in place.
8. Surgically close the spinal cord and staple the dermis of the rat with 8-10 staples.

Additional notes

1. All animals have been administered cyclosporine A (10 mg/kg) three days prior to surgeries and during the period after transplantation

6.18 Scaffold Transplantation into Sprague Dawley Spinal Cord Contusion Animal Model (Peptide Scaffolds)

Materials needed

200-250g Sprague Dawley female rats
Sutures
Medical surgical instruments
2 mg/mL RADA 16-I peptide
20% sucrose (VWR)
10% sucrose
0.05% Trypsin
Endothelial Growth Medium (EGM-Complete)
Dulbecco Modified Eagle Medium (DMEM)
Sutures
Medical staples
P19-P22 GFP hCMEC/d3
P7-P18 GFP hBVP
15 mL test tubes
RADA 16-I peptide
P75 and cell culture dishes
Hemocytometer
200 µl and 1000 µL pipettes
10 µL surgical syringe
30 G needle
Matrigel

Equipment

IH Infinity Horizontal Impactor, Lexington (model #0400)
Miniature force sensor (PCB- 209c11)
Micro Syringe Pump Controller (Micro4)
Centrifuge
Vacuum flask aspirator
Brightfield microscope

Spinal cord contusion

1. Perform laminectomy to expose the C4/C5 spinal cord region on 200-250g Sprague Dawley female rats.
2. Secure a miniature force sensor to the IH Infinity Horizontal Impactor.

3. Transfer rats with exposed spinal cords to the stage of the IH Infinity Horizontal Impactor.
4. Place the miniature force sensor 2 mm above the exposed spinal cord.
5. Drop and apply a force of 150,000 Dynes to the spinal cord at the C4/C5 spinal cord region.
6. Stitch a black suture next to the contusion epicenter to know where to perform the peptide injection seven days later.
7. Surgically close the spinal cord and staple the dermis of the rat with 8-10 staples.

Cell preparation

1. Thaw 1 vial of p 19 GFP human cerebral microvascular endothelial cells (hCMEC/d3) and 1 vial of p11 GFP human brain vascular pericytes (hBVP) in a 37ºC water bath for 1 minute.
2. Suspend each vial in 4 mL of EGM for hCMEC/d3 and 4 mL of DMEM for hBVP.
3. Centrifuge each solution at 160 G for 5 minutes.
4. Aspirate supernatant using a vacuum flask aspirator and resuspend the hCMEC/d3 cell pellet in 1 mL of EGM and the hBVP cell pellet in 1 mL DMEM.
5. Plate hCMEC/d3 cells on a p75 gelatin coated flask with 8 mL EGM and plate the hBVP on two non-coated p100 plates with 12 mL DMEM per plate.
6. Replace media the next day and every 2-3 days with 5 mL EGM for the hCMEC/d3 and 12 mL DMEM for each of the hBVP p100 plates.
7. Use cells for experiments once at least 80% cell confluency is reached.

Peptide injections

1. Aspirate medium from each cell plate and add 2 mL 0.05% trypsin per plate for 5 minutes at 37ºC.
2. Gently shake the cell plate and verify with brightfield microscope to ensure that the cells detached from the bottom of the dish.
3. Deactivate trypsin with 3 mL DMEM per dish.
4. Draw the solution into a 15 mL conical test tube and mix with a 1 mL pipette to ensure homogenous distribution of suspended cells.
5. Centrifuge the cells at 160G for 5 minutes and resuspend the cell pellet with fresh medium so that the cells are not exposed to trypsin for a prolonged period of time.
6. Count cells using a hemocytometer by taking 10 µL solution samples per cell type.
7. Aliquot the proper cell solution volume to achieve 5 M/mL and 2.4 M/mL cell density conditions.

i. For the 5 M/mL condition, 100 µL final peptide gel volume required 416,667 hCMEC/d3 cells and 83,333 hBVP cells.
ii. For the 2.4 M/mL condition, 100 µL final peptide gel volume required 200,000 hCMEC/d3 and 40,000 hBVP.

8. Mix the two cell solutions in 1 test tube and centrifuge at 160 G for 5 minutes.
9. Aspirate the supernatant, resuspend the cell pellet with 1 mL 10% sucrose, and centrifuge again at 160G for 5 minutes. This step is necessary to remove any remaining medium which would cause premature peptide polymerization.
10. Aspirate the supernatant and resuspend the cell pellet with 50 µL 20% sucrose. Gently mix the solution with a 200 µL pipette.
11. Add 50 µL 2 mg/mL RADA 16-I peptide to the 50 µL cell suspension in the 20% sucrose. Ensure that the peptide solution has been sonicated for at least 20 minutes within the last 2 weeks.
12. Mix the cell peptide solution for 1 minute using the 200 µL pipette.
13. Draw 10 µL of the cell peptide solution using a 10 µL surgical syringe with a 30 G needle.
14. Connect the 10 µL surgical syringe to the microsyringe pump controller and inject the solution at a flow rate of 100 nL/s.
15. Leave the needle tip inside the spinal cord for 1 minute after the injection stops.
16. Remove the injection needle and apply 20 µL of Matrigel over the location where the peptide was injected.
17. Surgically close the spinal cord and staple the dermis of the rat with 8-10 staples.

Additional notes

1. All animals have been administered cyclosporine A (10 mg/kg) three days prior to surgeries and during the period after transplantation

6.19 Sprague Dawley Rat Perfusion Protocol

Materials needed

Paraformaldehyde reagent
Distilled water
NaOH
Sodium phosphate monobasic
Sodium phosphate dibasic
Euthasol

Equipment

2L Pyrex flask
Hot plate
Standard rat perfusion peristaltic pump
#3 filter
Vacuum flask
Weight scale
Perfusion board
Perfusion needle

Solution preparation

16% paraformaldehyde (1L)

1. Weight out 160g of paraformaldehyde reagent.
2. Add paraformaldehyde to 750 mL distilled water in a 2L Pyrex flask with the top covered in foil.
3. Heat the solution to 90-95ºC while stirring. Be sure not to boil the solution.
4. Turn off hot plate when paraformaldehyde partially dissolves (solution turns milky white) and do not stop stirring.
5. Slowly add 5 or 10 M NaOH solution drop-wise until the solution partially clears (solution will not be completely clear, but will lose the milky appearance).
6. Adjust the final volume to 1 L with distilled water.
7. Filter the solution with a #3 filter using a vacuum flask.
8. Store at 4ºC as stock solution.

0.2M Sodium phosphate buffer

1. Sodium phosphate monobasic (solution A)
2. Sodium phosphate dibasic (solution B)
3. Mix 95 mL of solution A with 405 mL solution B to achieve a 0.2M sodium phosphate buffer with a pH of approximately 7.4.

0.9% saline

1. Add 9 g NaCl to 1L of distilled water and stir until all salt is dissolved.
2. Buffered saline may also be used as a pre-perfusion wash.

4% buffered paraformaldehyde

1. Mix solution:
    i. 1 part 16% paraformaldehyde
    ii. 2 parts 0.2M sodium phosphate buffer
    iii. 1 part distilled water

Animal preparation and perfusion

1. Prime pump with 0.9% saline and verify that there are no bubbles in the line or the syringe
2. Euthanize (deeply anesthetize – overdose) animal with 0.2 mL Euthasol.
3. Tape animal to perfusion board
4. Perform thoracotomy.
5. Incise right atrium/auricle then place perfusion needle into left ventricle or into the aorta.
6. Set peristaltic pump to pump rate setting of 2.5-3 and run saline through the animal until blood clears. The liver should turn from dark red to light brown and the lungs should remain collapsed.
7. Switch to 4% paraformaldehyde and run up to 500 mL through the animal at the same pump rate setting of 2.5-3.
8. Once the muscles have stopped twitching, lower the pump speed to 2. Each animal should have a total perfusion time of 20 minutes.

6.20 Fluorescent Immunohistochemistry (IHC) and Immunocytochemistry (ICC) Staining of In Vivo Glass Slides

Materials needed

PBS
Triton X-100
Goat serum
Paraformaldehyde reagent
Distilled water
NaOH
Sodium phosphate monobasic
Sodium phosphate dibasic
Euthasol

Equipment

10cc syringe
18-gauge needle
Medical forceps
2L Pyrex flask
Hot plate
Standard rat perfusion peristaltic pump
#3 filter
Vacuum flask
Weight scale
Perfusion board
Perfusion needle

Blocking buffer preparation

1. 0.2% Triton X-100
2. 10% goat serum
3. Diluted in PBS

Staining buffer preparation

1. 2% goat serum
2. Antibody at the dilution indicated from the manufacturer
3. Diluted in PBS

Staining day 1

1. Reheat slides (from cryostat sectioning) to room temperature for 30 minutes using a plate warmer.
2. Circle tissue sections with rubber cement (Elmer's) by using a 10cc syringe with 18-gauge needle.
3. Let the glue dry for 30 minutes.
4. Wash slides in PBS 3 times for 5 minutes at room temperature.
5. Block slides with blocking buffer (250 µL per slide) for 1 hour at room temperature.
6. Incubate overnight at room temperature with primary antibody in staining buffer with 250 µL per slide.

Staining day 2

1. Wash slides in PBS 3 times for 5 minutes at room temperature.
2. Incubate slides in the dark with secondary antibody in the staining buffer with 200 µL per slide for 2 hours at room temperature
3. Wash slides in PBS 3 times for 5 minutes at room temperature in the dark. Remove the glue ring with forceps between the 1st and 2nd wash.
4. Allow the slides to dry for 25 minutes at room temperature in the dark.
5. Place coverslip over the slides with mounting medium.
6. Store slides at 4ºC for short term storage or at -20ºC for long term storage.

Additional notes

1. Do not directly pour buffer on the tissue sections.
2. Use a wet brush to flatten sections that being to lift up from the glass slide.
3. Never allow the sections to dry after starting the staining.

6.21 Rheology

Materials needed

Collagen
Peptide (RADA-16I)
Sucrose
DMEM
PBS

Equipment

Rheometer (Discovery- TA Instruments)
Pipettes
Test tubes
1º 20 mm SST ST cone Peltier Plate geometry

Rheometer calibration

1. Turn on rheometer.
2. Calibration order:
    i. Inertia without geometry attached.
    ii. Inertia with geometry attached.
    iii. Friction.
    iv. Rotational mapping.

Protocol (Collagen gels)

1. Turn on and calibrate rheometer.
2. Warm up the 1º cone geometry by "zeroing gap" and leaving in this position (top and bottom plates touching) for 3-5 minutes.
3. Create 40 µL final gel volume with either 5 mg/mL or 2 mg/mL final collagen concentration.
4. Using a 100 µL pipette inject the 40 µL gel on the bottom plate of the rheometer.
5. Press the green start button and rotate manually the top geometry as it comes down on the gel.
6. After 10 minutes add 2 mL DMEM to prevent gel dehydration.
7. Run the test for 20 minutes or until the storage moduli values plateau.

Protocol (Peptide gels)

1. Turn on and calibrate rheometer.

2. Warm up the 1º cone geometry by “zeroing gap” and leaving in this position (top and bottom plates touching) for 3-5 minutes.
3. Create 40 µL final gel volume (20µL 2 mg/mL peptide and 20% sucrose).
4. Using a 100 µL pipette inject the 40 µL gel on the bottom plate of the rheometer.
5. Press the green start button and rotate manually the top geometry as it comes down on the gel.
6. After 1 minute add 400 µL DMEM around the gel to initiate polymerization.
7. Run the test for a 5-10 minutes or until the storage moduli values plateau.

6.2 Statistical Analysis

6.2.1 Mechanical stimulation of 3D in vitro model of the blood-brain barrier.

> my_data

	Day	teer	condition
1	0	1.50446	flow
2	0	146.90154	flow
3	0	635.00202	flow
4	0	-26.98832	no flow
5	0	240.32963	no flow
6	0	184.66869	no flow
7	1	505.83185	flow
8	1	68.16302	flow
9	1	519.83760	flow
10	1	-172.70199	no flow
11	1	122.59236	no flow
12	1	377.19636	no flow
13	2	181.63269	flow
14	2	217.80412	flow
15	2	725.82791	flow
16	2	-88.99623	no flow
17	2	257.54835	no flow
18	2	420.46805	no flow
19	3	348.75410	flow
20	3	726.83573	flow
21	3	810.55810	flow
22	3	98.73924	no flow
23	3	233.63711	no flow
24	3	394.29444	no flow
25	4	770.73825	flow
26	4	1002.92755	flow
27	4	1265.71080	flow
28	4	209.79681	no flow
29	4	291.13178	no flow

```
30   4  434.14640  no flow
> aov2 <-aov(teer~ condition+Day+Day:condition, data=my_data)
> summary(aov2)
             Df  Sum Sq Mean Sq F value   Pr(>F)
condition     1  817465  817465  15.760 0.000506 ***
Day           1  765681  765681  14.761 0.000705 ***
condition:Day  1  244550  244550   4.715 0.039218 *
Residuals    26 1348624   51870
---
Signif. codes:  0 ‘***’ 0.001 ‘**’ 0.01 ‘*’ 0.05 ‘.’ 0.1 ‘ ’ 1
> TukeyHSD(aov2)
  Tukey multiple comparisons of means
    95% family-wise confidence level

Fit: aov(formula = teer ~ condition + Day + Day:condition, data = my_data)

$condition
                diff       lwr       upr     p adj
no flow -flow -330.1445 -501.0877 -159.2013 0.0005057
```

Dextran Permeability:

```
> static=c(13.5634E-6,13.8544E-6,8.4168E-6)
> flow
[1] 9.05472e-07 5.43463e-07 1.03997e-06
> t.test(flow,static)

        Welch Two Sample t-test

data:  flow and static
t = -6.2718, df = 2.0282, p-value = 0.02367
alternative hypothesis: true difference in means is not equal to 0
95 percent confidence interval:
 -1.863992e-05 -3.590547e-06
sample estimates:
  mean of x    mean of y
8.296350e-07 1.194487e-05

> t.test(stretch,static)

        Welch Two Sample t-test

data:  stretch and static
t = -5.8925, df = 2.1018, p-value = 0.02456
alternative hypothesis: true difference in means is not equal to 0
95 percent confidence interval:
```

```
 -1.788640e-05 -3.189607e-06
sample estimates:
   mean of x    mean of y
1.406865e-06 1.194487e-05

> t.test(flow_ec_only,static)

        Welch Two Sample t-test

data:  flow_ec_only and static
t = -5.6697, df = 2.4081, p-value = 0.01918
alternative hypothesis: true difference in means is not equal to 0
95 percent confidence interval:
 -1.733145e-05 -3.701432e-06
sample estimates:
   mean of x    mean of y
1.428425e-06 1.194487e-05

> t.test(flow_ec_only_tnf_a,static)

        Welch Two Sample t-test

data:  flow_ec_only_tnf_a and static
t = -0.44684, df = 2.6923, p-value = 0.6885
alternative hypothesis: true difference in means is not equal to 0
95 percent confidence interval:
 -1.744560e-05  1.339112e-05
sample estimates:
   mean of x    mean of y
9.917630e-06 1.194487e-05

> t.test(flow_tnf_a,static)
    Welch Two Sample t-test
data:  flow_tnf_a and static
t = -1.5224, df = 3.0225, p-value = 0.2246
alternative hypothesis: true difference in means is not equal to 0
95 percent confidence interval:
 -1.694837e-05  5.948757e-06
sample estimates:
   mean of x    mean of y
5.010787e-06 1.051059e-05
```

6.2.2 Neurovascular interaction to guidance axon growth.

3D in vitro microvessel formation, Figure 1.

Welch Two Sample t-test

```
data:  static5 and flow5
t = 1.9818, df = 26.578, p-value = 0.05793
alternative hypothesis: true difference in means is not equal to 0
95 percent confidence interval:
 -1.322814 74.620147
sample estimates:
mean of x mean of y
 241.9160  205.2673
```

```
> static5=c(307.56,+ 187.32,+ 281.59,+ 289.67,+ 347.07,+ 258.45,+ 287.49,+ 152.84,+
240.19,+ 267.29,+ 219.88,+ 184.74,+ 239,+ 195.73,+ 169.92);
> flow5=c(227.58,+ 223.98,+ 187.74,+ 303.96,+ 141.46,+ 275.19,+ 260.27,+ 189.44,+
195.16,+ 169.04,+ 180.5,+ 189.7,+ 181.56,+ 175.05,+ 178.38);
> t.test(static5,flow5)
```

3D microvessel alignment with interstitial fluid flow, Figure 2.

ANOVA and Welch Two Sample t-test

```
> res.aov2 <- aov(alignment ~ day + condition, data = my_data)
> summary(res.aov2)
            Df Sum Sq Mean Sq F value   Pr(>F)
day          1   3171    3171   4.988   0.0268 *
condition    1  15709   15709  24.711 1.56e-06 ***
Residuals  177 112523     636
---
Signif. codes:  0 ‘***’ 0.001 ‘**’ 0.01 ‘*’ 0.05 ‘.’ 0.1 ‘ ’ 1
> my_data
    day alignment condition
1     3      1.17      flow
2     3      7.70      flow
3     3      8.53      flow
4     3     15.04      flow
5     3     15.78      flow
6     3     50.11      flow
7     3     53.39      flow
8     3     58.34      flow
9     3     66.97      flow
10    3     75.53      flow
11    3     77.99      flow
12    3     82.57      flow
13    3     83.35      flow
14    3     86.01      flow
15    3     82.69      flow
```

16	3	82.61	flow
17	3	75.00	flow
18	3	72.53	flow
19	3	71.57	flow
20	3	52.13	flow
21	3	46.79	flow
22	3	45.00	flow
23	3	40.43	flow
24	3	30.78	flow
25	3	28.81	flow
26	3	25.02	flow
27	3	22.83	flow
28	3	21.54	flow
29	3	8.13	flow
30	3	7.59	flow
31	4	0.00	flow
32	4	1.26	flow
33	4	4.50	flow
34	4	6.84	flow
35	4	10.51	flow
36	4	12.76	flow
37	4	17.88	flow
38	4	18.14	flow
39	4	29.93	flow
40	4	65.73	flow
41	4	79.70	flow
42	4	71.82	flow
43	4	67.78	flow
44	4	65.48	flow
45	4	61.70	flow
46	4	58.24	flow
47	4	52.33	flow
48	4	50.06	flow
49	4	45.00	flow
50	4	42.77	flow
51	4	41.04	flow
52	4	33.91	flow
53	4	30.47	flow
54	4	30.33	flow
55	4	29.74	flow
56	4	23.63	flow
57	4	10.92	flow
58	4	10.68	flow
59	4	8.75	flow
60	4	6.79	flow
61	5	0.82	flow

62	5	2.42	flow
63	5	5.71	flow
64	5	7.80	flow
65	5	7.97	flow
66	5	11.31	flow
67	5	11.73	flow
68	5	12.84	flow
69	5	16.78	flow
70	5	28.07	flow
71	5	29.43	flow
72	5	41.47	flow
73	5	59.93	flow
74	5	60.72	flow
75	5	75.96	flow
76	5	66.12	flow
77	5	52.59	flow
78	5	47.49	flow
79	5	47.07	flow
80	5	31.48	flow
81	5	29.84	flow
82	5	29.45	flow
83	5	25.29	flow
84	5	18.65	flow
85	5	16.54	flow
86	5	10.81	flow
87	5	10.49	flow
88	5	10.48	flow
89	5	6.88	flow
90	5	1.19	flow
91	3	9.25	static
92	3	29.29	static
93	3	40.71	static
94	3	41.47	static
95	3	54.16	static
96	3	55.41	static
97	3	60.52	static
98	3	61.14	static
99	3	62.32	static
100	3	62.95	static
101	3	66.45	static
102	3	67.04	static
103	3	69.44	static
104	3	78.69	static
105	3	84.14	static
106	3	82.87	static
107	3	82.18	static

108	3	75.96	static
109	3	73.07	static
110	3	72.90	static
111	3	68.52	static
112	3	65.56	static
113	3	57.65	static
114	3	51.75	static
115	3	51.34	static
116	3	34.99	static
117	3	32.35	static
118	3	27.05	static
119	3	16.04	static
120	3	1.01	static
121	4	18.31	static
122	4	18.43	static
123	4	30.12	static
124	4	62.97	static
125	4	65.83	static
126	4	84.19	static
127	4	87.11	static
128	4	85.29	static
129	4	83.56	static
130	4	77.47	static
131	4	75.72	static
132	4	74.58	static
133	4	73.81	static
134	4	73.77	static
135	4	69.90	static
136	4	68.44	static
137	4	66.67	static
138	4	66.37	static
139	4	61.39	static
140	4	53.47	static
141	4	53.43	static
142	4	51.34	static
143	4	33.69	static
144	4	30.87	static
145	4	25.71	static
146	4	23.26	static
147	4	22.11	static
148	4	14.21	static
149	4	8.67	static
150	4	8.62	static
151	5	6.58	static
152	5	11.80	static
153	5	14.04	static

154 5 24.13 static
155 5 58.24 static
156 5 58.52 static
157 5 65.45 static
158 5 66.80 static
159 5 69.59 static
160 5 70.62 static
161 5 70.97 static
162 5 75.00 static
163 5 76.41 static
164 5 86.12 static
165 5 83.75 static
166 5 83.02 static
167 5 82.61 static
168 5 80.67 static
169 5 74.85 static
170 5 74.27 static
171 5 68.90 static
172 5 67.62 static
173 5 67.38 static
174 5 59.59 static
175 5 50.75 static
176 5 35.68 static
177 5 27.30 static
178 5 18.43 static
179 5 7.21 static
180 5 1.68 static

Welch Two Sample t-test
data: flow5 and static5
t = -4.539, df = 54.774, p-value = 3.136e-05
alternative hypothesis: true difference in means is not equal to 0
95 percent confidence interval:
-41.35593 -16.02074
sample estimates:
mean of x mean of y
25.91100 54.59933

> static5=c(6.58,+ 11.8,+ 14.04,+ 24.13,+ 58.24,+ 58.52,+ 65.45,+ 66.8,+ 69.59,+ 70.62,+ 70.97,+ 75,+ 76.41,+ 86.12,+ 83.75,+ 83.02,+ 82.61,+ 80.67,+ 74.85,+ 74.27,+ 68.9,+ 67.62,+ 67.38,+ 59.59,+ 50.75,+ 35.68,+ 27.3,+ 18.43,+ 7.21,+ 1.68);
> flow5=c(0.82,+ 2.42,+ 5.71,+ 7.8,+ 7.97,+ 11.31,+ 11.73,+ 12.84,+ 16.78,+ 28.07,+ 29.43,+ 41.47,+ 59.93,+ 60.72,+ 75.96,+ 66.12,+ 52.59,+ 47.49,+ 47.07,+ 31.48,+ 29.84,+ 29.45,+ 25.29,+ 18.65,+ 16.54,+ 10.81,+ 10.49,+ 10.48,+ 6.88,+ 1.19);
data: flow4 and static4
t = -2.9933, df = 57.662, p-value = 0.004059

alternative hypothesis: true difference in means is not equal to 0
95 percent confidence interval:
 -32.298437 -6.409563
sample estimates:
mean of x mean of y
 32.95633 52.31033

> flow4=c(0,+ 1.26,+ 4.5,+ 6.84,+ 10.51,+ 12.76,+ 17.88,+ 18.14,+ 29.93,+ 65.73,+ 79.7,+ 71.82,+ 67.78,+ 65.48,+ 61.7,+ 58.24,+ 52.33,+ 50.06,+ 45,+ 42.77,+ 41.04+ 33.91,+ 30.47,+ 30.33,+ 29.74,+ 23.63,+ 10.92,+ 10.68,+ 8.75,+ 6.79);

> static4=c(18.31,+ 18.43,+ 30.12,+ 62.97,+ 65.83,+ 84.19,+ 87.11,+ 85.29,+ 83.56,+ 77.47,+ 75.72,+ 74.58,+ 73.81,+ 73.77,+ 69.9,+ 68.44,+ 66.67,+ 66.37,+ 61.39,+ 53.47,+ 53.43,+ 51.34,+ 33.69,+ 30.87,+ 25.71,+ 23.26,+ 22.11,+ 14.21,+ 8.67,+ 8.62);

data: flow3 and static3
t = -1.214, df = 54.68, p-value = 0.23
alternative hypothesis: true difference in means is not equal to 0
95 percent confidence interval:
 -21.233966   5.214633
sample estimates:
mean of x mean of y
 46.53100 54.54067

> static3=c(9.25,+ 29.29,+ 40.71,+ 41.47,+ 54.16,+ 55.41,+ 60.52,+ 61.14,+ 62.32,+ 62.95,+ 66.45,+ 67.04,+ 69.44,+78.69,+ 84.14,+ 82.87,+ 82.18,+ 75.96,+ 73.07,+ 72.9,+ 68.52,+ 65.56,+ 57.65,+ 51.75,+ 51.34,+ 34.99,+ 32.35,+ 27.05,+ 16.04,+ 1.01);

> flow3=c(1.17,+ 7.7,+ 8.53,+ 15.04,+ 15.78,+ 50.11,+ 53.39,+ 58.34,+ 66.97,+ 75.53,+ 77.99,+ 82.57,+ 83.35,+ 86.01,+ 82.69,+ 82.61,+ 75,+ 72.53,+ 71.57,+ 52.13,+ 46.79,+ 45,+ 40.43,+ 30.78,+ 28.81,+ 25.02,+ 22.83,+ 21.54,+ 8.13,+ 7.59);

Disruption of 3D microvessel alignment, Figure 3.
Welch Two Sample t-test

data: flow5 and cd44kd
t = -2.285, df = 57.14, p-value = 0.02604
alternative hypothesis: true difference in means is not equal to 0
95 percent confidence interval:
 -25.176711 -1.659956
sample estimates:
mean of x mean of y
 25.91100 39.32933

> flow5=c(0.82,+ 2.42,+ 5.71,+ 7.8,+ 7.97,+ 11.31,+ 11.73,+ 12.84,+ 16.78,+ 28.07,+ 29.43,+ 41.47,+ 59.93,+ 60.72,+ 75.96,+ 66.12,+ 52.59,+ 47.49,+ 47.07,+ 31.48,+

29.84,+ 29.45,+ 25.29,+ 18.65,+ 16.54,+ 10.81,+ 10.49,+ 10.48,+ 6.88,+ 1.19);
> cd44kd=c(8.97,+ 11,+ 12.84,+ 15.95,+ 15.95,+ 16.91,+ 21.25,+ 37.64,+ 48.74,+
52.35,+ 74.52,+ 75.38,+ 78.96,+ 84.19,+ 73.12,+ 70.56,+ 70.29,+ 60.95,+ 46.22,+
38.96,+ 35.42,+ 34.82,+ 32.92,+ 30.83,+ 30.82,+ 30.67,+ 25.56,+ 25.2,+ 14.32,+ 4.57);
> t.test(flow5,cd44kd)

data: static and cd44kd
t = 2.2974, df = 57.126, p-value = 0.02528
alternative hypothesis: true difference in means is not equal to 0
95 percent confidence interval:
  1.960858 28.579142
sample estimates:
mean of x mean of y
 54.59933 39.32933

> static=c(6.58,+ 11.8,+ 14.04,+ 24.13,+ 58.24,+ 58.52,+ 65.45,+ 66.8,+ 69.59,+ 70.62,+
70.97,+ 75,+ 76.41,+ 86.12,+ 83.75,+ 83.02,+ 82.61,+ 80.67,+ 74.85,+ 74.27,+68.9,+
67.62,+ 67.38,+ 59.59,+ 50.75,+ 35.68,+ 27.3,+ 18.43,+ 7.21,+ 1.68);
> static(6.58,+ 11.8,+ 14.04,+ 24.13,+ 58.24, + 58.52,+ 65.45,+ 66.8,+ 69.59,+ 70.62,+
70.97,+ 75,+ 76.41,+ 86.12,+ 83.75,+ 83.02,+ 82.61,+ 80.67,+ 74.85,+ 74.27,+ 68.9,+
67.62,+ 67.38,+ 59.59,+ 50.75,+ 35.68,+ 27.3,+ 18.43,+ 7.21,+ 1.68);
> t.test(static,cd44kd)

data: flow5 and blebbi5
t = -5.0289, df = 56.931, p-value = 5.237e-06
alternative hypothesis: true difference in means is not equal to 0
95 percent confidence interval:
 -41.63198 -17.91868
sample estimates:
mean of x mean of y
 25.91100 55.68633

> flow5
 [1] 0.82 2.42 5.71 7.80 7.97 11.31 11.73 12.84 16.78 28.07 29.43 41.47
[13] 59.93 60.72 75.96 66.12 52.59 47.49 47.07 31.48 29.84 29.45 25.29 18.65
[25] 16.54 10.81 10.49 10.48 6.88 1.19
> blebbi5
 [1] 1.51 18.27 19.60 32.86 34.57 38.78 39.05 59.42 66.32 77.29 81.03 81.25
[13] 85.91 87.17 87.99 79.89 79.57 68.84 67.57 66.95 66.61 63.43 62.18 61.56
[25] 59.30 57.93 52.29 36.47 31.05 5.93
> t.test(flow5,blebbi5)

Microvessel morphology (length and diameter) with cd44KD and blebbistatin, Figure 3.

Welch Two Sample t-test

data: cd44kd_length and normal_flow_day5
t = -0.67203, df = 26.453, p-value = 0.5074
alternative hypothesis: true difference in means is not equal to 0
95 percent confidence interval:
 -50.75598 25.72931
sample estimates:
mean of x mean of y
 192.7540 205.2673

> cd44kd_length=c(286.29,+ 120.33,+ 151.44,+ 140,+ 177.87,+ 241.29,+ 185.26,+
218.81,+ 210.97,+ 170.19,+ 319.19,+ 143.78,+ 207.45,+ 188.57,+ 129.87);
> normal_flow_day5=c(227.58,+ 223.98,+ 187.74,+ 303.96,+ 141.46,+ 275.19,+
260.27,+ 189.44,+ 195.16,+ 169.04,+ 180.5,+ 189.7,+ 181.56,+ 175.05,+ 178.38);
> t.test(cd44kd_length, normal_flow_day5)

Welch Two Sample t-test
data: blebbi_length and normal_flow_day5
t = -1.0545, df = 27.368, p-value = 0.3009
alternative hypothesis: true difference in means is not equal to 0
95 percent confidence interval:
 -46.90543 15.04543
sample estimates:
mean of x mean of y
 189.3373 205.2673

> blebbi_length=c(259.63,+ 160.65,+ 201.86,+ 159.49,+ 203.89,+ 148.26,+ 170.97,+
203.06,+ 254.9,+ 145.92,+ 193.46,+ 142.41,+ 237.77,+ 171.25,+ 186.54);
> t.test(blebbi_length, normal_flow_day5)

  Welch Two Sample t-test
data: inner_diameter_flow_day5 and inner_diameter_flow_cd44kd
t = 3.2911, df = 6.8257, p-value = 0.01377
alternative hypothesis: true difference in means is not equal to 0
95 percent confidence interval:
 1.182182 7.329818
sample estimates:
mean of x mean of y
12.046 7.790

> t.test(inner_diameter_flow_day5,inner_diameter_flow_blebbi)

    Welch Two Sample t-test
data: inner_diameter_flow_day5 and inner_diameter_flow_blebbi
t = 3.0094, df = 6.7407, p-value = 0.02059
alternative hypothesis: true difference in means is not equal to 0
95 percent confidence interval:
 0.8049063 6.9310937

```
sample estimates:
mean of x mean of y
12.046 8.178

> t.test(outer_diameter_flow_day5,outer_diameter_flow_cd44kd)

    Welch Two Sample t-test
data:  outer_diameter_flow_day5 and outer_diameter_flow_cd44kd
t = 1.8391, df = 7.976, p-value = 0.1033
alternative hypothesis: true difference in means is not equal to 0
95 percent confidence interval:
 -1.309931 11.601931
sample estimates:
mean of x mean of y
   23.174    18.028
> t.test(outer_diameter_flow_day5,outer_diameter_flow_blebbi)

    Welch Two Sample t-test
data:  outer_diameter_flow_day5 and outer_diameter_flow_blebbi
t = 2.7737, df = 5.8828, p-value = 0.03294
alternative hypothesis: true difference in means is not equal to 0
95 percent confidence interval:
  0.7155673 11.8884327
sample estimates:
mean of x mean of y
   23.174    16.872
> inner_diameter_flow_day5=c(12.91,+ 11.16,+ 15.64,+ 9.07,+ 11.45);
> outer_diameter_flow_day5=c(19.93,+ 17.57,+ 28.9,+ 23.51,+ 25.96);
> inner_diameter_flow_cd44kd=c(10.35,+ 6.52,+ 7.84,+ 7.72,+ 6.52);
> outer_diameter_flow_cd44kd=c(17.28,+ 18.1,+ 24.59,+ 17.64,+ 12.53);
> inner_diameter_flow_blebbi=c(6.04,+ 7.54,+ 9.34,+ 9.92,+ 8.05);
> outer_diameter_flow_blebbi=c(14.05,+ 19.57,+ 18.75,+ 16.41,+ 15.58);
> t.test(inner_diameter_flow_day5,inner_diameter_flow_cd44kd)
```

Blood-spinal cord barrier evaluation, Figure 4.

```
Welch Two Sample t-test
data:  flow and flow_thrombin
t = -3.1637, df = 4.0764, p-value = 0.03318
alternative hypothesis: true difference in means is not equal to 0
95 percent confidence interval:
 -9.620494e-07 -6.625415e-08
sample estimates:
   mean of x    mean of y
1.376378e-07 6.517896e-07
> t.test(static,static_thrombin)

    Welch Two Sample t-test
```

data: static and static_thrombin
t = -5.1365, df = 4.1657, p-value = 0.006097
alternative hypothesis: true difference in means is not equal to 0
95 percent confidence interval:
 -7.211556e-07 -2.202062e-07
sample estimates:
  mean of x   mean of y
7.621012e-08 5.468910e-07
> t.test(static,flow)

   Welch Two Sample t-test
data: static and flow
t = -2.996, df = 7.7242, p-value = 0.01788
alternative hypothesis: true difference in means is not equal to 0
95 percent confidence interval:
 -1.090038e-07 -1.385161e-08
sample estimates:
  mean of x   mean of y
7.621012e-08 1.376378e-07
> t.test(static_thrombin,flow_thrombin)

   Welch Two Sample t-test
data: static_thrombin and flow_thrombin
t = -0.56568, df = 6.2892, p-value = 0.5912
alternative hypothesis: true difference in means is not equal to 0
95 percent confidence interval:
 -5.536403e-07 3.438431e-07
sample estimates:
  mean of x   mean of y
5.468910e-07 6.517896e-07

> flow
[1] 1.25190e-07 1.79096e-07 1.05944e-07 1.71509e-07 1.06450e-07
> static
[1] 8.08847e-08 1.02585e-07 1.04185e-07 3.75464e-08 5.58495e-08
> flow_thrombin
[1] 3.40093e-07 4.79782e-07 5.46440e-07 6.20823e-07 1.27181e-06
> static_thrombin
[1] 8.31635e-07 4.66625e-07 5.34519e-07 6.21717e-07 2.79959e-07
> t.test(flow,flow_thrombin)

Patterned microvessels guide axons from NPCs in vitro, Figure 5.
   Welch Two Sample t-test
data: axon_normal_day4 and axon_cd44kd_endos_day4
t = -2.1742, df = 57.926, p-value = 0.03379

```
alternative hypothesis: true difference in means is not equal to 0
95 percent confidence interval:
 -26.633745  -1.099588
sample estimates:
mean of x mean of y
 32.28200  46.14867

> axon_normal_day4=c(2.73,+ 4.32,+ 6.77,+ 16.86,+ 26.57,+ 38.52,+ 46.97,+ 53.62,+
56.61,+ 67.17,+ 79.05,+ 75.43,+ 72.03,+ 64.59,+ 58.17,+ 49.94,+ 45,+ 43.49,+ 27.98,+
26.57,+ 23.81,+ 21.45,+ 16.56,+ 12.01,+ 9.66,+ 8.33,+ 5.08,+ 3.88,+ 3.5,+ 1.79);
> axon_cd44kd_endos_day4=c(1.4,+ 23.63,+ 26.57,+ 26.57,+ 28.44,+ 33.37,+ 40.73,+
50.19,+ 50.71,+ 56.31,+ 57.17,+ 67.69,+ 68.5,+ 71.57,+ 74.22,+ 75.65,+ 77.01,+ 84.29,+
82.65,+ 65.77,+ 57.43,+54.69,+ 53.53,+ 46.27,+32.01,+ 29.48,+ 24.3,+ 15.02,+ 5.71,+
3.58);
> t.test(axon_normal_day4,axon_cd44kd_endos_day4)

Welch Two Sample t-test
data:  vessel_normal_day4 and vessel_cd44kd_endos_day4
t = -3.0785, df = 57.441, p-value = 0.003187
alternative hypothesis: true difference in means is not equal to 0
95 percent confidence interval:
 -27.975752  -5.926914
sample estimates:
mean of x mean of y
 30.63900  47.59033
> t.test(vessel_normal_day4,axon_normal_day4)

    Welch Two Sample t-test
data:  vessel_normal_day4 and axon_normal_day4
t = -0.26752, df = 57.218, p-value = 0.79
alternative hypothesis: true difference in means is not equal to 0
95 percent confidence interval:
 -13.94045  10.65445
sample estimates:
mean of x mean of y
   30.639    32.282
> t.test(vessel_cd44kd_day4,axon_cd44kd_day4)
Error in t.test(vessel_cd44kd_day4, axon_cd44kd_day4) :
  object 'vessel_cd44kd_day4' not found
> t.test(vessel_cd44kd_endos_day4,axon_cd44kd_endos_day4)

    Welch Two Sample t-test
data:  vessel_cd44kd_endos_day4 and axon_cd44kd_endos_day4
t = 0.24991, df = 56.204, p-value = 0.8036
alternative hypothesis: true difference in means is not equal to 0
95 percent confidence interval:
```

-10.11339 12.99672
sample estimates:
mean of x mean of y
47.59033 46.14867
> t.test(axon_normal_day4,vessel_cd44kd_endos_day4)

Welch Two Sample t-test
data: axon_normal_day4 and vessel_cd44kd_endos_day4
t = -2.5977, df = 55.481, p-value = 0.012
alternative hypothesis: true difference in means is not equal to 0
95 percent confidence interval:
-27.116125 -3.500542
sample estimates:
mean of x mean of y
32.28200 47.59033
> t.test(axon_cd44kd_endos_day4,vessel_normal_day4)

Welch Two Sample t-test
data: axon_cd44kd_endos_day4 and vessel_normal_day4
t = 2.5754, df = 57.617, p-value = 0.0126
alternative hypothesis: true difference in means is not equal to 0
95 percent confidence interval:
3.452986 27.566348
sample estimates:
mean of x mean of y
46.14867 30.63900

> vessel_normal_day4=c(2.29,+ 4.18,+ 10.18,+ 12.53,+ 13.45,+ 14.74,+ 22.48,+ 25.14,+ 33.98,+ 40.86,+ 43.36,+ 50.49,+ 56.04,+ 60.4,+ 62.35,+ 64.59,+ 70.87,+ 64.86,+ 57.26,+ 49.64,+ 38.9,+ 24.84,+ 24.26,+ 20.97,+ 19.89,+ 8.7,+ 6.91,+ 6.77,+ 5.27,+ 2.97);
> vessel_cd44kd_endos_day4=c(9.62,+ 13.71,+ 33.69,+ 35.06,+ 44.09,+ 45.73,+ 46.17,+ 48.62,+ 54.04,+ 61.39,+ 62.78,+ 63.43,+ 65.3,+ 71.86,+ 80.75,+ 75.41,+ 72.72,+ 68.2,+ 66.19,+ 56.31,+ 50.31,+ 48.24,+ 45,+ 43.36, + 43.21,+ 39.96,+ 36.35,+ 35.34,+ 8.67,+ 2.2);
> t.test(vessel_normal_day4,vessel_cd44kd_endos_day4)

Axon guidance at the site of a cervical spinal cord injury in a rat model, Figure 6.
Welch Two Sample t-test
data: invivo_flow_axon and in_vivo_static_axon
t = -6.0087, df = 47.766, p-value = 2.472e-07
alternative hypothesis: true difference in means is not equal to 0
95 percent confidence interval:
-40.38174 -20.13065
sample estimates:
mean of x mean of y
16.98733 47.24352

```
> invivo_flow_axon=c(37.21644,+ 33.02387,+ 27.8241,+ 23.83874,+ 19.61209,+
18.85316,+ 11.41584,+ 11.15466,+ 9.88141,+ 9.14164,+ 4.48461,+ 4.12759,+ 3.11084,+
0,+ 0,+ 1.59114,+ 2.77022,+ 4.01418,+ 4.8739,+ 7.6668,+ 8.1301,+ 8.55556,+
14.42077,+ 19.62226,+ 22.29363,+ 36.93876,+ 38.11828,+ 39.38242,+ 43.2643,+
44.29268);
> in_vivo_static_axon=c(18.43495,+ 35.78897,+ 37.79394,+ 59.53446,+ 60.75117,+
89.1186,+ 41.2686,+ 78.69007,+ 81.8699,+ 58.57043,+ 31.13897,+ 45,+ 86.82017,+
57.72436,+ 41.18593,+ 26.56505,+ 81.8699,+ 0,+ 61.38954,+ 28.07249,+ 33.11134,+
50.90614,+ 57.99462,+ 21.25051,+ 23.62938,+ 19.13364,+ 21.16126,+ 47.29061,+
39.98689,+ 81.25384);
> t.test(in_vivo_flow_axon,in_vivo_static_axon)

Welch Two Sample t-test
data:  flow_vessel and static_vessel
t = -10.229, df = 41.285, p-value = 6.941e-13
alternative hypothesis: true difference in means is not equal to 0
95 percent confidence interval:
 -50.31503 -33.72579
sample estimates:
mean of x mean of y
 12.66244  54.68285

> flow_vessel=c(45.90938,+ 14.18429,+ 14.12792,+ 12.69958,+ 12.45,+ 10.70401,+
9.94429,+ 7.12502,+ 5.23748,+ 3.49464,+ 1.28733,+ 2.15296,+ 2.31372,+ 3.81407,+
5.77433,+ 6.24837,+ 7.37377,+ 7.76517,+ 8.65872,+ 9.40634,+ 11.30993,+ 14.24561,+
14.26451,+ 15.11347,+ 15.56151,+ 16.32096,+ 21.50143,+ 21.67465,+ 26.56505,+
32.64464);
> static_vessel=c(4.26789,+ 37.77568,+ 41.46771,+ 61.07357,+ 68.83874,+ 37.13092,+
14.42077,+ 15.42216,+ 60.25512,+ 40.46223,+ 41.78452,+ 55.71312,+ 42.51045,+
48.81407,+ 76.2729,+ 77.074,+ 69.67686,+ 41.46771,+ 43.61128,+ 64.59228,+
62.44719,+ 75.83783,+ 67.54306,+ 50.09212,+ 61.049,+ 80.04937,+ 69.56717,+
80.53768,+ 76.67547,+ 74.0546);
> t.test(flow_vessel,static_vessel)

Welch Two Sample t-test
data:  axon_day4_in_vitro and axon_in_vivo
t = 2.8969, df = 45.975, p-value = 0.005753
alternative hypothesis: true difference in means is not equal to 0
95 percent confidence interval:
  4.667277 25.922057
sample estimates:
mean of x mean of y
 32.28200  16.98733

> axon_day4_in_vitro = c(2.73,+ 4.32,+ 6.77,+ 16.86,+ 26.57,+ 38.52,+ 46.97,+ 53.62,+
```

56.61,+ 67.17,+ 79.05,+ 75.43,+ 72.03,+ 64.59,+ 58.17,+ 49.94,+ 45,+ 43.49,+ 27.98,+ 26.57,+ 23.81,+ 21.45,+ 16.56,+ 12.01,+ 9.66,+ 8.33,+ 5.08,+ 3.88,+ 3.5,+ 1.79);
> axon_in_vivo=c(37.21644,+ 33.02387,+ 27.8241,+23.83874,+ 19.61209,+ 18.85316,+ 11.41584,+ 11.15466,+ 9.88141,+ 9.14164,+ 4.48461,+ 4.12759,+ 3.11084,+ 0,+ 0,+ 1.59114,+ 2.77022,+ 4.01418,+ 4.8739,+ 7.6668,+ 8.1301,+ 8.55556,+ 14.42077,+ 19.62226,+ 22.29363,+ 36.93876,+ 38.11828,+ 39.38242,+ 43.2643,+ 44.29268);
> t.test(axon_day4_in_vitro,axon_in_vivo)

  Welch Two Sample t-test
data: vessel_in_vitro_day4 and vessel_in_vivo
t = 4.2905, df = 37.994, p-value = 0.0001182
alternative hypothesis: true difference in means is not equal to 0
95 percent confidence interval:
 10.71856 29.86923
sample estimates:
mean of x mean of y
 32.95633 12.66244

> vessel_in_vitro_day4=c(0,+ 1.26,+ 4.5,+ 6.84,+ 10.51,+ 12.76,+ 17.88,+ 18.14,+ 29.93,+ 65.73,+ 79.7,+ 71.82,+ 67.78,+ 65.48,+ 61.7,+ 58.24,+ 52.33,+ 50.06,+ 45,+ 42.77,+ 41.04,+ 33.91,+ 30.47,+ 30.33,+ 29.74,+ 23.63,+ 10.92,+ 10.68,+ 8.75,+ 6.79);
> vessel_in_vivo=c(45.90938,+ 14.18429,+ 14.12792,+ 12.69958,+ 12.45,+ 10.70401,+ 9.94429,+ 7.12502,+ 5.23748,+ 3.49464,+ 1.28733,+ 2.15296,+ 2.31372,+ 3.81407,+ 5.77433,+ 6.24837,+ 7.37377,+ 7.76517,+ 8.65872,+ 9.40634,+ 11.30993,+ 14.24561,+ 14.26451,+ 15.11347,+ 15.56151,+ 16.32096,+ 21.50143,+ 21.67465,+ 26.56505,+ 32.64464);
> t.test(vessel_in_vitro_day4,vessel_in_vivo)

Welch Two Sample t-test
data: vessel_in_vitro_day5 and vessel_in_vivo
t = 3.1059, df = 40.302, p-value = 0.003467
alternative hypothesis: true difference in means is not equal to 0
95 percent confidence interval:
  4.629496 21.867627
sample estimates:
mean of x mean of y
 25.91100 12.66244
> vessel_in_vitro_day5=c(0.82,+ 2.42,+ 5.71,+ 7.8,+ 7.97,+ 11.31,+ 11.73,+ 12.84,+ 16.78,+ 28.07,+ 29.43,+ 41.47,+ 59.93,+ 60.72,+ 75.96,+ 66.12,+ 52.59,+ 47.49,+ 47.07,+ 31.48,+ 29.84,+ 29.45,+ 25.29,+ 18.65,+ 16.54,+ 10.81,+ 10.49,+ 10.48,+ 6.88,+ 1.19);
> t.test(vessel_in_vitro_day5,vessel_in_vivo)

    Welch Two Sample t-test
data: vessel_in_vitro_day4_npc and vessel_in_vivo
t = 4.0477, df = 39.336, p-value = 0.000235

alternative hypothesis: true difference in means is not equal to 0
95 percent confidence interval:
 8.995828 26.957296
sample estimates:
mean of x mean of y
 30.63900 12.66244
> vessel_in_vitro_day4_npc=c(2.29,+ 4.18,+ 10.18,+ 12.53,+ 13.45,+ 14.74,+ 22.48,+
25.14,+ 33.98,+ 40.86,+ 43.36,+ 50.49,+ 56.04,+ 60.4,+ 62.35,+ 64.59,+ 70.87,+ 64.86,+
57.26,+ 49.64,+ 38.9,+ 24.84,+ 24.26,+ 20.97,+ 19.89,+ 8.7,+ 6.91,+ 6.77,+ 5.27,+ 2.97);
> t.test(vessel_in_vitro_day4_npc,vessel_in_vivo)

Welch Two Sample t-test
data: normal_axon_in_vitro and axon_length_in_vivo
t = -1.2153, df = 16.334, p-value = 0.2415
alternative hypothesis: true difference in means is not equal to 0
95 percent confidence interval:
-60.47740 16.35663
sample estimates:
mean of x mean of y
 99.5960 121.6564

> normal_axon_in_vitro=c(113.58,+ 117.46,+ 101.98,+ 113.96,+ 112.78,+ 87.44,+
110.58,+ 92.15,+ 117.05,+ 108.42,+ 127.12,+ 63.33,+ 73.17,+ 77.76,+ 77.16);
> axon_length_in_vivo=c(75.15053,+ 48.05646,+ 103.08753,+ 81.8234,+ 24.62524,+
185.97821,+ 102.93442,+ 57.11978,+ 137.88595,+ 98.19611,+ 132.03597,+ 151.50298,+
122.48865,+ 267.41035,+ 236.55022);
> t.test(normal_axon_in_vitro,axon_length_in_vivo)

Welch Two Sample t-test
data: vessel_length_in_vivo and vessel_length_in_vitro
t = 0.72026, df = 17.1, p-value = 0.4811
alternative hypothesis: true difference in means is not equal to 0
95 percent confidence interval:
 -50.14213 102.15895
sample estimates:
mean of x mean of y
 231.2757 205.2673

> vessel_length_in_vivo=c(183.43858,+ 245.95282,+ 324.24421,+ 298.06018,+
189.91221,+ 180.08805,+ 172.31286,+ 629.94416,+ 136.02003,+ 241.58005,+
129.98668,+ 85.7776,+ 177.12794,+ 136.71766,+ 337.97308);
> vessel_length_in_vitro=c(227.58,+ 223.98,+ 187.74,+ 303.96,+ 141.46,+ 275.19,+
260.27,+ 189.44,+ 195.16,+ 169.04,+ 180.5,+ 189.7,+ 181.56,+ 175.05,+ 178.38);
> t.test(vessel_length_in_vivo,vessel_length_in_vitro)

In vivo axon length

```
  Welch Two Sample t-test
data:  flow and static
t = 1.6815, df = 17.478, p-value = 0.1105
alternative hypothesis: true difference in means is not equal to 0
95 percent confidence interval:
 -7.844432 70.066879
sample estimates:
mean of x mean of y
121.65639  90.54516
> static=c(83.51869,+ 119.90822,+ 45.35704,+ 84.81279,+ 131.05412,+ 111.26442,+
110.76253,+ 99.57501,+ 82.76707,+ 75.90865,+ 57.51771,+ 81.32716,+ 94.49719,+
67.1405,+ 112.76635);
> flow=c(75.15053,+ 48.05646,+ 103.08753,+ 81.8234,+ 24.62524,+ 185.97821,+
102.93442,+ 57.11978,+ 137.88595,+ 98.19611,+ 132.03597,+ 151.50298,+ 122.48865,+
267.41035,+ 236.55022);
> t.test(flow,static)
```

In vivo vessel length

```
   Welch Two Sample t-test
data:  static and flow
t = -2.0672, df = 18.958, p-value = 0.05264
alternative hypothesis: true difference in means is not equal to 0
95 percent confidence interval:
 -154.9505575    0.9733735
sample estimates:
mean of x mean of y
 154.2871  231.2757

> static=c(312.65275,+ 153.41949,+ 107.27793,+ 116.8337,+ 132.59189,+ 180.65504,+
184.36825,+ 176.88336,+ 121.08529,+ 108.60705,+ 121.63878,+ 115.50796,+
93.12643,+ 217.16847,+ 172.49084);
> flow=c(183.43858,+ 245.95282,+ 324.24421,+ 298.06018,+ 189.91221,+ 180.08805,+
172.31286,+ 629.94416,+ 136.02003,+ 241.58005,+ 129.98668,+ 85.7776,+ 177.12794,+
136.71766,+ 337.97308);
> t.test(static, flow)
```

6.2.3 Microvessels within peptide transplants increase host axon infiltration.

Tuj-positive axon infiltration statistics.

Welch Two Sample t-test

```
> t.test(tuj_acellular,tuj_high_density)

   Welch Two Sample t-test
```

data: tuj_acellular and tuj_high_density

t = -8.5585, df = 9.0656, p-value = 1.228e-05

alternative hypothesis: true difference in means is not equal to 0

95 percent confidence interval:

 -2677.205 -1558.795

sample estimates:

mean of x mean of y

1312 3430

> t.test(tuj_acellular,tuj_low_density)

    Welch Two Sample t-test

data: tuj_acellular and tuj_low_density

t = -2.1203, df = 7.2676, p-value = 0.07024

alternative hypothesis: true difference in means is not equal to 0

95 percent confidence interval:

 -1464.67415   74.34082

sample estimates:

mean of x mean of y

 1312.000 2007.167

> t.test(tuj_high_density,tuj_low_density)

    Welch Two Sample t-test

data: tuj_high_density and tuj_low_density

t = 3.9902, df = 8.8317, p-value = 0.003279

alternative hypothesis: true difference in means is not equal to 0

95 percent confidence interval:

613.8364 2231.8303

sample estimates:

mean of x mean of y

3430.000 2007.167

tuj_acellular

[1] 1481 1775 1332 810 1479 995

> tuj_high_density

[1] 3415 3881 3120 3193 4138 2833

> tuj_low_density

[1] 2319 2820 2707 1203 1802 1192

5-HT serotonin axon infiltration statistics.

Welch Two Sample t-test

data: motor_axon_acellular and motor_axon_low_density

t = -7.7591, df = 9.8892, p-value = 1.641e-05

alternative hypothesis: true difference in means is not equal to 0

95 percent confidence interval:

-348.9404 -193.0596

sample estimates:

mean of x mean of y

322.6667 593.6667

> t.test(motor_axon_acellular, motor_axon_high_density)

Welch Two Sample t-test

data: motor_axon_acellular and motor_axon_high_density

t = -3.8196, df = 6.6586, p-value = 0.007195

alternative hypothesis: true difference in means is not equal to 0

95 percent confidence interval:

-174.47766 -40.18901

sample estimates:

mean of x mean of y

322.6667 430.0000

> t.test(motor_axon_low_density, motor_axon_high_density)

Welch Two Sample t-test

data: motor_axon_low_density and motor_axon_high_density

t = 6.3683, df = 7.021, p-value = 0.0003739

alternative hypothesis: true difference in means is not equal to 0

95 percent confidence interval:

102.9317 224.4016

sample estimates:

mean of x mean of y

593.6667 430.0000

> motor_axon_acellular

[1] 336 368 279 407 228 318

> motor_axon_low_density

[1] 628 620 656 547 608 503

> motor_axon_high_density

[1] 394 423 432 464 412 455

Neurovascular interactions statistics.

Welch Two Sample t-test

> neurovascular_inter_high_density=c(14,13);

> neurovascular_inter_low_density=c(6,9);

> t.test(neurovascular_inter_low_density,neurovascular_inter_high_density)

Welch Two Sample t-test

data: neurovascular_inter_low_density and neurovascular_inter_high_density

t = -3.7947, df = 1.2195, p-value = 0.1281

alternative hypothesis: true difference in means is not equal to 0

95 percent confidence interval:

-19.272109 7.272109

sample estimates:

mean of x mean of y

7.5 13.5

References

Abbott, N. J., Ronnback, L., & Hansson, E. (2006). Astrocyte-endothelial interactions at the blood-brain barrier. *Nat Rev Neurosci, 7*(1), 41-53. Retrieved from https://www.ncbi.nlm.nih.gov/pubmed/16371949. doi:10.1038/nrn1824

Acharya, N. K., Goldwaser, E. L., Forsberg, M. M., Godsey, G. A., Johnson, C. A., Sarkar, A., . . . Nagele, R. G. (2015). Sevoflurane and Isoflurane induce structural changes in brain vascular endothelial cells and increase blood-brain barrier permeability: Possible link to postoperative delirium and cognitive decline. *Brain Res, 1620*, 29-41. Retrieved from https://www.ncbi.nlm.nih.gov/pubmed/25960348. doi:10.1016/j.brainres.2015.04.054

Adamson, R. H., Lenz, J. F., & Curry, F. E. (1994). Quantitative Laser Scanning Confocal Microscopy on Single Capillaries: Permeability Measurement. *Microcirculation, 1*(4), 251-265. Retrieved from http://dx.doi.org/10.3109/10739689409146752. doi:10.3109/10739689409146752

Asher, R. A., Morgenstern, D. A., Fidler, P. S., Adcock, K. H., Oohira, A., Braistead, J. E., . . . Fawcett, J. W. (2000). Neurocan is upregulated in injured brain and in cytokine-treated astrocytes. *J Neurosci, 20*(7), 2427-2438. Retrieved from https://www.ncbi.nlm.nih.gov/pubmed/10729323.

Audus, K. L., & Borchardt, R. T. (1986). Characterization of an in vitro blood-brain barrier model system for studying drug transport and metabolism. *Pharm Res, 3*(2), 81-87. Retrieved from https://www.ncbi.nlm.nih.gov/pubmed/24271465. doi:10.1023/A:1016337202335

Bade, N. D., Kamien, R. D., Assoian, R. K., & Stebe, K. J. (2017). Curvature and Rho activation differentially control the alignment of cells and stress fibers. *Sci Adv, 3*(9), e1700150. Retrieved from https://www.ncbi.nlm.nih.gov/pubmed/28913421. doi:10.1126/sciadv.1700150

Bagley, A. F., Scherz-Shouval, R., Galie, P. A., Zhang, A. Q., Wyckoff, J., Whitesell, L., . . . Bhatia, S. N. (2015). Endothelial Thermotolerance Impairs Nanoparticle Transport in Tumors. *Cancer Res, 75*(16), 3255-3267. Retrieved from https://www.ncbi.nlm.nih.gov/pubmed/26122846. doi:10.1158/0008-5472.CAN-15-0325

Bakshi, A., Fisher, O., Dagci, T., Himes, B. T., Fischer, I., & Lowman, A. (2004). Mechanically engineered hydrogel scaffolds for axonal growth and angiogenesis after transplantation in spinal cord injury. *J Neurosurg Spine, 1*(3), 322-329. Retrieved from https://www.ncbi.nlm.nih.gov/pubmed/15478371. doi:10.3171/spi.2004.1.3.0322

Bartanusz, V., Jezova, D., Alajajian, B., & Digicaylioglu, M. (2011). The blood-spinal cord barrier: morphology and clinical implications. *Ann Neurol, 70*(2), 194-206. Retrieved from https://www.ncbi.nlm.nih.gov/pubmed/21674586
http://onlinelibrary.wiley.com/store/10.1002/ana.22421/asset/22421_ftp.pdf?v=1&t=j2jg9g43&s=338d6bed8374003b2eba7ab9cbe6b76dbea4ec01. doi:10.1002/ana.22421

Bartanusz, V., Jezova, D., Alajajian, B., & Digicaylioglu, M. (2011). The blood–spinal cord barrier: morphology and clinical implications. *Annals of neurology, 70*(2), 194-206.

Basso, D. M., Beattie, M. S., & Bresnahan, J. C. (1995). A sensitive and reliable locomotor rating scale for open field testing in rats. *J Neurotrauma, 12*(1), 1-21. Retrieved from https://www.ncbi.nlm.nih.gov/pubmed/7783230. doi:10.1089/neu.1995.12.1

Bell, R. D., & Zlokovic, B. V. (2009). Neurovascular mechanisms and blood-brain barrier disorder in Alzheimer's disease. *Acta Neuropathol, 118*(1), 103-113. Retrieved from https://www.ncbi.nlm.nih.gov/pubmed/19319544. doi:10.1007/s00401-009-0522-3

Benson, K., Cramer, S., & Galla, H. J. (2013). Impedance-based cell monitoring: barrier properties and beyond. *Fluids Barriers CNS, 10*(1), 5. Retrieved from https://www.ncbi.nlm.nih.gov/pubmed/23305242. doi:10.1186/2045-8118-10-5

Bergers, G., & Song, S. (2005). The role of pericytes in blood-vessel formation and maintenance. *Neuro Oncol, 7*(4), 452-464. Retrieved from https://www.ncbi.nlm.nih.gov/pubmed/16212810. doi:10.1215/S1152851705000232

Bomstein, Y., Marder, J. B., Vitner, K., Smirnov, I., Lisaey, G., Butovsky, O., . . . Yoles, E. (2003). Features of skin-coincubated macrophages that promote recovery from spinal cord injury. *J Neuroimmunol, 142*(1-2), 10-16. Retrieved from https://www.ncbi.nlm.nih.gov/pubmed/14512160.

Bonner, J. F., Connors, T. M., Silverman, W. F., Kowalski, D. P., Lemay, M. A., & Fischer, I. (2011). Grafted neural progenitors integrate and restore synaptic connectivity across the injured spinal cord. *J Neurosci, 31*(12), 4675-4686. Retrieved from https://www.ncbi.nlm.nih.gov/pubmed/21430166. doi:10.1523/JNEUROSCI.4130-10.2011

Booth, R., & Kim, H. (2012). Characterization of a microfluidic in vitro model of the blood-brain barrier (muBBB). *Lab Chip, 12*(10), 1784-1792. Retrieved from https://www.ncbi.nlm.nih.gov/pubmed/22422217. doi:10.1039/c2lc40094d

Bracken, M. B., Shepard, M. J., Collins, W. F., Holford, T. R., Young, W., Baskin, D. S., . . . et al. (1990). A randomized, controlled trial of methylprednisolone or naloxone in the treatment of acute spinal-cord injury. Results of the Second National Acute Spinal Cord Injury Study. *N Engl J Med, 322*(20), 1405-1411. Retrieved from https://www.ncbi.nlm.nih.gov/pubmed/2278545. doi:10.1056/NEJM199005173222001

Bracken, M. B., Shepard, M. J., Holford, T. R., Leo-Summers, L., Aldrich, E. F., Fazl, M., . . . Young, W. (1997). Administration of methylprednisolone for 24 or 48 hours or tirilazad mesylate for 48 hours in the treatment of acute spinal cord injury. Results of the Third National Acute Spinal Cord Injury Randomized Controlled Trial. National Acute Spinal Cord Injury Study. *JAMA, 277*(20), 1597-1604. Retrieved from https://www.ncbi.nlm.nih.gov/pubmed/9168289.

Bradbury, E. J., & Carter, L. M. (2011). Manipulating the glial scar: chondroitinase ABC as a therapy for spinal cord injury. *Brain research bulletin, 84*(4-5), 306-316.

Bunge, R. P. (1993). Expanding roles for the Schwann cell: ensheathment, myelination, trophism and regeneration. *Curr Opin Neurobiol, 3*(5), 805-809. Retrieved from https://www.ncbi.nlm.nih.gov/pubmed/8260833.

Butcher, J. T., Penrod, A. M., Garcia, A. J., & Nerem, R. M. (2004). Unique morphology and focal adhesion development of valvular endothelial cells in static and fluid flow environments. *Arterioscler Thromb Vasc Biol, 24*(8), 1429-1434. Retrieved from https://www.ncbi.nlm.nih.gov/pubmed/15117733. doi:10.1161/01.ATV.0000130462.50769.5a

Cai, D., Qiu, J., Cao, Z., McAtee, M., Bregman, B. S., & Filbin, M. T. (2001). Neuronal cyclic AMP controls the developmental loss in ability of axons to regenerate. *J Neurosci, 21*(13), 4731-4739. Retrieved from https://www.ncbi.nlm.nih.gov/pubmed/11425900.

Cao, Y., Chen, Y., & DeVivo, M. (2011). Lifetime direct costs after spinal cord injury. *Topics in Spinal Cord Injury Rehabilitation, 16*(4), 10-16.

Chauvet, N., Prieto, M., & Alonso, G. (1998). Tanycytes present in the adult rat mediobasal hypothalamus support the regeneration of monoaminergic axons. *Exp Neurol, 151*(1), 1-13. Retrieved from https://www.ncbi.nlm.nih.gov/pubmed/9582250. doi:10.1006/exnr.1998.6784

Cho, H., Seo, J. H., Wong, K. H., Terasaki, Y., Park, J., Bong, K., . . . Irimia, D. (2015). Three-Dimensional Blood-Brain Barrier Model for in vitro Studies of Neurovascular Pathology. *Sci Rep, 5*, 15222. Retrieved from https://www.ncbi.nlm.nih.gov/pubmed/26503597. doi:10.1038/srep15222

Chrobak, K. M., Potter, D. R., & Tien, J. (2006). Formation of perfused, functional microvascular tubes in vitro. *Microvasc Res, 71*(3), 185-196. Retrieved from https://www.ncbi.nlm.nih.gov/pubmed/16600313. doi:10.1016/j.mvr.2006.02.005

Clifford, P. M., Siu, G., Kosciuk, M., Levin, E. C., Venkataraman, V., D'Andrea, M. R., & Nagele, R. G. (2008). Alpha7 nicotinic acetylcholine receptor expression by vascular smooth muscle cells facilitates the deposition of Abeta peptides and promotes cerebrovascular amyloid angiopathy. *Brain Res, 1234*, 158-171. Retrieved from https://www.ncbi.nlm.nih.gov/pubmed/18708033. doi:10.1016/j.brainres.2008.07.092

Cucullo, L., Hossain, M., Puvenna, V., Marchi, N., & Janigro, D. (2011). The role of shear stress in Blood-Brain Barrier endothelial physiology. *BMC Neurosci, 12*, 40. Retrieved from https://www.ncbi.nlm.nih.gov/pubmed/21569296. doi:10.1186/1471-2202-12-40

Cucullo, L., Marchi, N., Hossain, M., & Janigro, D. (2011). A dynamic in vitro BBB model for the study of immune cell trafficking into the central nervous system. *J Cereb Blood Flow Metab, 31*(2), 767-777. Retrieved from https://www.ncbi.nlm.nih.gov/pubmed/20842162. doi:10.1038/jcbfm.2010.162

Cucullo, L., McAllister, M. S., Kight, K., Krizanac-Bengez, L., Marroni, M., Mayberg, M. R., . . . Janigro, D. (2002). A new dynamic in vitro model for the multidimensional study of astrocyte-endothelial cell interactions at the blood-brain barrier. *Brain Res, 951*(2), 243-254. Retrieved from https://www.ncbi.nlm.nih.gov/pubmed/12270503.

Cummings, B. J., Uchida, N., Tamaki, S. J., Salazar, D. L., Hooshmand, M., Summers, R., . . . Anderson, A. J. (2005). Human neural stem cells differentiate and promote locomotor recovery in spinal cord-injured mice. *Proc Natl Acad Sci U S A, 102*(39), 14069-14074. Retrieved from https://www.ncbi.nlm.nih.gov/pubmed/16172374. doi:10.1073/pnas.0507063102

Daneman, R., & Prat, A. (2015). The blood–brain barrier. *Cold Spring Harbor perspectives in biology, 7*(1), a020412.

David, S., & Aguayo, A. J. (1981). Axonal elongation into peripheral nervous system" bridges" after central nervous system injury in adult rats. *Science, 214*(4523), 931-933.

Dehouck, M. P., Meresse, S., Delorme, P., Fruchart, J. C., & Cecchelli, R. (1990). An easier, reproducible, and mass-production method to study the blood-brain barrier in vitro. *J Neurochem, 54*(5), 1798-1801. Retrieved from https://www.ncbi.nlm.nih.gov/pubmed/2182777.

del Zoppo, G. J. (2010). The neurovascular unit, matrix proteases, and innate inflammation. *Ann N Y Acad Sci, 1207*, 46-49. Retrieved from https://www.ncbi.nlm.nih.gov/pubmed/20955425. doi:10.1111/j.1749-6632.2010.05760.x

del Zoppo, G. J., & Hallenbeck, J. M. (2000). Advances in the vascular pathophysiology of ischemic stroke. *Thromb Res, 98*(3), 73-81. Retrieved from https://www.ncbi.nlm.nih.gov/pubmed/10812160.

Deosarkar, S. P., Prabhakarpandian, B., Wang, B., Sheffield, J. B., Krynska, B., & Kiani, M. F. (2015). A Novel Dynamic Neonatal Blood-Brain Barrier on a Chip. *PLoS One, 10*(11), e0142725. Retrieved from https://www.ncbi.nlm.nih.gov/pubmed/26555149. doi:10.1371/journal.pone.0142725

Dietz, V., Colombo, G., & Jensen, L. (1994). Locomotor activity in spinal man. *Lancet, 344*(8932), 1260-1263. Retrieved from https://www.ncbi.nlm.nih.gov/pubmed/7967986.

Dray, C., Rougon, G., & Debarbieux, F. (2009). Quantitative analysis by in vivo imaging of the dynamics of vascular and axonal networks in injured mouse spinal cord. *Proceedings of the National Academy of Sciences, 106*(23), 9459-9464. Retrieved from https://www.pnas.org/content/pnas/106/23/9459.full.pdf. doi:10.1073/pnas.0900222106

Dray, C., Rougon, G., & Debarbieux, F. (2009). Quantitative analysis by in vivo imaging of the dynamics of vascular and axonal networks in injured mouse spinal cord. *Proc Natl Acad Sci U S A, 106*(23), 9459-9464. Retrieved from https://www.ncbi.nlm.nih.gov/pubmed/19470644. doi:10.1073/pnas.0900222106

Ellis-Behnke, R. G., Liang, Y. X., You, S. W., Tay, D. K., Zhang, S., So, K. F., & Schneider, G. E. (2006). Nano neuro knitting: peptide nanofiber scaffold for brain repair and axon regeneration with functional return of vision. *Proc Natl Acad Sci U S A, 103*(13), 5054-5059. Retrieved from https://www.ncbi.nlm.nih.gov/pubmed/16549776. doi:10.1073/pnas.0600559103

Eng, L. F. (1985). Glial fibrillary acidic protein (GFAP): the major protein of glial intermediate filaments in differentiated astrocytes. *Journal of neuroimmunology, 8*, 203-214.

Evaniew, N., Noonan, V. K., Fallah, N., Kwon, B. K., Rivers, C. S., Ahn, H., . . . Network, R. (2015). Methylprednisolone for the Treatment of Patients with Acute Spinal Cord Injuries: A Propensity Score-Matched Cohort Study from a Canadian Multi-Center Spinal Cord Injury Registry. *J Neurotrauma, 32*(21), 1674-1683. Retrieved from https://www.ncbi.nlm.nih.gov/pubmed/26065706. doi:10.1089/neu.2015.3963

Fairless, R., & Barnett, S. C. (2005). Olfactory ensheathing cells: their role in central nervous system repair. *Int J Biochem Cell Biol, 37*(4), 693-699. Retrieved from https://www.ncbi.nlm.nih.gov/pubmed/15694828. doi:10.1016/j.biocel.2004.10.010

Fehlings, M. G., Vaccaro, A., Wilson, J. R., Singh, A., D, W. C., Harrop, J. S., . . . Rampersaud, R. (2012). Early versus delayed decompression for traumatic cervical spinal cord injury: results of the Surgical Timing in Acute Spinal Cord Injury Study (STASCIS). *PLoS One, 7*(2), e32037. Retrieved from https://www.ncbi.nlm.nih.gov/pubmed/22384132. doi:10.1371/journal.pone.0032037

Feron, F., Perry, C., Cochrane, J., Licina, P., Nowitzke, A., Urquhart, S., . . . Mackay-Sim, A. (2005). Autologous olfactory ensheathing cell transplantation in human spinal cord injury. *Brain, 128*(Pt 12), 2951-2960. Retrieved from https://www.ncbi.nlm.nih.gov/pubmed/16219671. doi:10.1093/brain/awh657

Fischer, S., Clauss, M., Wiesnet, M., Renz, D., Schaper, W., & Karliczek, G. F. (1999). Hypoxia induces permeability in brain microvessel endothelial cells via VEGF and NO. *Am J Physiol, 276*(4 Pt 1), C812-820. Retrieved from https://www.ncbi.nlm.nih.gov/pubmed/10199811.

Fischer, S., Wobben, M., Kleinstuck, J., Renz, D., & Schaper, W. (2000). Effect of astroglial cells on hypoxia-induced permeability in PBMEC cells. *Am J Physiol Cell Physiol, 279*(4), C935-944. Retrieved from https://www.ncbi.nlm.nih.gov/pubmed/11003573. doi:10.1152/ajpcell.2000.279.4.C935

Fitch, M. T., & Silver, J. (1997). Activated macrophages and the blood-brain barrier: inflammation after CNS injury leads to increases in putative inhibitory molecules. *Exp Neurol, 148*(2), 587-603. Retrieved from https://www.ncbi.nlm.nih.gov/pubmed/9417835. doi:10.1006/exnr.1997.6701

Fouad, K., Schnell, L., Bunge, M. B., Schwab, M. E., Liebscher, T., & Pearse, D. D. (2005). Combining Schwann cell bridges and olfactory-ensheathing glia grafts with chondroitinase promotes locomotor recovery after complete transection of the spinal cord. *J Neurosci, 25*(5), 1169-1178. Retrieved from https://www.ncbi.nlm.nih.gov/pubmed/15689553. doi:10.1523/JNEUROSCI.3562-04.2005

Friedli, L., Rosenzweig, E. S., Barraud, Q., Schubert, M., Dominici, N., Awai, L., . . . Courtine, G. (2015). Pronounced species divergence in corticospinal tract reorganization and functional recovery after lateralized spinal cord injury favors primates. *Sci Transl Med, 7*(302), 302ra134. Retrieved from https://www.ncbi.nlm.nih.gov/pubmed/26311729. doi:10.1126/scitranslmed.aac5811

Galie, P. A., Nguyen, D. H., Choi, C. K., Cohen, D. M., Janmey, P. A., & Chen, C. S. (2014). Fluid shear stress threshold regulates angiogenic sprouting. *Proc Natl Acad Sci U S A, 111*(22), 7968-7973. Retrieved from https://www.ncbi.nlm.nih.gov/pubmed/24843171. doi:10.1073/pnas.1310842111

Galie, P. A., & Stegemann, J. P. (2011). Simultaneous application of interstitial flow and cyclic mechanical strain to a three-dimensional cell-seeded hydrogel. *Tissue Eng Part C Methods, 17*(5), 527-536. Retrieved from https://www.ncbi.nlm.nih.gov/pubmed/21174633. doi:10.1089/ten.TEC.2010.0547

Galie, P. A., van Oosten, A., Chen, C. S., & Janmey, P. A. (2015). Application of multiple levels of fluid shear stress to endothelial cells plated on polyacrylamide gels. *Lab Chip, 15*(4), 1205-1212. Retrieved from https://www.ncbi.nlm.nih.gov/pubmed/25573790. doi:10.1039/c4lc01236d

Genove, E., Shen, C., Zhang, S., & Semino, C. E. (2005). The effect of functionalized self-assembling peptide scaffolds on human aortic endothelial cell function. *Biomaterials, 26*(16), 3341-3351. Retrieved from https://www.ncbi.nlm.nih.gov/pubmed/15603830. doi:10.1016/j.biomaterials.2004.08.012

Gerhardt, H., Golding, M., Fruttiger, M., Ruhrberg, C., Lundkvist, A., Abramsson, A., . . . Betsholtz, C. (2003). VEGF guides angiogenic sprouting utilizing endothelial tip cell filopodia. *J Cell Biol, 161*(6), 1163-1177. Retrieved from https://www.ncbi.nlm.nih.gov/pubmed/12810700. doi:10.1083/jcb.200302047

Ghosh, M., & Pearse, D. D. (2014). The role of the serotonergic system in locomotor recovery after spinal cord injury. *Front Neural Circuits, 8*, 151. Retrieved from https://www.ncbi.nlm.nih.gov/pubmed/25709569. doi:10.3389/fncir.2014.00151

Giulian, D., & Lachman, L. B. (1985). Interleukin-1 stimulation of astroglial proliferation after brain injury. *Science, 228*(4698), 497-499. Retrieved from https://www.ncbi.nlm.nih.gov/pubmed/3872478.

Grasman, J. M., & Kaplan, D. L. (2017). Human endothelial cells secrete neurotropic factors to direct axonal growth of peripheral nerves. *Sci Rep, 7*(1), 4092. Retrieved from https://www.ncbi.nlm.nih.gov/pubmed/28642578. doi:10.1038/s41598-017-04460-8

Griep, L. M., Wolbers, F., de Wagenaar, B., ter Braak, P. M., Weksler, B. B., Romero, I. A., . . . van den Berg, A. (2013). BBB on chip: microfluidic platform to mechanically and biochemically modulate blood-brain barrier function. *Biomed Microdevices, 15*(1), 145-150. Retrieved from https://www.ncbi.nlm.nih.gov/pubmed/22955726. doi:10.1007/s10544-012-9699-7

Grigoryan, B., Paulsen, S. J., Corbett, D. C., Sazer, D. W., Fortin, C. L., Zaita, A. J., . . . Ta, A. H. (2019). Multivascular networks and functional intravascular topologies within biocompatible hydrogels. *Science, 364*(6439), 458-464.

Guest, J. D., Rao, A., Olson, L., Bunge, M. B., & Bunge, R. P. (1997). The ability of human Schwann cell grafts to promote regeneration in the transected nude rat spinal cord. *Exp Neurol, 148*(2), 502-522. Retrieved from https://www.ncbi.nlm.nih.gov/pubmed/9417829. doi:10.1006/exnr.1997.6693

Guo, J., Su, H., Zeng, Y., Liang, Y. X., Wong, W. M., Ellis-Behnke, R. G., . . . Wu, W. (2007). Reknitting the injured spinal cord by self-assembling peptide nanofiber scaffold. *Nanomedicine, 3*(4), 311-321. Retrieved from https://www.ncbi.nlm.nih.gov/pubmed/17964861. doi:10.1016/j.nano.2007.09.003

Guo, X., & Kassab, G. S. (2004). Distribution of stress and strain along the porcine aorta and coronary arterial tree. *Am J Physiol Heart Circ Physiol, 286*(6), H2361-2368. Retrieved from https://www.ncbi.nlm.nih.gov/pubmed/15148060. doi:10.1152/ajpheart.01079.2003

Harkema, S. J. (2008). Plasticity of interneuronal networks of the functionally isolated human spinal cord. *Brain Res Rev, 57*(1), 255-264. Retrieved from https://www.ncbi.nlm.nih.gov/pubmed/18042493. doi:10.1016/j.brainresrev.2007.07.012

Hawkins, B. T., & Davis, T. P. (2005). The blood-brain barrier/neurovascular unit in health and disease. *Pharmacol Rev, 57*(2), 173-185. Retrieved from https://www.ncbi.nlm.nih.gov/pubmed/15914466. doi:10.1124/pr.57.2.4

Hayashi, K., Nakao, S., Nakaoke, R., Nakagawa, S., Kitagawa, N., & Niwa, M. (2004). Effects of hypoxia on endothelial/pericytic co-culture model of the blood-brain barrier. *Regul Pept, 123*(1-3), 77-83. Retrieved from https://www.ncbi.nlm.nih.gov/pubmed/15518896. doi:10.1016/j.regpep.2004.05.023

Herland, A., van der Meer, A. D., FitzGerald, E. A., Park, T. E., Sleeboom, J. J., & Ingber, D. E. (2016). Distinct Contributions of Astrocytes and Pericytes to Neuroinflammation Identified in a 3D Human Blood-Brain Barrier on a Chip. *PLoS One, 11*(3), e0150360. Retrieved from https://www.ncbi.nlm.nih.gov/pubmed/26930059. doi:10.1371/journal.pone.0150360

Hill, C. E., Hurtado, A., Blits, B., Bahr, B. A., Wood, P. M., Bartlett Bunge, M., & Oudega, M. (2007). Early necrosis and apoptosis of Schwann cells transplanted into the injured rat spinal cord. *Eur J Neurosci, 26*(6), 1433-1445. Retrieved from https://www.ncbi.nlm.nih.gov/pubmed/17880386. doi:10.1111/j.1460-9568.2007.05771.x

Hirase, T., Staddon, J. M., Saitou, M., Ando-Akatsuka, Y., Itoh, M., Furuse, M., . . . Rubin, L. L. (1997). Occludin as a possible determinant of tight junction permeability in endothelial cells. *Journal of cell science, 110*(14), 1603-1613.

Holmes, T. C., de Lacalle, S., Su, X., Liu, G., Rich, A., & Zhang, S. (2000). Extensive neurite outgrowth and active synapse formation on self-assembling peptide scaffolds. *Proceedings of the National Academy of Sciences, 97*(12), 6728-6733.

Hugenholtz, H. (2003). Methylprednisolone for acute spinal cord injury: not a standard of care. *CMAJ, 168*(9), 1145-1146. Retrieved from https://www.ncbi.nlm.nih.gov/pubmed/12719318.

Hurtado, A., Cregg, J. M., Wang, H. B., Wendell, D. F., Oudega, M., Gilbert, R. J., & McDonald, J. W. (2011). Robust CNS regeneration after complete spinal cord transection using aligned poly-L-lactic acid microfibers. *Biomaterials, 32*(26), 6068-6079. Retrieved from https://www.ncbi.nlm.nih.gov/pubmed/21636129. doi:10.1016/j.biomaterials.2011.05.006

Jin, Y., Neuhuber, B., Singh, A., Bouyer, J., Lepore, A., Bonner, J., . . . Fischer, I. (2011). Transplantation of human glial restricted progenitors and derived astrocytes into a contusion model of spinal cord injury. *Journal of neurotrauma, 28*(4), 579-594.

Kadoya, K., Lu, P., Nguyen, K., Lee-Kubli, C., Kumamaru, H., Yao, L., . . . Tuszynski, M. H. (2016). Spinal cord reconstitution with homologous neural grafts enables robust corticospinal regeneration. *Nat Med, 22*(5), 479-487. Retrieved from https://www.ncbi.nlm.nih.gov/pubmed/27019328. doi:10.1038/nm.4066

Kanda, T., Numata, Y., & Mizusawa, H. (2004). Chronic inflammatory demyelinating polyneuropathy: decreased claudin-5 and relocated ZO-1. *Journal of Neurology, Neurosurgery & Psychiatry, 75*(5), 765-769.

Kassab, G. S., Le, K. N., & Fung, Y. C. (1999). A hemodynamic analysis of coronary capillary blood flow based on anatomic and distensibility data. *Am J Physiol, 277*(6 Pt 2), H2158-2166. Retrieved from https://www.ncbi.nlm.nih.gov/pubmed/10600833.

Keirstead, H. S., Nistor, G., Bernal, G., Totoiu, M., Cloutier, F., Sharp, K., & Steward, O. (2005). Human embryonic stem cell-derived oligodendrocyte progenitor cell transplants remyelinate and restore locomotion after spinal cord injury. *J Neurosci, 25*(19), 4694-4705. Retrieved from https://www.ncbi.nlm.nih.gov/pubmed/15888645. doi:10.1523/JNEUROSCI.0311-05.2005

Koch, D., Rosoff, W. J., Jiang, J., Geller, H. M., & Urbach, J. S. (2012). Strength in the periphery: growth cone biomechanics and substrate rigidity response in peripheral and central nervous system neurons. *Biophysical journal, 102*(3), 452-460.

Koffler, J., Zhu, W., Qu, X., Platoshyn, O., Dulin, J. N., Brock, J., . . . Tuszynski, M. H. (2019). Biomimetic 3D-printed scaffolds for spinal cord injury repair. *Nat Med, 25*(2), 263-269. Retrieved from https://www.ncbi.nlm.nih.gov/pubmed/30643285. doi:10.1038/s41591-018-0296-z

Kovacs, M., Toth, J., Hetenyi, C., Malnasi-Csizmadia, A., & Sellers, J. R. (2004). Mechanism of blebbistatin inhibition of myosin II. *J Biol Chem, 279*(34), 35557-35563. Retrieved from https://www.ncbi.nlm.nih.gov/pubmed/15205456. doi:10.1074/jbc.M405319200

Krishnan, L., Underwood, C. J., Maas, S., Ellis, B. J., Kode, T. C., Hoying, J. B., & Weiss, J. A. (2008). Effect of mechanical boundary conditions on orientation of angiogenic microvessels. *Cardiovasc Res, 78*(2), 324-332. Retrieved from https://www.ncbi.nlm.nih.gov/pubmed/18310100. doi:10.1093/cvr/cvn055

Krych, A. J., Rooney, G. E., Chen, B., Schermerhorn, T. C., Ameenuddin, S., Gross, L., . . . Friedman, J. A. (2009). Relationship between scaffold channel diameter and number of regenerating axons in the transected rat spinal cord. *Acta biomaterialia, 5*(7), 2551-2559.

Lacroix, S., Chang, L., Rose-John, S., & Tuszynski, M. H. (2002). Delivery of hyper-interleukin-6 to the injured spinal cord increases neutrophil and macrophage infiltration and inhibits axonal growth. *J Comp Neurol, 454*(3), 213-228. Retrieved from https://www.ncbi.nlm.nih.gov/pubmed/12442313. doi:10.1002/cne.10407

Lagord, C., Berry, M., & Logan, A. (2002). Expression of TGFbeta2 but not TGFbeta1 correlates with the deposition of scar tissue in the lesioned spinal cord. *Mol Cell Neurosci, 20*(1), 69-92. Retrieved from https://www.ncbi.nlm.nih.gov/pubmed/12056841. doi:10.1006/mcne.2002.1121

Lammertse, D. P., Jones, L. A., Charlifue, S. B., Kirshblum, S. C., Apple, D. F., Ragnarsson, K. T., . . . Knoller, N. (2012). Autologous incubated macrophage therapy in acute, complete spinal cord injury: results of the phase 2 randomized controlled multicenter trial. *Spinal Cord, 50*(9), 661-671. Retrieved from https://www.ncbi.nlm.nih.gov/pubmed/22525310. doi:10.1038/sc.2012.39

Lazarovici, P., Marcinkiewicz, C., & Lelkes, P. I. (2006). Cross talk between the cardiovascular and nervous systems: neurotrophic effects of vascular endothelial growth factor (VEGF) and angiogenic effects of nerve growth factor (NGF)-implications in drug development. *Curr Pharm Des, 12*(21), 2609-2622. Retrieved from https://www.ncbi.nlm.nih.gov/pubmed/16842161.

Lee, B. B., Cripps, R. A., Fitzharris, M., & Wing, P. C. (2014). The global map for traumatic spinal cord injury epidemiology: update 2011, global incidence rate. *Spinal Cord, 52*(2), 110-116. Retrieved from https://www.ncbi.nlm.nih.gov/pubmed/23439068. doi:10.1038/sc.2012.158

Lehman, R. A., Jr., Taylor, B. A., Rhee, J. M., & Riew, K. D. (2008). Cervical laminaplasty. *J Am Acad Orthop Surg, 16*(1), 47-56. Retrieved from https://www.ncbi.nlm.nih.gov/pubmed/18180392.

Li, Y., Field, P. M., & Raisman, G. (1997). Repair of adult rat corticospinal tract by transplants of olfactory ensheathing cells. *Science, 277*(5334), 2000-2002. Retrieved from https://www.ncbi.nlm.nih.gov/pubmed/9302296.

Li, Y., & Raisman, G. (1995). Sprouts from cut corticospinal axons persist in the presence of astrocytic scarring in long-term lesions of the adult rat spinal cord. *Exp Neurol, 134*(1), 102-111. Retrieved from https://www.ncbi.nlm.nih.gov/pubmed/7672031. doi:10.1006/exnr.1995.1041

Liu, Z., Tan, J. L., Cohen, D. M., Yang, M. T., Sniadecki, N. J., Ruiz, S. A., . . . Chen, C. S. (2010). Mechanical tugging force regulates the size of cell-cell junctions. *Proc Natl Acad Sci U S A, 107*(22), 9944-9949. Retrieved from https://www.ncbi.nlm.nih.gov/pubmed/20463286. doi:10.1073/pnas.0914547107

Lu, P., Wang, Y., Graham, L., McHale, K., Gao, M., Wu, D., . . . Tuszynski, M. H. (2012). Long-distance growth and connectivity of neural stem cells after severe spinal cord injury. *Cell, 150*(6), 1264-1273. Retrieved from https://www.ncbi.nlm.nih.gov/pubmed/22980985. doi:10.1016/j.cell.2012.08.020

Lu, P., Yang, H., Jones, L. L., Filbin, M. T., & Tuszynski, M. H. (2004). Combinatorial therapy with neurotrophins and cAMP promotes axonal regeneration beyond sites of spinal cord injury. *J Neurosci, 24*(28), 6402-6409. Retrieved from https://www.ncbi.nlm.nih.gov/pubmed/15254096. doi:10.1523/JNEUROSCI.1492-04.2004

Mackay-Sim, A., Feron, F., Cochrane, J., Bassingthwaighte, L., Bayliss, C., Davies, W., . . . Geraghty, T. (2008). Autologous olfactory ensheathing cell transplantation in human paraplegia: a 3-year clinical trial. *Brain, 131*(Pt 9), 2376-2386. Retrieved from https://www.ncbi.nlm.nih.gov/pubmed/18689435. doi:10.1093/brain/awn173

Maslov, K., Zhang, H. F., Hu, S., & Wang, L. V. (2008). Optical-resolution photoacoustic microscopy for in vivo imaging of single capillaries. *Opt Lett, 33*(9), 929-931. Retrieved from https://www.ncbi.nlm.nih.gov/pubmed/18451942.

Maynard Jr, F. M., Bracken, M. B., Creasey, G., Ditunno Jr, J. F., Donovan, W. H., Ducker, T. B., . . . Tator, C. H. (1997). International standards for neurological and functional classification of spinal cord injury. *Spinal Cord, 35*(5), 266.

McKeon, R. J., Hoke, A., & Silver, J. (1995). Injury-induced proteoglycans inhibit the potential for laminin-mediated axon growth on astrocytic scars. *Exp Neurol, 136*(1), 32-43. Retrieved from https://www.ncbi.nlm.nih.gov/pubmed/7589332. doi:10.1006/exnr.1995.1081

Medalha, C. C., Jin, Y., Yamagami, T., Haas, C., & Fischer, I. (2014). Transplanting neural progenitors into a complete transection model of spinal cord injury. *J Neurosci Res, 92*(5), 607-618. Retrieved from https://www.ncbi.nlm.nih.gov/pubmed/24452691. doi:10.1002/jnr.23340

Moeendarbary, E., Weber, I. P., Sheridan, G. K., Koser, D. E., Soleman, S., Haenzi, B., . . . Franze, K. (2017). The soft mechanical signature of glial scars in the central nervous system. *Nat Commun, 8*, 14787. Retrieved from https://www.ncbi.nlm.nih.gov/pubmed/28317912. doi:10.1038/ncomms14787

Monti Graziadei, G. A., Karlan, M. S., Bernstein, J. J., & Graziadei, P. P. (1980). Reinnervation of the olfactory bulb after section of the olfactory nerve in monkey (Saimiri sciureus). *Brain Res, 189*(2), 343-354. Retrieved from https://www.ncbi.nlm.nih.gov/pubmed/6768424.

Moore, M. J., Friedman, J. A., Lewellyn, E. B., Mantila, S. M., Krych, A. J., Ameenuddin, S., . . . Yaszemski, M. J. (2006). Multiple-channel scaffolds to promote spinal cord axon regeneration. *Biomaterials, 27*(3), 419-429. Retrieved from https://www.ncbi.nlm.nih.gov/pubmed/16137759. doi:10.1016/j.biomaterials.2005.07.045

Morin, K. T., Dries-Devlin, J. L., & Tranquillo, R. T. (2014). Engineered microvessels with strong alignment and high lumen density via cell-induced fibrin gel compaction and interstitial flow. *Tissue Eng Part A, 20*(3-4), 553-565. Retrieved from https://www.ncbi.nlm.nih.gov/pubmed/24083839. doi:10.1089/ten.TEA.2013.0262

Mothe, A. J., & Tator, C. H. (2013). Review of transplantation of neural stem/progenitor cells for spinal cord injury. *Int J Dev Neurosci, 31*(7), 701-713. Retrieved from https://www.ncbi.nlm.nih.gov/pubmed/23928260. doi:10.1016/j.ijdevneu.2013.07.004

Moussa, W. M. (2012). Anterior cervical discectomy versus posterior keyhole foraminotomy in cervical radiculopathy. *Alexandria Journal of Medicine, 48*(4), 309-314. Retrieved from http://www.sciencedirect.com/science/article/pii/S2090506812000449. doi:https://doi.org/10.1016/j.ajme.2012.04.002

Nakahashi, T., Fujimura, H., Altar, C. A., Li, J., Kambayashi, J.-i., Tandon, N. N., & Sun, B. (2000). Vascular endothelial cells synthesize and secrete brain-derived neurotrophic factor. *FEBS letters, 470*(2), 113-117.

Nakajima, H., Uchida, K., Guerrero, A. R., Watanabe, S., Sugita, D., Takeura, N., . . . Baba, H. (2012). Transplantation of mesenchymal stem cells promotes an alternative pathway of macrophage activation and functional recovery after spinal cord injury. *J Neurotrauma, 29*(8), 1614-1625. Retrieved from https://www.ncbi.nlm.nih.gov/pubmed/22233298. doi:10.1089/neu.2011.2109

National Spinal Cord Injury Statistical Center, Facts and Figures at a Glance. (2017). *Birmingham, AL: University of Alabama at Birmingham*.

Nguyen, D. H., Stapleton, S. C., Yang, M. T., Cha, S. S., Choi, C. K., Galie, P. A., & Chen, C. S. (2013). Biomimetic model to reconstitute angiogenic sprouting morphogenesis in vitro. *Proc Natl Acad Sci U S A, 110*(17), 6712-6717. Retrieved from https://www.ncbi.nlm.nih.gov/pubmed/23569284. doi:10.1073/pnas.1221526110

Norenberg, M. D., Smith, J., & Marcillo, A. (2004). The pathology of human spinal cord injury: defining the problems. *J Neurotrauma, 21*(4), 429-440. Retrieved from https://www.ncbi.nlm.nih.gov/pubmed/15115592. doi:10.1089/089771504323004575

Pan, W., Banks, W. A., & Kastin, A. J. (1997). Permeability of the blood–brain and blood–spinal cord barriers to interferons. *Journal of neuroimmunology, 76*(1-2), 105-111.

Pardridge, W. M., Triguero, D., Yang, J., & Cancilla, P. A. (1990). Comparison of in vitro and in vivo models of drug transcytosis through the blood-brain barrier. *J Pharmacol Exp Ther, 253*(2), 884-891. Retrieved from https://www.ncbi.nlm.nih.gov/pubmed/2338660.

Parr, A. M., Kulbatski, I., Zahir, T., Wang, X., Yue, C., Keating, A., & Tator, C. H. (2008). Transplanted adult spinal cord-derived neural stem/progenitor cells promote early functional recovery after rat spinal cord injury. *Neuroscience, 155*(3), 760-770. Retrieved from https://www.ncbi.nlm.nih.gov/pubmed/18588947. doi:10.1016/j.neuroscience.2008.05.042

Partyka, P. P., Godsey, G. A., Galie, J. R., Kosciuk, M. C., Acharya, N. K., Nagele, R. G., & Galie, P. A. (2017). Mechanical stress regulates transport in a compliant 3D model of the blood-brain barrier. *Biomaterials, 115*, 30-39. Retrieved from https://www.ncbi.nlm.nih.gov/pubmed/27886553. doi:10.1016/j.biomaterials.2016.11.012

Partyka, P. P., Jin, Y., Bouyer, J., DaSilva, A., Godsey, G. A., Nagele, R. G., . . . Galie, P. A. (2019). Harnessing neurovascular interaction to guide axon growth. *Sci Rep, 9*(1), 2190. Retrieved from https://www.ncbi.nlm.nih.gov/pubmed/30778117. doi:10.1038/s41598-019-38558-y

Pearse, D. D., Pereira, F. C., Marcillo, A. E., Bates, M. L., Berrocal, Y. A., Filbin, M. T., & Bunge, M. B. (2004). cAMP and Schwann cells promote axonal growth and functional recovery after spinal cord injury. *Nat Med, 10*(6), 610-616. Retrieved from https://www.ncbi.nlm.nih.gov/pubmed/15156204. doi:10.1038/nm1056

Persidsky, Y., Ramirez, S. H., Haorah, J., & Kanmogne, G. D. (2006). Blood-brain barrier: structural components and function under physiologic and pathologic conditions. *J Neuroimmune Pharmacol, 1*(3), 223-236. Retrieved from https://www.ncbi.nlm.nih.gov/pubmed/18040800. doi:10.1007/s11481-006-9025-3

Phillips, A. A., Warburton, D. E., Ainslie, P. N., & Krassioukov, A. V. (2014). Regional neurovascular coupling and cognitive performance in those with low blood pressure secondary to high-level spinal cord injury: improved by alpha-1 agonist midodrine hydrochloride. *J Cereb Blood Flow Metab, 34*(5), 794-801. Retrieved from https://www.ncbi.nlm.nih.gov/pubmed/24473484. doi:10.1038/jcbfm.2014.3

Placone, A. L., McGuiggan, P. M., Bergles, D. E., Guerrero-Cazares, H., Quinones-Hinojosa, A., & Searson, P. C. (2015). Human astrocytes develop physiological morphology and remain quiescent in a novel 3D matrix. *Biomaterials, 42*, 134-143. Retrieved from https://www.ncbi.nlm.nih.gov/pubmed/25542801. doi:10.1016/j.biomaterials.2014.11.046

Polacheck, W. J., Charest, J. L., & Kamm, R. D. (2011). Interstitial flow influences direction of tumor cell migration through competing mechanisms. *Proc Natl Acad Sci U S A, 108*(27), 11115-11120. Retrieved from https://www.ncbi.nlm.nih.gov/pubmed/21690404
https://www.ncbi.nlm.nih.gov/pmc/articles/PMC3131352/pdf/pnas.201103581.pdf. doi:10.1073/pnas.1103581108

Prabhakarpandian, B., Shen, M. C., Nichols, J. B., Mills, I. R., Sidoryk-Wegrzynowicz, M., Aschner, M., & Pant, K. (2013). SyM-BBB: a microfluidic Blood Brain Barrier model. *Lab Chip, 13*(6), 1093-1101. Retrieved from https://www.ncbi.nlm.nih.gov/pubmed/23344641. doi:10.1039/c2lc41208j

Preston, E., Webster, J., & Small, D. (2001). Characteristics of sustained blood-brain barrier opening and tissue injury in a model for focal trauma in the rat. *J Neurotrauma, 18*(1), 83-92. Retrieved from https://www.ncbi.nlm.nih.gov/pubmed/11200252. doi:10.1089/089771501750055794

Prockop, L. D., Naidu, K. A., Binard, J. E., & Ransohoff, J. (1995). Selective Permeability of [3H]-D-Mannitol and [l4C]-Carboxyl-lnulin Across the Blood-Brain Barrier and Blood-Spinal Cord Barrier in the Rabbit. *The journal of spinal cord medicine, 18*(4), 221-226.

Ramo, N. L., Troyer, K. L., & Puttlitz, C. M. (2018). Viscoelasticity of spinal cord and meningeal tissues. *Acta biomaterialia, 75*, 253-262.

Ramon-Cueto, A., Cordero, M. I., Santos-Benito, F. F., & Avila, J. (2000). Functional recovery of paraplegic rats and motor axon regeneration in their spinal cords by olfactory ensheathing glia. *Neuron, 25*(2), 425-435. Retrieved from https://www.ncbi.nlm.nih.gov/pubmed/10719896.

Ramon-Cueto, A., Plant, G. W., Avila, J., & Bunge, M. B. (1998). Long-distance axonal regeneration in the transected adult rat spinal cord is promoted by olfactory ensheathing glia transplants. *J Neurosci, 18*(10), 3803-3815. Retrieved from https://www.ncbi.nlm.nih.gov/pubmed/9570810.

Ramon y Cajal, S. (1928). Degeneration and regeneration of the nervous system.

Riemenschneider, S. B., Mattia, D. J., Wendel, J. S., Schaefer, J. A., Ye, L., Guzman, P. A., & Tranquillo, R. T. (2016). Inosculation and perfusion of pre-vascularized tissue patches containing aligned human microvessels after myocardial infarction. *Biomaterials, 97*, 51-61. Retrieved from https://www.ncbi.nlm.nih.gov/pubmed/27162074. doi:10.1016/j.biomaterials.2016.04.031

Rosenzweig, E. S., Brock, J. H., Lu, P., Kumamaru, H., Salegio, E. A., Kadoya, K., . . . Tuszynski, M. H. (2018). Restorative effects of human neural stem cell grafts on the primate spinal cord. *Nat Med, 24*(4), 484-490. Retrieved from https://www.ncbi.nlm.nih.gov/pubmed/29480894. doi:10.1038/nm.4502

Rubin, L. L., Hall, D. E., Porter, S., Barbu, K., Cannon, C., Horner, H. C., . . . et al. (1991). A cell culture model of the blood-brain barrier. *J Cell Biol, 115*(6), 1725-1735. Retrieved from https://www.ncbi.nlm.nih.gov/pubmed/1661734.

Saglam, A., Perets, A., Canver, A. C., Li, H. L., Kollins, K., Cohen, G., . . . Lelkes, P. I. (2013). Angioneural crosstalk in scaffolds with oriented microchannels for regenerative spinal cord injury repair. *J Mol Neurosci, 49*(2), 334-346. Retrieved from https://www.ncbi.nlm.nih.gov/pubmed/22878912. doi:10.1007/s12031-012-9863-9

Sahni, V., & Kessler, J. A. (2010). Stem cell therapies for spinal cord injury. *Nat Rev Neurol, 6*(7), 363-372. Retrieved from https://www.ncbi.nlm.nih.gov/pubmed/20551948. doi:10.1038/nrneurol.2010.73

Sekhon, L. H., & Fehlings, M. G. (2001). Epidemiology, demographics, and pathophysiology of acute spinal cord injury. *Spine (Phila Pa 1976), 26*(24 Suppl), S2-12. Retrieved from https://www.ncbi.nlm.nih.gov/pubmed/11805601.

Sezer, N., Akkuş, S., & Uğurlu, F. G. (2015). Chronic complications of spinal cord injury. *World journal of orthopedics, 6*(1), 24.

Shin, Y., Jeon, J. S., Han, S., Jung, G. S., Shin, S., Lee, S. H., . . . Chung, S. (2011). In vitro 3D collective sprouting angiogenesis under orchestrated ANG-1 and VEGF gradients. *Lab Chip, 11*(13), 2175-2181. Retrieved from https://www.ncbi.nlm.nih.gov/pubmed/21617793. doi:10.1039/c1lc20039a

Siddall, P. J., McClelland, J. M., Rutkowski, S. B., & Cousins, M. J. (2003). A longitudinal study of the prevalence and characteristics of pain in the first 5 years following spinal cord injury. *Pain, 103*(3), 249-257. Retrieved from https://www.ncbi.nlm.nih.gov/pubmed/12791431.

Sieminski, A. L., Was, A. S., Kim, G., Gong, H., & Kamm, R. D. (2007). The stiffness of three-dimensional ionic self-assembling peptide gels affects the extent of capillary-like network formation. *Cell Biochem Biophys, 49*(2), 73-83. Retrieved from https://www.ncbi.nlm.nih.gov/pubmed/17906362.

Silver, J., & Miller, J. H. (2004). Regeneration beyond the glial scar. *Nat Rev Neurosci, 5*(2), 146-156. Retrieved from https://www.ncbi.nlm.nih.gov/pubmed/14735117. doi:10.1038/nrn1326

Smith, J. R., Galie, P. A., Slochower, D. R., Weisshaar, C. L., Janmey, P. A., & Winkelstein, B. A. (2016). Salmon-derived thrombin inhibits development of chronic pain through an endothelial barrier protective mechanism dependent on APC. *Biomaterials, 80*, 96-105. Retrieved from https://www.ncbi.nlm.nih.gov/pubmed/26708087. doi:10.1016/j.biomaterials.2015.11.062

Song, H. J., Ming, G. L., & Poo, M. M. (1997). cAMP-induced switching in turning direction of nerve growth cones. *Nature, 388*(6639), 275-279. Retrieved from https://www.ncbi.nlm.nih.gov/pubmed/9230436. doi:10.1038/40864

Stichel, C., & Müller, H. W. (1998). The CNS lesion scar: new vistas on an old regeneration barrier. *Cell and tissue research, 294*(1), 1-9.

Stokols, S., & Tuszynski, M. H. (2006). Freeze-dried agarose scaffolds with uniaxial channels stimulate and guide linear axonal growth following spinal cord injury. *Biomaterials, 27*(3), 443-451.

Takami, T., Oudega, M., Bates, M. L., Wood, P. M., Kleitman, N., & Bunge, M. B. (2002). Schwann cell but not olfactory ensheathing glia transplants improve hindlimb locomotor performance in the moderately contused adult rat thoracic spinal cord. *J Neurosci, 22*(15), 6670-6681. Retrieved from https://www.ncbi.nlm.nih.gov/pubmed/12151546. doi:20026636

Thome, C., Zevgaridis, D., Leheta, O., Bazner, H., Pockler-Schoniger, C., Wohrle, J., & Schmiedek, P. (2005). Outcome after less-invasive decompression of lumbar spinal stenosis: a randomized comparison of unilateral laminotomy, bilateral laminotomy, and laminectomy. *J Neurosurg Spine, 3*(2), 129-141. Retrieved from https://www.ncbi.nlm.nih.gov/pubmed/16370302. doi:10.3171/spi.2005.3.2.0129

van der Helm, M. W., van der Meer, A. D., Eijkel, J. C., van den Berg, A., & Segerink, L. I. (2016). Microfluidic organ-on-chip technology for blood-brain barrier research. *Tissue Barriers, 4*(1), e1142493. Retrieved from https://www.ncbi.nlm.nih.gov/pubmed/27141422. doi:10.1080/21688370.2016.1142493

van der Meer, A. D., Orlova, V. V., ten Dijke, P., van den Berg, A., & Mummery, C. L. (2013). Three-dimensional co-cultures of human endothelial cells and embryonic stem cell-derived pericytes inside a microfluidic device. *Lab Chip, 13*(18), 3562-3568. Retrieved from https://www.ncbi.nlm.nih.gov/pubmed/23702711. doi:10.1039/c3lc50435b

Wang, F., Huang, S.-L., He, X.-J., & Li, X.-H. (2014). Determination of the ideal rat model for spinal cord injury by diffusion tensor imaging. *Neuroreport, 25*(17), 1386.

Weksler, B. B., Subileau, E. A., Perriere, N., Charneau, P., Holloway, K., Leveque, M., . . . Couraud, P. O. (2005). Blood-brain barrier-specific properties of a human adult brain endothelial cell line. *FASEB J, 19*(13), 1872-1874. Retrieved from https://www.ncbi.nlm.nih.gov/pubmed/16141364. doi:10.1096/fj.04-3458fje

Wen, H., Watry, D. D., Marcondes, M. C. G., & Fox, H. S. (2004). Selective decrease in paracellular conductance of tight junctions: role of the first extracellular domain of claudin-5. *Molecular and cellular biology, 24*(19), 8408-8417.

Wernig, A., & Muller, S. (1992). Laufband locomotion with body weight support improved walking in persons with severe spinal cord injuries. *Paraplegia, 30*(4), 229-238. Retrieved from https://www.ncbi.nlm.nih.gov/pubmed/1625890. doi:10.1038/sc.1992.61

Wernig, A., Nanassy, A., & Muller, S. (1998). Maintenance of locomotor abilities following Laufband (treadmill) therapy in para- and tetraplegic persons: follow-up studies. *Spinal Cord, 36*(11), 744-749. Retrieved from https://www.ncbi.nlm.nih.gov/pubmed/9848480.

Westgren, N., & Levi, R. (1998). Quality of life and traumatic spinal cord injury. *Arch Phys Med Rehabil, 79*(11), 1433-1439. Retrieved from https://www.ncbi.nlm.nih.gov/pubmed/9821906.

Winkler, E. A., Bell, R. D., & Zlokovic, B. V. (2011). Lack of Smad or Notch leads to a fatal game of brain pericyte hopscotch. *Dev Cell, 20*(3), 279-280. Retrieved from https://www.ncbi.nlm.nih.gov/pubmed/21397835. doi:10.1016/j.devcel.2011.03.002

Witt, K. A., Mark, K. S., Hom, S., & Davis, T. P. (2003). Effects of hypoxia-reoxygenation on rat blood-brain barrier permeability and tight junctional protein expression. *Am J Physiol Heart Circ Physiol, 285*(6), H2820-2831. Retrieved from https://www.ncbi.nlm.nih.gov/pubmed/12907427. doi:10.1152/ajpheart.00589.2003

Xu, X. M., Guenard, V., Kleitman, N., Aebischer, P., & Bunge, M. B. (1995). A combination of BDNF and NT-3 promotes supraspinal axonal regeneration into Schwann cell grafts in adult rat thoracic spinal cord. *Exp Neurol, 134*(2), 261-272. Retrieved from https://www.ncbi.nlm.nih.gov/pubmed/7556546. doi:10.1006/exnr.1995.1056

Yao, R., Murtaza, M., Velasquez, J. T., Todorovic, M., Rayfield, A., Ekberg, J., . . . St John, J. (2018). Olfactory Ensheathing Cells for Spinal Cord Injury: Sniffing Out the Issues. *Cell Transplant, 27*(6), 879-889. Retrieved from https://www.ncbi.nlm.nih.gov/pubmed/29882418. doi:10.1177/0963689718779353

Ye, Z., Zhang, H., Luo, H., Wang, S., Zhou, Q., Du, X., . . . Zhao, X. (2008). Temperature and pH effects on biophysical and morphological properties of self-assembling peptide RADA16-I. *J Pept Sci, 14*(2), 152-162. Retrieved from https://www.ncbi.nlm.nih.gov/pubmed/18196533. doi:10.1002/psc.988

Yu, X., Dillon, G. P., & Bellamkonda, R. B. (1999). A laminin and nerve growth factor-laden three-dimensional scaffold for enhanced neurite extension. *Tissue Eng, 5*(4), 291-304. Retrieved from https://www.ncbi.nlm.nih.gov/pubmed/10477852. doi:10.1089/ten.1999.5.291

Yuan, H., Gaber, M. W., Boyd, K., Wilson, C. M., Kiani, M. F., & Merchant, T. E. (2006). Effects of fractionated radiation on the brain vasculature in a murine model: blood-brain barrier permeability, astrocyte proliferation, and ultrastructural changes. *Int J Radiat Oncol Biol Phys, 66*(3), 860-866. Retrieved from https://www.ncbi.nlm.nih.gov/pubmed/17011458. doi:10.1016/j.ijrobp.2006.06.043

Zeng, X., Zeng, Y. S., Ma, Y. H., Lu, L. Y., Du, B. L., Zhang, W., . . . Chan, W. Y. (2011). Bone marrow mesenchymal stem cells in a three-dimensional gelatin sponge scaffold attenuate inflammation, promote angiogenesis, and reduce cavity formation in experimental spinal cord injury. *Cell Transplant, 20*(11-12), 1881-1899. Retrieved from https://www.ncbi.nlm.nih.gov/pubmed/21396163. doi:10.3727/096368911X566181

Zhu, J., Lu, Y., Yu, F., Zhou, L., Shi, J., Chen, Q., . . . Wang, J. (2018). Effect of decellularized spinal scaffolds on spinal axon regeneration in rats. *J Biomed Mater Res A, 106*(3), 698-705. Retrieved from https://www.ncbi.nlm.nih.gov/pubmed/28986946. doi:10.1002/jbm.a.36266